MSc Dissertation
Prevention and Management of Natural Hazards
Faculty of Geology and Geo-environment
National and Kapodestrian University of Athens

Study of the earthquake site-effects of the broader Karditsa urban area and deterministic strong ground motion simulation for the main seismic/active faults of the Thessaly area, using field measurements, stochastic simulations, and Geographic Information Systems

Giannis Papazachos
22010

Dissertation supervisor: Professor Efthymios Lekkas

June 2013

(This page is left intentionally blank)

Abstract

The current master's dissertation was submitted in partial fulfillment of the requirements of Master of Science in Prevention and Management of Natural Hazards, Faculty of Geology and Geo-environment, National and Kapodestrian University of Athens. In its first part, this study aimed at estimating the ground response for the simulated seismic motions from strong earthquakes, within the broader area of Karditsa (central Greece). For this purpose, the geotechnical / geophysical background of the city of Karditsa was studied, by employing existing microzonation data (Lekkas, 1998) and performing ambient noise (HVSR) measurements. The analysis of microzonation geotechnical data led to the creation of the V_{s30} model for the area, which showed small-scale spatial variations of the shear wave velocity, V_s, for the uppermost 30m. This was partly expected due to the known geological setting of the study area. In the second part, a more generic approach was adopted, concerning a larger study area (broader area of the whole Thessaly plain). In this approach, it was attempted to simulate the damage distribution for the 1954, M=7.0 Sofades earthquake and the 1957, M=6.8 Velestino earthquake, using synthesized seismic motions, which were appropriately converted to macroseismic intensity (Modified Mercalli scale, I_{MM}), after incorporating the site-effect through the local geology (the geological formations of the area have been studied extensively in the past, Papanikolaou and Sideris, 2007). Since no instrumental recordings were available for the specific events, macroseismic intensities (I_{MM} up to 9+) for these events were used, as they have been observed in the broader Thessaly area. For the simulations, a modified stochastic finite-fault method (EXSIM algorithm, Motazedian and Atkinson, 2005) was used, in order to reproduce the damage distribution of both earthquakes.

The simulation approach attempts to combine existing earthquake information and appropriate scaling relations with surface geology, in order to investigate the efficiency and usefulness of the available macroseismic data

(Papazachos et al., 1997). For the estimation of the fault dimensions, the calibrating equations for fault geometry from moment magnitude proposed for dip-slip faults by Papazachos et al. (2004) and Papazachos et al. (2006) were utilized. In order to account for site-effects on the observed seismic motions, a new digitized geological map for the broader Thessaly basin was created, using the 1:50000 geological maps of the Greek Institute of Geology and Mineral Exploration (IGME). The geological formations were grouped according to their age and mapped on appropriate soil classes, according to EC8.

Synthetic time series were estimated for different rupture scenarios. In order to compare the obtained stochastic motions with the historical (macroseismic) information, various relations between PGA and PGV (obtained from the stochastic records) and macroseismic intensity were considered, allowing the generation of synthetic (stochastic) isoseismals. For each soil class, different site amplification factors were tested, according to local geology (Skarlatoudis et al., 2003; Klimis et al., 1999). Moreover, a trial-and-error optimization of each fault position has been performed, using the available seismological information, as well as the published neotectonic data for these events and the broader southern Thessaly fault zone (Papastamatiou and Mouyaris, 1986; Mountrakis et al., 1993).

The results confirm the applicability of the proposed approach. The finally determined positions of both faults are different than previously proposed, in agreement with the available neotectonic information. The observed macroseismic intensities are also in very good agreement with the stochastic simulation predictions, verifying both the usefulness of the approach, as well as of the macroseismic data used. Site-effects show an excellent correlation with the geological classification employed. Moreover, the constant amplification factors of Skarlatoudis et al. (2003) show a very good agreement with the observed amplifications, whereas the generic transfer functions proposed by Klimis et al. (1999) seem to lead to higher site amplifications, not observed in the real data, probably due to the very large thickness of Quaternary formations in the broader Thessaly basin. These large thicknesses lead to very low resonant frequencies, significantly differ-

ent to the generic transfer functions of Klimis et al. (1999), as verified by appropriate HVSR measurements performed along selected profiles in the southern Karditsa area.

(This page is left intentionally blank)

Acknowledgements

Thank you to the following people who helped with this work and its eventual realization:

My supervisor, professor Efthymios Lekkas, for his trust, guidance and constructive criticism throughout all the stages of this work.

The members of my committee, associate professor Voulgaris Nikolaos and assistant professor Alexopoulos Ioannis, for their detailed observations and suggestions on this work.

Professor Costas Papazachos from the Aristotle University of Thessaloniki, without whom this work could not be realized.

M.Sc. Geophysicist Harris Kkallas for our cooperation and his support during the ambient noise data collection field work.

Dr. Andreas Skarlatoudis for his suggestions and guidance regarding the stochastic simulation process.

Ass. Prof. Georgios Vargemezis for his critical help on GIS issues.

My classmates, especially Leonidas, Vivi, Eleni and Georgia, for all the fun, the encouragement and mostly the gossip.

Dimitrios Theocharis, Vera Antoniou and Aggelos Pallikarakis for their assistance and support to us throughout the MSc program.

My dearest friends Miltos (for his might) and Irina (for her magic).

Most of all, my parents, Costas and Lela, for making it possible for me to study in the first place and urging me to continue during hard times.

And, of course, my Ευτυχία[1].

[1] /ɛfti:hˈi:ə/; a Greek female given name, meaning happiness

(This page is left intentionally blank)

Contents

List of Figures

List of Tables

1.Introduction

1.1 Thessaly area geological and morphotectonic characteristics

The broader Thessaly area is located at the back-arc area of the Aegean micro-plate and is one of the most seismically active areas of Greece. The Thessaly plain, the largest plain of central Greece, is particularly interesting from both the neotectonic and active tectonics point of view, because it is a well-defined, inland basin, filled with recent Quaternary and Neogene sediments in which intense seismicity has been observed during historical times, especially during the 20^{th} century.

1.1.1 Morphological setting

Within the Thessaly plain, altitudes range from 45m to 200m. The basin is surrounded by mountainous terrain area, with an average altitude of exceeding 1000m. As can be seen in Figure 1.1, Antichassia and Kato Olimpos mountains occupy the northern part of Thessaly area, Ossa, Mavrovouni and Pilio mountains dominate its eastern section, while the western and southern parts of the basin are occupied by the Pindos and Othris ranges, respectively. In the middle of the Thessaly plain a morphological ridge exists, which consists of the mountains of Zarkou and Titanos. The axis of this ridge coincides with the region's tectonic lines and divides the plain into an eastern and a western basin.

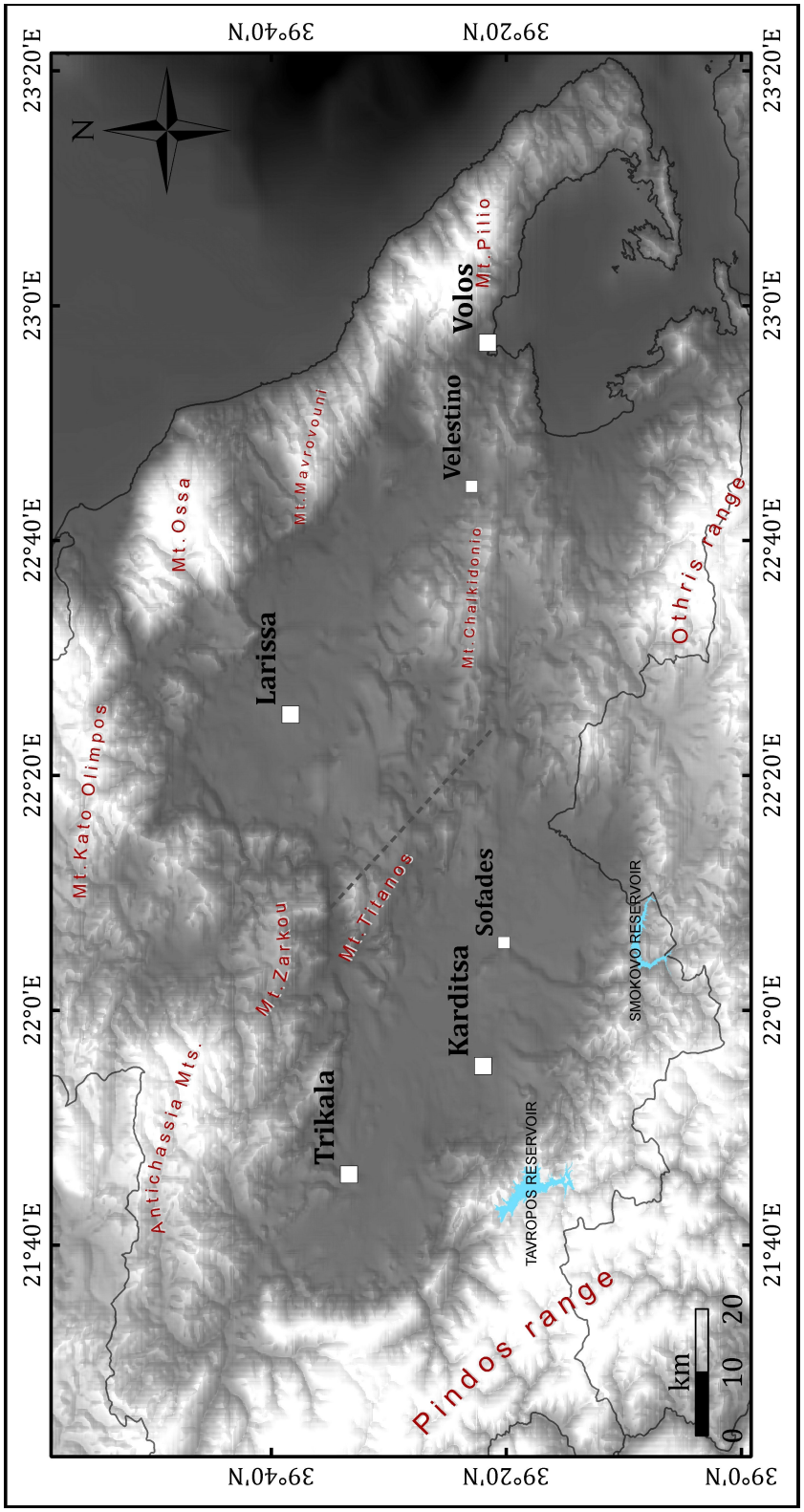

Figure 1.1: Main morphological features of the Thessaly basin area.

1.1.2 Active tectonics of the broader Thessaly area

The term 'active tectonics' of a region usually describes the recent geological processes within the region, which often result in seismic activity and related geodynamic and morphotectonic phenomena. The active tectonic setting of the broader Aegean area has been extensively studied, in order to define more precisely the boundaries of tectonic plates and the direction and speed of their movement. The main results, obtained by combining geophysical, geodetic and geological methods, indicate that the lithosphere of the eastern Mediterranean (front part of the African plate) converges with the Aegean lithosphere (front part of the Eurasian plate) and that the oceanic-type lithosphere of the eastern Mediterranean, due to its greater density, subducts beneath the Aegean lithosphere. This convergence takes place along the Hellenic arc (Zakynthos - Crete - Rhodes) and specifically along its convex part (Papanikolaou and Sideris, 2007).

Reliable fault-plane solutions of surface earthquakes, combined with the observation of the spatial distribution of earthquake epicenters, led to the conclusion that the Aegean lithosphere and the surrounding area (i.e. within the inner part of the Hellenic arc) constitute the Aegean micro-plate, which extends in the N-S direction (McKenzie, 1972). The combination of satellite and geophysical data showed that the Aegean micro-plate performs a nearly linear motion, in a SW direction, with an increasing speed, along the same direction. As shown in Figure 1.2, the front part of the micro-plate, which overrides the eastern Mediterranean, moves at a speed of 3.5cm/yr, the middle part at a speed of $\simeq$2cm/yr and the rear portion, at an even smaller speed of approximately 1cm/yr (Papazachos et al., 1999).

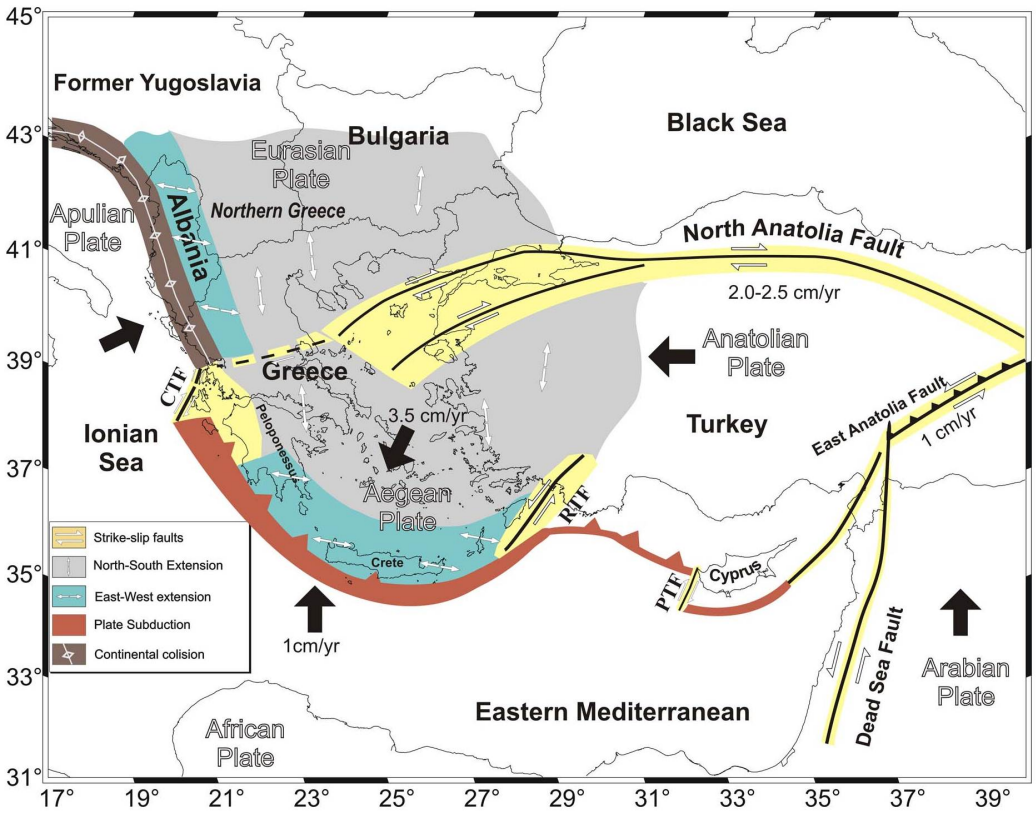

Figure 1.2: Main seismotectonic features of the broader Aegean area (Modified from Papazachos et al., 1998). Solid arrows depict plate motions, while white arrows show the local stress field and faulting pattern.

As a consequence of the previously described setting, Thessaly, which is located at the back-arc area of the Aegean micro-plate, has been shown to expand in a more-or-less N-S direction (see Figure 1.3), with a velocity of ∼1cm/year, due to the active stress field in the same direction. This extensional phase is the third tectonic phase recognized within the area (known as Quaternary-active extension) and it has been active from the middle Pleistocene to the present, hence, it is considered as the currently active tectonic phase of the area. The result of this expansion phase is the creation of normal faults with dominant E-W strikes, mainly along the southern and the northern borders of the Thessaly plain, forming two discrete rupture zones (see Figure 1.3). The faults of the northern Thessaly rupture zone, along Peneus river, are associated mainly with historical earthquakes with

magnitudes up to ~ 6.5, while their typical lengths do not exceed 25km. In the southern Thessaly rupture zone the faults are relatively larger (up to ∼50km), causing earthquakes up to M=7.0. Most of the southern Thessaly zone faults dip to the North while most of the northern Thessaly rupture zones dip to the South (Caputo and Pavlides, 1993; Mountrakis et al., 1993; Papazachos and Papazachou, 2002). This dominant E-W faulting pattern is also found along the western Thessaly border, were it co-exists with the N-S normal faults of the Hellenides mountain belt (Lekkas, 1987).

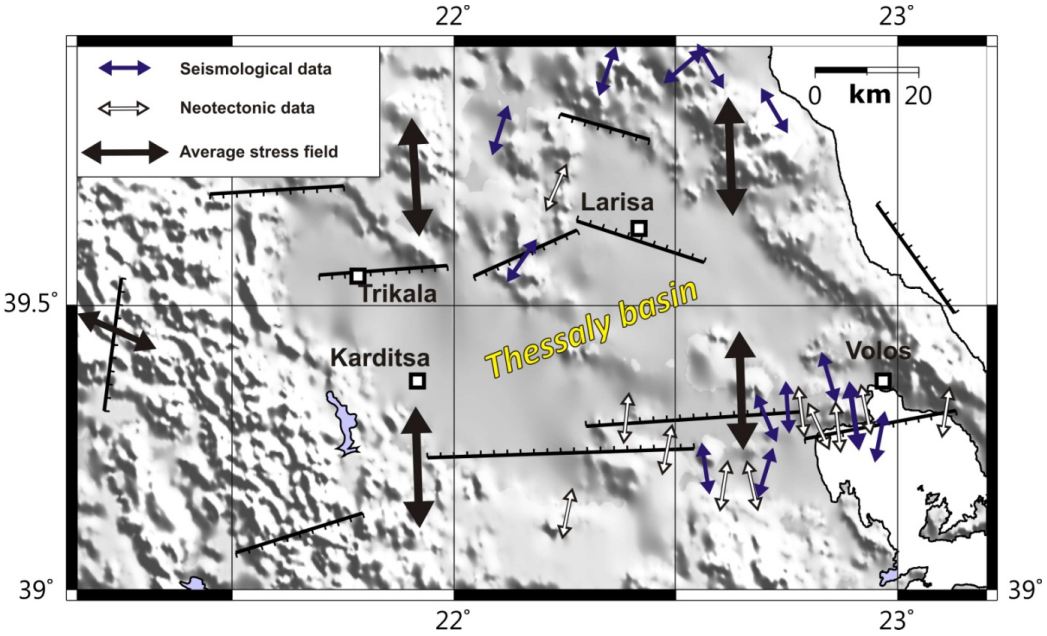

Figure 1.3: Extensional N-S trending stress field in the Thessaly basin, resulting in the generation of major active E-W striking faults (adopted from Papazachos et al., 2001). Small blue and white arrows denote T-axes from neotectonic and earthquake observations, respectively, while large black arrows depict the average stress field of the study area (modified from Panagiotopoulos and Papazachos, 2008).

The two (2) precedent tectonic phases of the Thessaly area are the compressional phase of the middle Miocene (ESE-WSW compression), followed by the late Miocene-Pliocene extensional phase (NE-SW extension, Caputo and Pavlides, 1993). As previously mentioned, a very interesting zone of normal faults, with a N-S direction, is identified along the inner part of the

Greek Arc. This zone extends between the outer compression zone and the inner part of the Aegean Sea, which is dominated by normal faults with an E-W direction. Furthermore, this zone can be associated with the creation of a sequence of extensional structures, which appear in the region of northern Peloponnese and western Crete, along this zone (e.g. faults of lake Ochrida, Prespes lakes, Konitsa, Kalamata, West and East Crete, Karpathos, etc.).

1.1.3 Geology

The Thessaly plain covers part of the Pelagonian and Subpelagonian geological zones. The area is characterized by strong stratigraphic complexity and tectonic deformation, of both the Alpine and the post-Alpine cycle. Specifically, the geological structures include Alpine, Molassic and post-Alpine formations.

The Alpine cycle formations fall into three (3) geotectonic units of the Greek area, namely the Pindos unit that is found in the western part of the basin and mainly on the Pindos mountain range, the western Thessaly unit, appearing in the western and southern Thessaly plain boundaries and, finally, the eastern Greece unit that is identified mainly in the East. The Alpine formations of the above units compile the geological background of the area, including a wide variety of lithological types, mostly characterized as rock formations (bedrock).

The Molassic formations of the Mesohellenic Trough are deposited according to the Alpine formations, appearing in the W / N-W Thessaly plain boundary. They contain mixed phases of clastic formations which can be classified as rocky if they are not weathered. At several places they exhibit a thick soil cover. The Neogene formations are deposited unconformably to the aforementioned formations. They are found mostly in the central part of the Thessaly area, containing a variety of lithological phases, with relatively low grade geotechnical properties. Finally, the Plio-Pleistocene and Quaternary formations are also deposited unconformably to all the aforementioned formations. These are mostly clastic formations that occupy the flat area of the Thessaly plain, including formations of lacustrine

and terrestrial lithological phases, both of which are characterized by very low geotechnical properties values, also containing aquifers (Lekkas, 1987, 1991; Papanikolaou and Sideris, 2007).

For the purposes of this study, geological formations of the area were hand-digitized using the available Greek Institute of Geology and Mineral Exploration (IGME) maps (scale 1:50.000). The layout of the digitized IGME geological maps is depicted in the Appendix (Figure A.1). The main geological formations were grouped into four classes according to their age, hence their expected dynamic amplification behavior:

1) Bedrock/Basement rocks (typically of Mesozoic-Paleogene age)

2) Molassic type sediments (Paleogene-Neogene age)

3) Neogene sediments

4) Quaternary-Plio/Pleistocene sediments

It should be noted that during the digitization and classification procedures, incompatibility between adjacent IGME maps was identified, regarding the geological characterization of formations (see Appendix Figure A.2). Those cases were handled separately, considering the detailed formation descriptions provided for each map, as well as the age and technology of the mapping procedures. Appropriate corrections were introduced for the formation grouping, using alternative geological maps, morphology and satellite imaging. The final Thessaly area grouped geological map, according to the proposed classification, is presented in Figure 1.4.

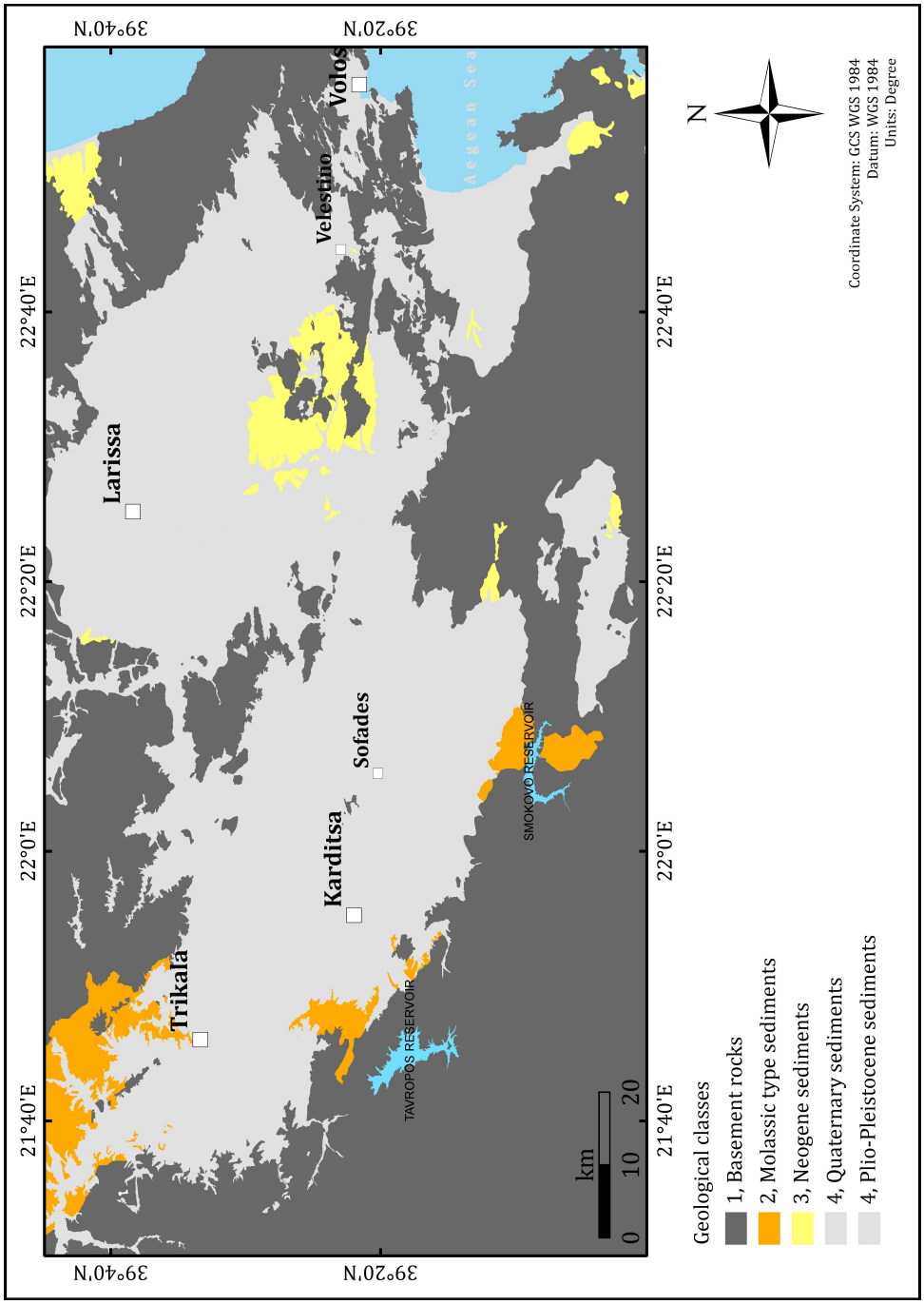

Figure 1.4: Grouped geological map for the broader Thessaly basin area, according to the classification adopted in the present study.

1.1.4 Seismicity

The Thessaly basin, has a well-known history of large earthquakes, with mainshocks having typical magnitudes between 6.0 and 7.0. The seismicity (instrumental and historic) follows the two discrete rupture zones of the Thessaly basin previously described (see Figure 1.3). The seismicity map of the Thessaly are is presented in Figure 1.5. During the 20th century, eight major seismic sequences with mainshock magnitudes equal or larger than 6.0 have occurred in this area (1905, 1911, 1930, 1941, 1954, 1955, 1957, 1980), with the M=7.0, 1954 Sofades earthquake being the most destructive event, resulting in heavy damages in the towns and villages of the broader southern Thessaly region (Papastamatiou and Mouyaris, 1986; Papazachos and Papazachou, 2002). The M=6.8, 1957 Velestino earthquake and the M=6.5, 1980 Almyros earthquake, are two equally notable events, with similarly destructive consequences.

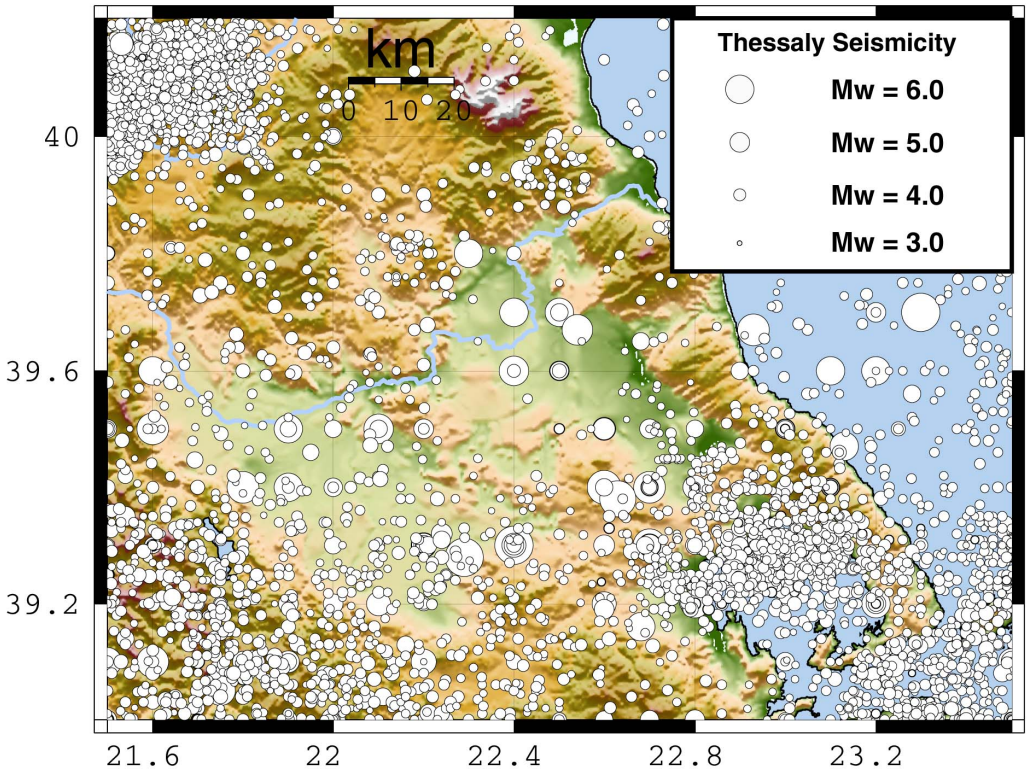

Figure 1.5: Seismicity map of the Thessaly area.

Table 1.1 presents the typical focal parameters of the eleven (11) faults of Thessaly (shown in Figure 1.3), that have caused earthquakes with M≥6.0 during historical times, as listed by Papazachos et al. (2001).

Table 1.1: Typical focal parameters of the eleven (11) faults of Thessaly, that have caused large earthquakes (M≥6.0) during historical times. The year and the moment magnitude (M) of each of these earthquakes are also given.

No	Name	Length	Strike	Dip	Year	M
1	Meteora	26	90	43	1544	6.4
					1665	6.0
					1787	6.0
2	Trikala	25	89	43	1621	6.0
					1674	6.0
					1735	6.4
3	Pinias	22	69	43	1661	6.2
4	Larissa	26	291	47	1668	6.0
					1731	6.0
					1781	6.2
					1941	6.3
5	Elassona	18	109	47	1766	6.1
6	Keramidi	26	327	50	1905	6.4
					1911	6.0
					1930	6.1
7	Agrafa	26	76	50	1514	6.0
					1566	6.4
					1966	6.2
8	Sofades	52	271	47	1954	7.0
9	Farsala	42	269	47	1743	6.6
					1773	6.4
					1957	6.8
10	N. Anchialos	30	82	43	1864	6.0
					1955	6.2
					1980	6.5
11	Arta	26	11	49	1967	6.4

The two (2) earthquakes examined in this study are the M=7.0, 1954 Sofades earthquake and the M=6.8, 1957 Velestino earthquake (activation

of Sofades and Farsala faults, respectively). Both faults are part of the southern rupture zone, with roughly E-W strike, dipping to the North.

The M=7.0, 1954 Sofades earthquake occurred on April 30, 1954, and its epicenter was located at 39.28^o N, 22.29^o E (see Figure 3.3). The aftermath's descriptions by Papastamatiou and Mouyaris (1986) and Papazachos and Papazachou (2002) report damages in the prefectures of Karditsa, Larisa, Trikala, Fthiotida, Magnesia and Evritania. Overall, 6599 buildings were completely destroyed, 9154 were heavily damaged and 12920 were lightly damaged, while the town of Sofades, in the Karditsa prefecture, was almost entirely destroyed. In total, 25 people were killed and 157 were injured. Also, ground fissures, liquefaction phenomena and hydrological changes were observed at several places. The largest foreshock occurred on April 25 (M=4.6), while the largest aftershock occurred on May 4 (M=5.7). The Sofades event marked the beginning of a series of earthquakes along the southern Thessaly rupture zone, that also involved the destructive events of 1955 and 1957, which mostly affected the city of Volos and the whole eastern part of the southern Thessaly basin (Papastamatiou and Mouyaris, 1986).

The M=6.8, 1957 Velestino earthquake occurred on March 8, 1957, and its epicenter was located at 39.38^o N, 22.63^o E (see Figure 3.9). The descriptions given by Papazachos and Papazachou (2002) reports serious damages in the prefectures of Magnesia, Larissa, Karditsa and Trikala. A total of 32701 buildings were damaged, 6934 of which collapsed, 10847 were seriously damaged and 14920 were lightly damaged. 2 people were killed while 71 were injured. A large foreshock (M=6.5) occurred a few minutes before the mainshock and its consequences cannot be distinguished from those of the mainshock. The largest aftershock (M=6.0) occured several hours after the mainshock.

Figures 1.6 and 1.7 show the macroseismic intensities distribution for the 1954 Sofades and 1957 Velestino earthquakes, respectively. Within the Thessaly area, observed intensities range from 5 to 9+ for the first, 1954 Sofades event and from 4 to 9+ for the second, 1957 Velestino earthquake.

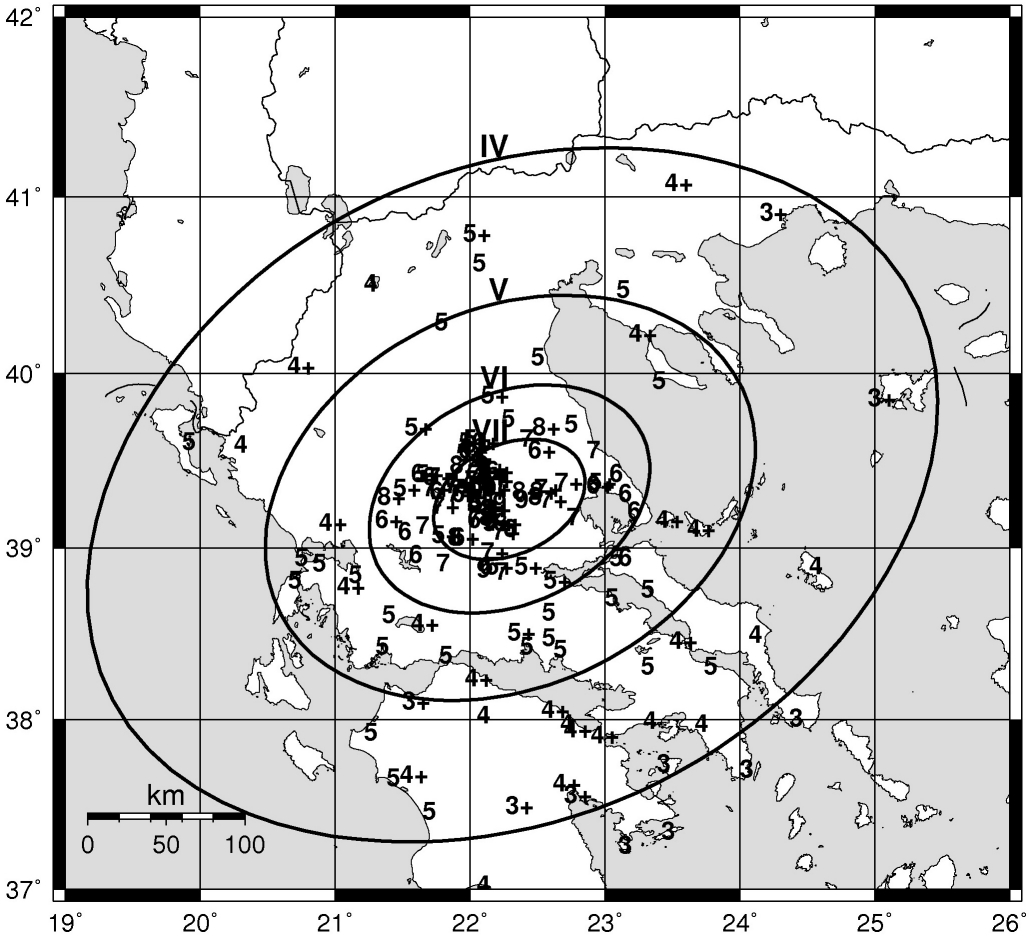

Figure 1.6: Isoseismals of the M=7.0, 1954 Sofades earthquake (Papazachos et al., 1997).

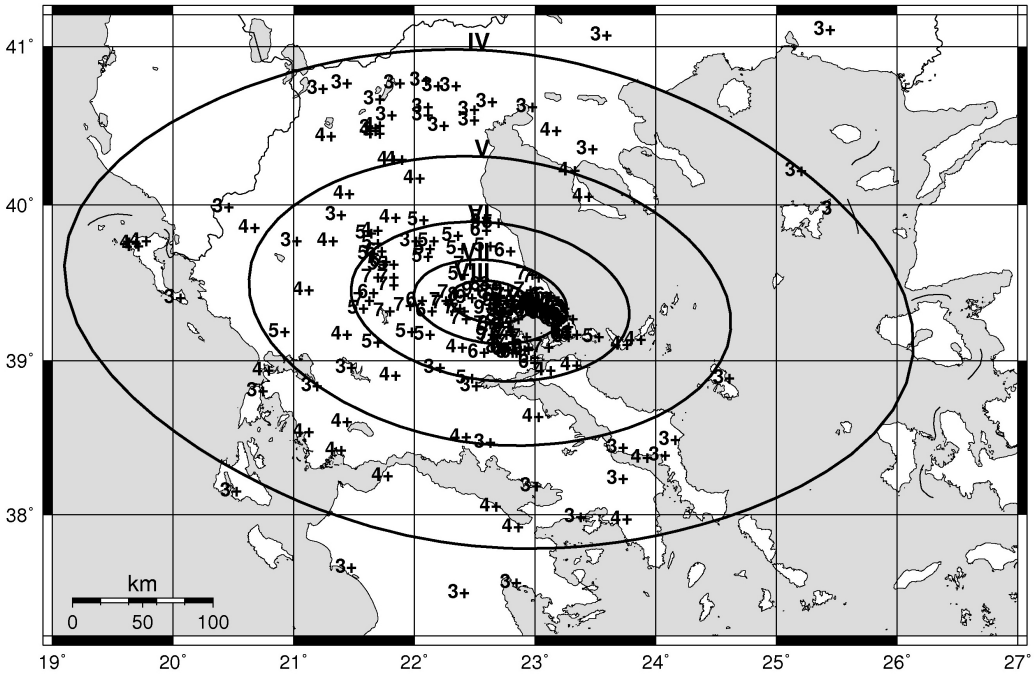

Figure 1.7: Isoseismals of the M=6.8, 1957 Velestino earthquake (Papazachos et al., 1997).

1.2 Contribution of local geophysical setting to ground motion (site-effects)

It is well known that the local soil conditions significantly affect the recorded seismic motions, since they can locally alter (in most cases amplify) the amplitude, frequency content and duration of seismic waves. As a result, the extent of seismic damage is determined not only by the seismic source properties and propagation path, but also by both the soil conditions and the technical construction parameters. Thus, knowledge of the local geological and geotechnical/geophysical structure is required for site-effect assessment and seismic-resistant design.

A key factor to assess the site response is the distribution of the shear wave velocity, V_s, of the uppermost sediments, since V_s provides an appropriate measure of the average soil stiffness. More particularly, the average V_s of the uppermost 30m (V_{s30}) is commonly used for site characterization

in ground response estimation (Borcherdt, 1994; Dobry et al., 2000). Direct measurement of V_s is feasible only through relatively high-cost procedures and in-situ tests (Crosshole, Seismic Cone, etc.). Thus, direct measurements are usually performed only at selected positions, since it is possible to estimate V_s at a site using alternative, commonly used geotechnical parameters (such as N_{SPT} blow counts, cone resistance values, etc.), which are typically collected during standard geotechnical investigations (Standard Penetration tests, Cone Penetration tests, etc.). This indirect estimation is usually performed through empirical equations, relating these geotechnical parameters to V_s (see later discussion in Chapter 2).

An increasingly popular low-cost procedure for site effect assessment used during the recent years is based on the use of ambient noise measurements and their analysis. In these methods, the constant, low-amplitude oscillations of the ground due to natural phenomena (microseisms, frequencies up to 1Hz) or human activities (microtremors, frequencies larger than 1Hz) are recorded through high-sensitivity seismometers. Based on these recordings, the horizontal to vertical spectral ratio (HVSR) is calculated to evaluate the ground's resonant frequency (f_0) and approximate the amplification factor (A_0) at this frequency (e.g. Haghshenas et al., 2008).

Within this study, site-effects were incorporated into the simulations using all available geological and/or geotechnical/geophysical data. Specifically, for the city of Karditsa, the availability of such data allowed the creation of the V_{s30} model for the urban area of the city. Moreover, ambient noise (HVSR) measurements were performed in selected positions within the broader Karditsa area, the analysis of which returned the resonant frequencies of the area's soil formations, while providing an indirect estimate for the amplifications and the expected sediments thickness range.

1.3 Stochastic simulation of seismic ground motion

The stochastic simulation method was initially proposed by Boore (1983) and then applied by a large number of researchers in order to simulate the ground motion from seismic sources (e.g. Boore and Atkinson, 1987; Toro and McGuire, 1987; Ou and Hermann, 1998; Atkinson and Boore, 1995). The method was originally developed as a point-source method (SMSIM). EXSIM is a modified stochastic simulation algorithm, using finite-fault modeling (like its predecessor, FINSIM, Beresnev and Atkinson, 1998), but with a dynamic corner frequency approach, as proposed by Motazedian and Atkinson (2005), including the near-fault ground motion model developed by Mavroeidis and Papageorgiou (2003). In EXSIM, the fault is divided into equal sized rectangular subfaults, considered as point sources. The ground motions are calculated for each subfault using the original point-source method and then summed at the observation point (target site). A simplified illustration of this procedure is presented in Figure 1.8, where a hypothetical fault is divided in 5x3 subfaults (each with dimensions dLxdw). In this example, the rupture begins at subfault (5,2) (blue star) and propagates throughout the fault's surface. When the rupture reaches a subfault, this subfault is treated as a separate fault, providing a unique synthetic stochastic record. These records are then summed into the complete stochastic record of the event at the selected simulation site.

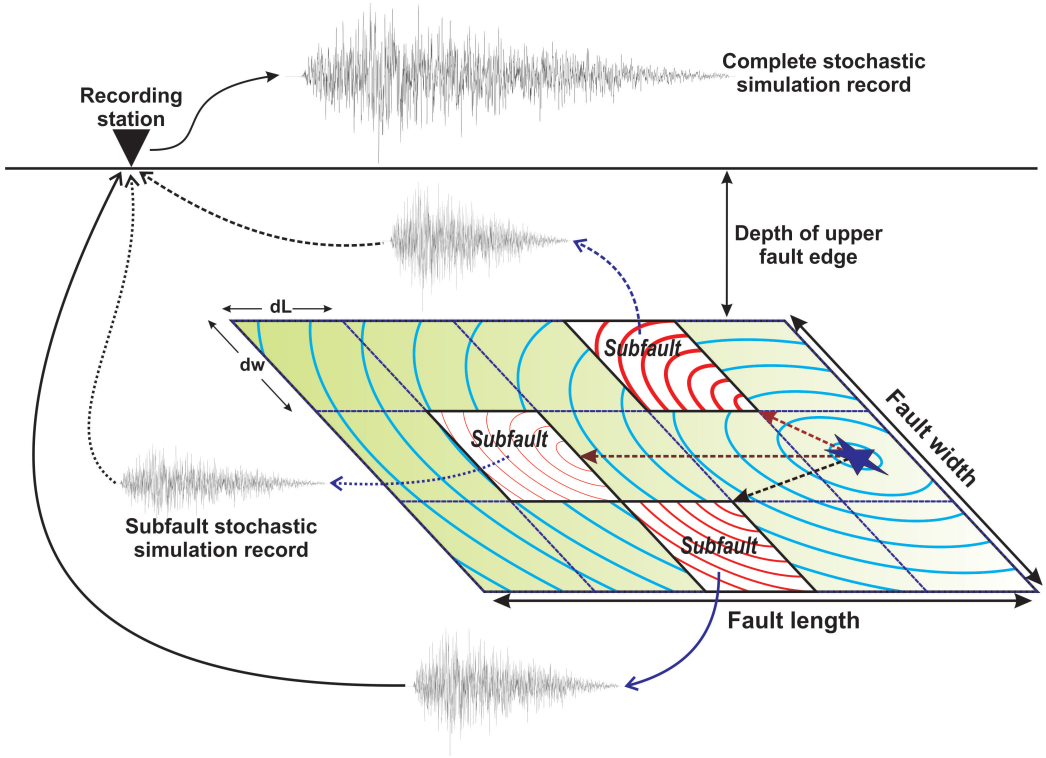

Figure 1.8: Simplified illustration of the seismic motion prediction procedure followed by the EXSIM algorithm.

The main advantage of the proposed approach is that it can reproduce realistic strong motion measures, although the modelled ruptures are specified by a few simple metrics, such as earthquake magnitude and distance, with options to include more detailed information on fault geometry and slip. In most cases, a random rupture scenario is considered for the simulations, though it is possible to introduce specific rupture scenarios (e.g. bi-directional, etc.).

In the present work, EXSIM was employed to generate synthetic time series for specified earthquake fault rupture scenarios, incorporating site-effects and leading to the estimation of Peak Ground Acceleration (PGA) and Peak Ground Velocity (PGV) from the synthetic time series. The PGA and PGV values were then used to estimate the expected macroseismic intensities (I_{MM}, Modified Mercalli scale) through empirical equations (e.g. Theodulidis and Papazachos, 1992; Tselentis and Danciu, 2008,

etc.). This makes it possible to indirectly estimate the seismic motions of even pre-instrumental earthquakes through the synthesized macroseismic observation results and estimate the ground motions for areas for which no macroseismic data are available.

(This page is left intentionally blank)

2.The urban area of Karditsa

2.1 Microzonation study and data collection procedure

The first target of the present work was to assess the site-effect for the city of Karditsa, by estimating the expected ground response in cases of strong ground motions due to earthquakes. In order to define the local geological and geotechnical / geophysical structures for the urban area, ground analysis data were obtained from the 1998 microzonation study (Lekkas, 1998), within which a large number of in-situ, geotechnical and geophysical tests took place at 23 locations within the urban area of Karditsa (see Figure 2.1). The obtained data included stratigraphic columns and Standard Penetration Test (SPT) blow counts (N_{SPT}) for 5 positions, cone resistance (q_c) and local friction (f_s) values from Cone Penetration tests (CPT) for 22 positions, shear wave velocity (V_s) values from Crosshole test (CH) for 1 position and V_s values from Seismic Cone tests (SC) for 3 positions. From Figure 2.1 it is clear that positions 1, 3 and 5 exhibit the highest data availability. Table 2.1 summarizes the tests conducted at each position, along with the maximum sampling depth of each test.

Figures 2.2-2.4 show typical examples from the original microzonation study documents for the tests conducted at Pos.1 (see Figure 2.1). Figure 2.2 shows the stratigraphic presentation, along with SPT and CH test results. Figure 2.3 shows the variation of cone resistance q_c and local friction f_s, as revealed from the CPT test. Finally, Figure 2.4 shows the S-wave arrival time variation with depth, from the SC test. It should be noted that the V_s values determined from the CH and SC tests were reassessed within the present study, using the measured q_c, f_s and S-wave travel time values.

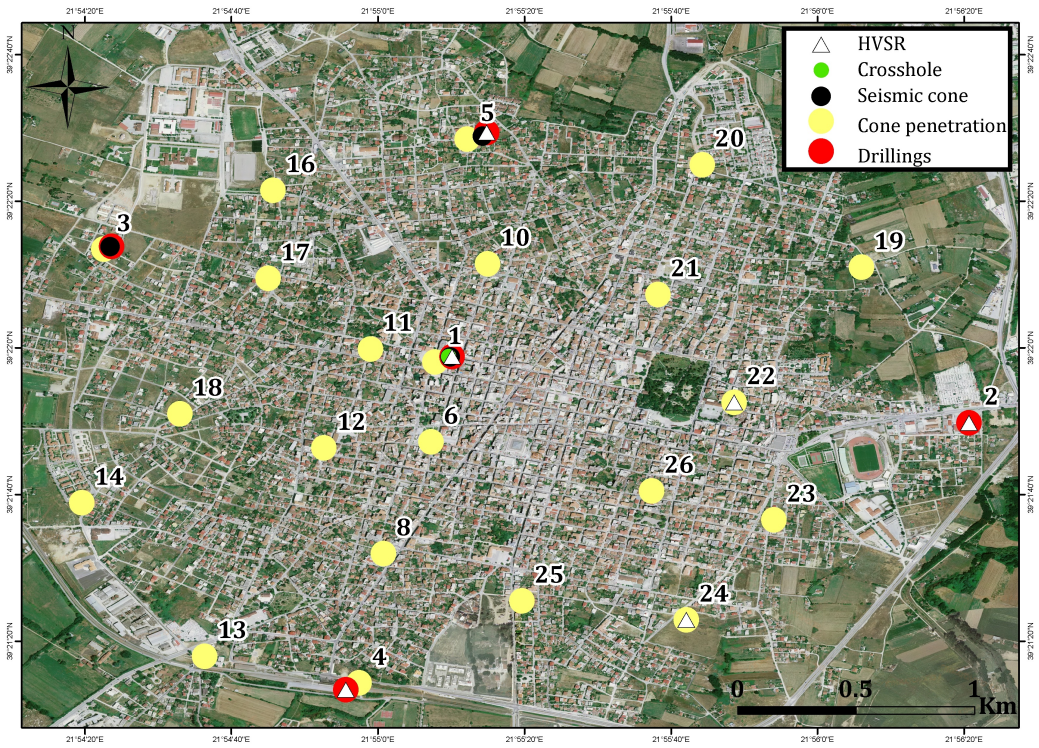

Figure 2.1: Karditsa 1998 microzonation study borehole sampling and test locations.

Table 2.1: Available geotechnical/geophysical tests and relative maximum sampling depths for all microzonation study positions (see Figure 2.1).

		Depths (m)			
Position(s)	Tests	Stratigraphy/SPT	CPT	CH	SC
1	SPT, CPT, CH, SC	70	30	58	24
2	SPT	50	-	-	-
3	SPT, CPT, SC	30	30	-	24
4	SPT, CPT	30	30	-	-
5	SPT, CPT, SC	30	30	-	18
6-26	CPT	-	30	-	-

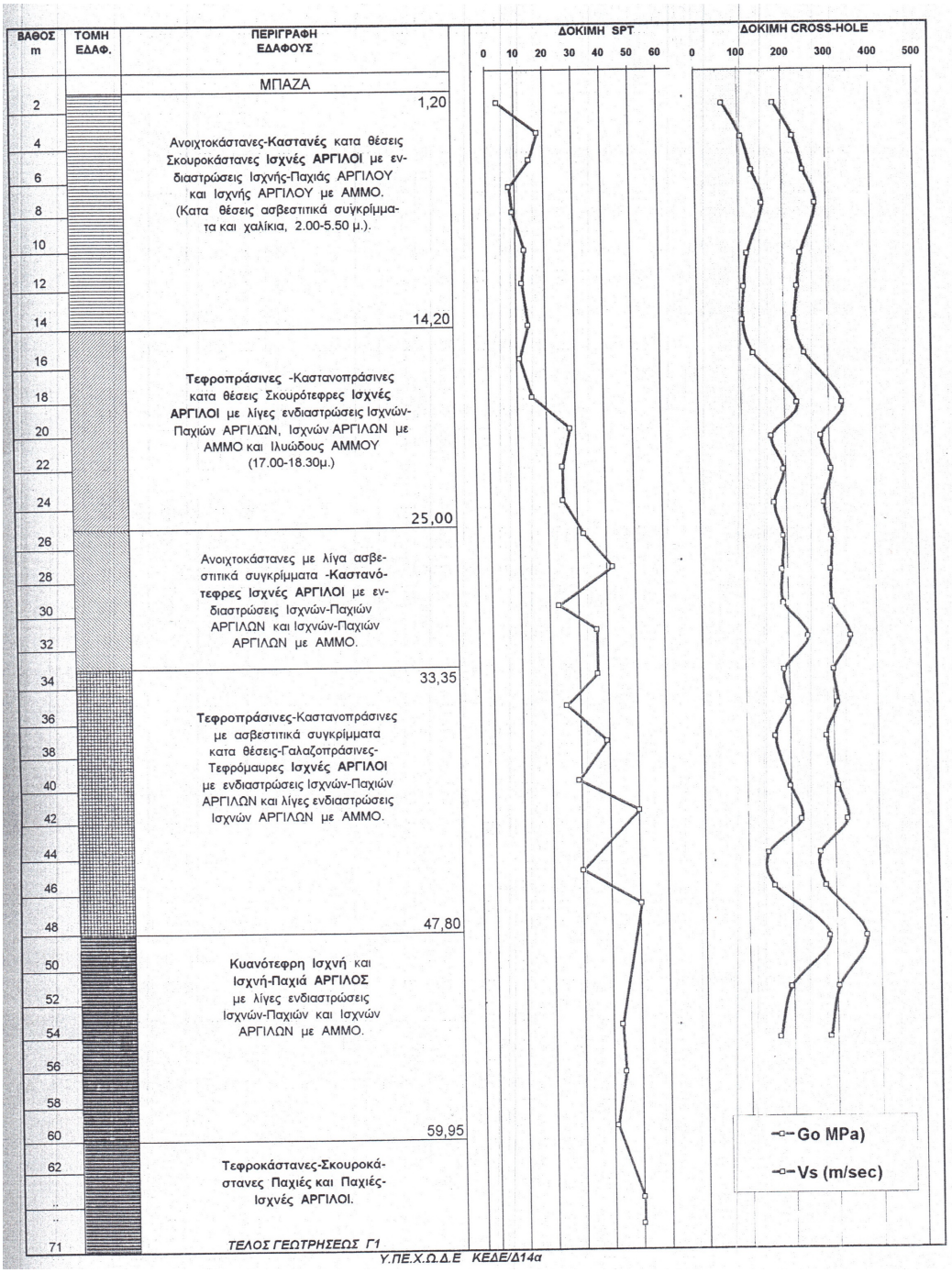

Figure 2.2: Original microzonation study document, presenting the stratigraphic log and results from Standard Penetration and Crosshole tests, for position 1 (see Figure 2.1).

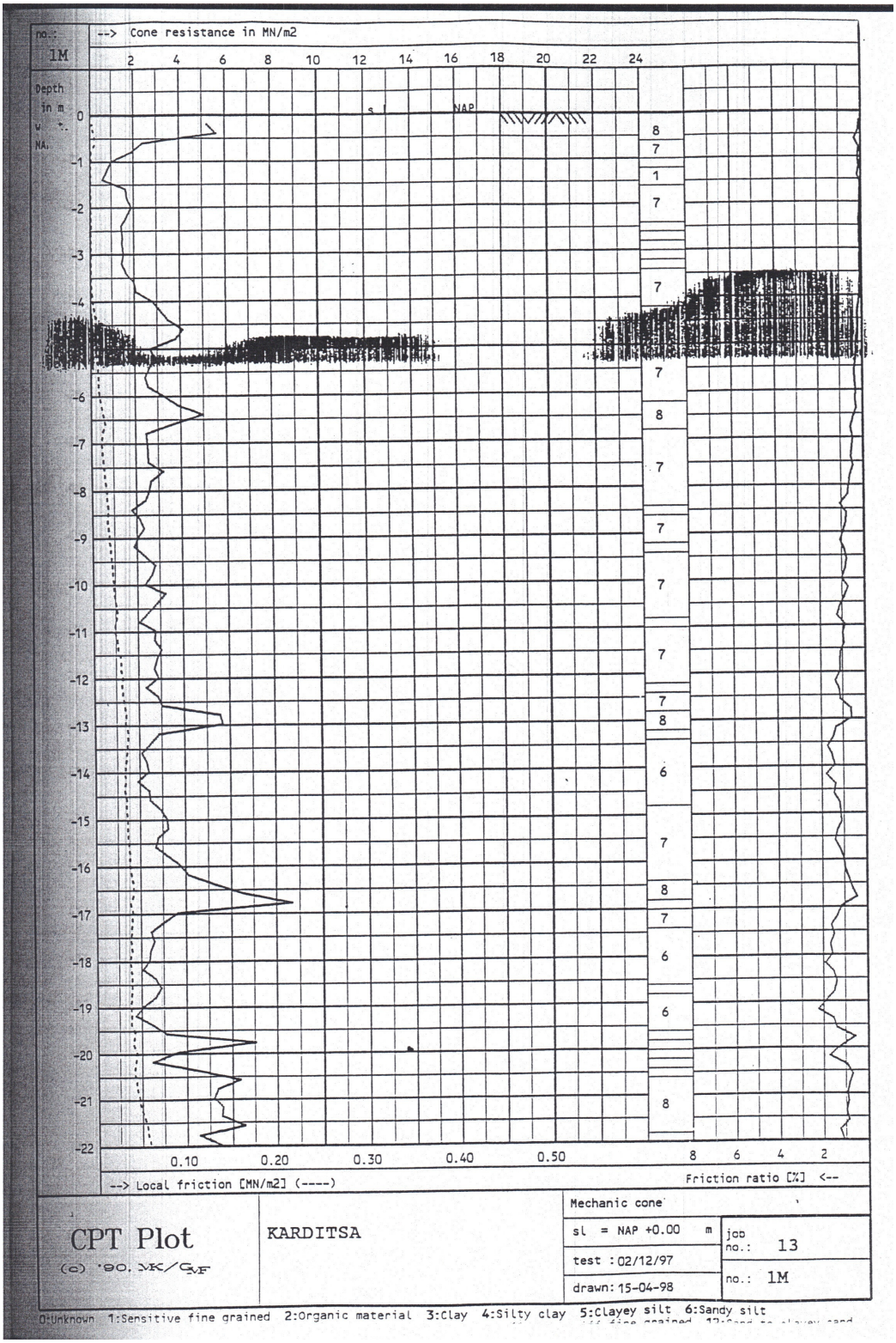

Figure 2.3: Original microzonation study document presenting Cone Penetration test results for position 1 (see Figure 2.1).

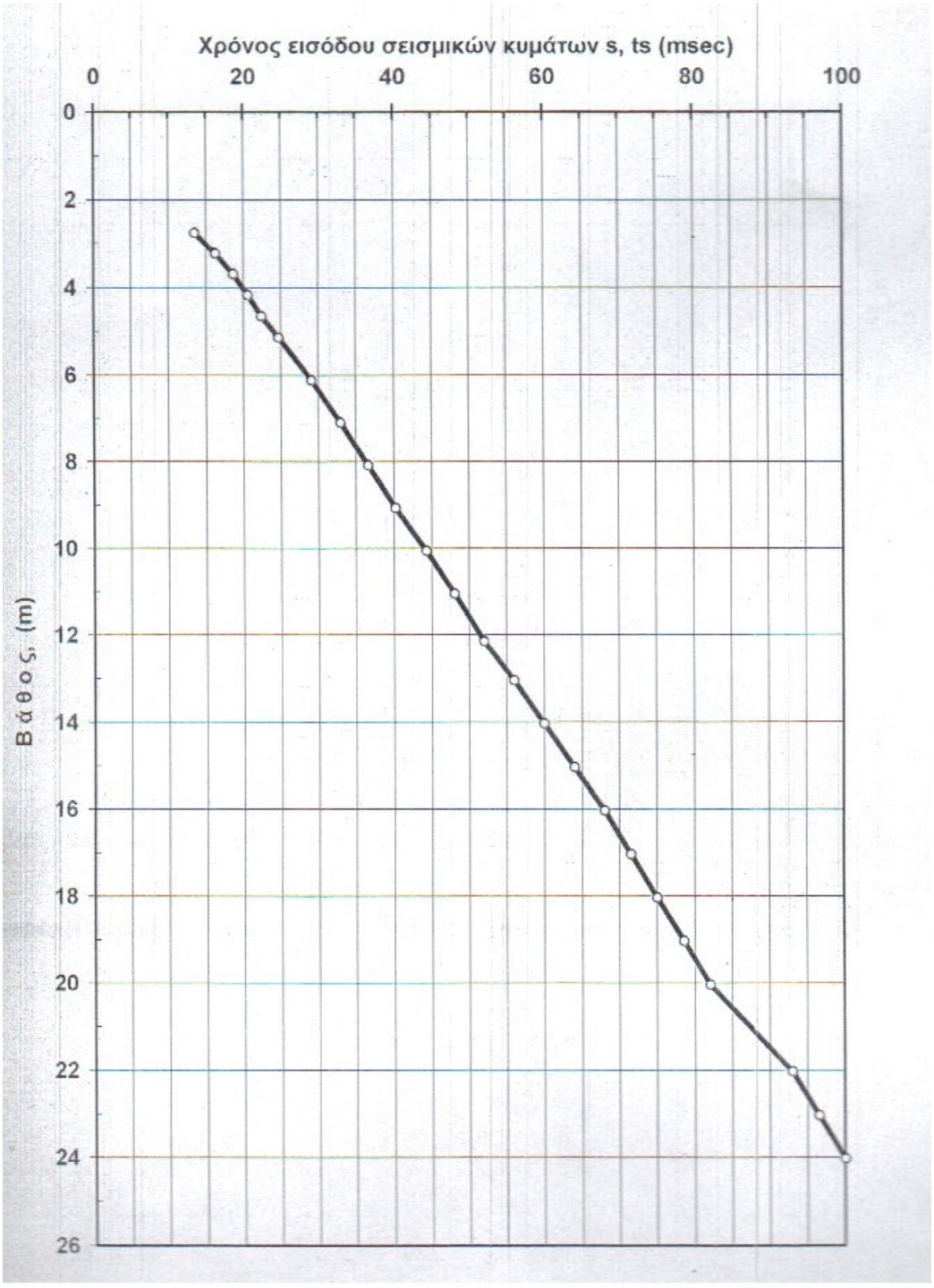

Figure 2.4: Original microzonation study document presenting Seismic cone S-wave travel time results for position 1 (see Figure 2.1).

2.2 Geological and geotechnical/geophysical setting

Initially, the collected microzonation data were used to assess the geological and geotechnical/geophysical setting for the urban area of the city of Karditsa. As can be seen in the grouped geological map of the broader study area (Figure 1.4), the city is built exclusively upon Quaternary alluvial deposits, mostly loose and unconsolidated. Stratigraphic columns (see Figure 2.2) were available for five (5) positions (see Table 2.1), showing the presence of seven soil layers within the uppermost 70m. Table 2.2 presents the soil structure at each position, the corresponding USCS classification and the main geotechnical parameters available and used in this study.

Table 2.2: Layer structure, USCS classification and major geotechnical properties of the seven (7) existing ground layers, for positions 1 - 5 (see Figure 2.1).

	Pos	Layer I	Layer II	Layer III
depth (m)	1	0.00-1.20	1.20-14.20	14.20-25
	2	0.00-1.80	1.80-11.10	11.10-21.95
	3	0.00-4.00	4.00-11.10	11.10-21.00
	4	0.00-5.05	5.05-17.00	17.00-28.00
	5	0.00-2.90	2.90-10.45	10.45-21.10
USCS classification		CL	CL, CL-CH, CH-CL, SC	CL, CL-CH, CH, SM
N_{SPT}		20	4-29	11-29
q_c (MPa)			1.7-2.0	2.0-2.1

	Pos	Layer IV	Layer V	Layer VI	Layer VII
depth (m)	1	25-33.35	33.35-47.80	47.80-59.95	59.95-70.45
	2	21.95-34.15	34.15-50.95		
	3	21.00-33.15			
	4	28.00-32.45			
	5	21.10-32.75			
USCS classification		CL, CL-CH, CH-CL	CL, CL-CH, CH	CL, CL-CH, CH	CL, CH-CL, CH
N_{SPT}		17-42	23-50	44-50	>50
q_c (MPa)		>3			

Table 2.2 shows the coexistence of inorganic, lean, low-to-medium plasticity clays (CL) and inorganic, fat, high-plasticity clays (CH), within most layers, apart from Layer I (0m to 1-5m), where only lean clays exist. Clayey sand and silty sand are found only in Layers II and III ($\sim 3m - \sim 25m$). A slight improvement of soil mechanical characteristics with depth is observed from the increase of the N_{SPT} counts and the corresponding cone resistance values.

2.3 V_{s30} model for the Karditsa area

In order to estimate the ground motions within the urban area of Karditsa, the V_{s30} model of the area was created and used for site characterization. Direct V_s measurements were available only for positions 1, 3 and 5 (see Figure 2.1 and Table 2.1), from Crosshole (Pos.1 only) and Seismic Cone tests conducted within the 1998 microzonation study. All positions had CPT data available, apart from Pos.2 where only SPT data were available. This suggested that it was possible to estimate V_s values from N_{SPT} blow counts (for Pos.2) and from q_c and f_s values (for all remaining positions), in order to obtain V_s values for a subsurface 3D grid within the urban Karditsa area.

Tables 2.3 and 2.4 show some of the existing empirical equations correlating these common geotechnical parameters to V_s. In order to employ these equations, it was necessary to test their applicability for the examined case. For this reason, positions 1, 3 and 5 were considered as the most appropriate to be used as reference for this comparison, since direct V_s measurements were available only for these sites.

Table 2.3: Existing empirical equations for the estimation of V_s values from N_{SPT}.

Author(s)	All soils	Clays
Athanasopoulos (1995)	$V_s = 107.6N^{0.36}$	-
Pitilakis & Anastasiadis (1998)	$V_s = 132(N_{60})^{0.271}$	-
Hasancebi & Ulusay (2007)	$V_s = 90N^{0.309}$	$V_s = 97.9N^{0.269}$
Dikmen (2009)	$V_s = 58N^{0.39}$	$V_s = 44N^{0.48}$

N: number of blow counts, V_s in (m/s)

Table 2.4: Existing empirical equations for the estimation of V_s values from q_c, f_s and depth(Z).

Author(s)	Clays
Tsiambaos & Sabatikakis (2010)	$V_s = 176 q_c^{0.557}$
Andrus et al. (2003)	$V_s = 6.21 q_c^{0.444}$
	$V_s = 9.93 q_c^{0.338} f_s^{0.078}$
	$V_s = 9.72 q_c^{0.333} f_s^{0.084} Z^{0.023}$

q_c and f_s in MPa for Tsiambaos, KPa for Andrus, Z in m, V_s in m/s

For positions 1, 3 and 5, all of the above equations were used to estimate V_s from N_{SPT}, q_c and f_s. The Seismic Cone tests (available for all three positions) and the Crosshole test (position 1 only) which were used to obtain direct V_s measurement, showed that V_s values ranged between 200-300m/s for all three positions. As can be seen from Figures 2.5, 2.6 and 2.7, there is a poor correlation between V_s measured by SC and CH and V_s estimated from the equations listed in tables 2.3 and 2.4. Regarding the V_s estimation from N_{SPT} (see Table 2.3), the equations of Athanasopoulos (1995) and Pitilakis and Anastasiadis (1998) lead to overestimation, while the ones of Dikmen (2009) and Hasancebi and Ulusay (2007) lead to underestimation of V_s for all three positions. When employing equations to estimate V_s from q_c and f_s (see Table 2.4), all the equations of Andrus et al. (2003) underestimate the measured V_s values, while the equation of Tsiambaos and Sabatikakis (2010) return higher values for most depths. This suggested that it was necessary to estimate new, locally applicable, equations correlating V_s to these common geotechnical parameters, which would result in a reliable V_s estimation for the urban area of Karditsa.

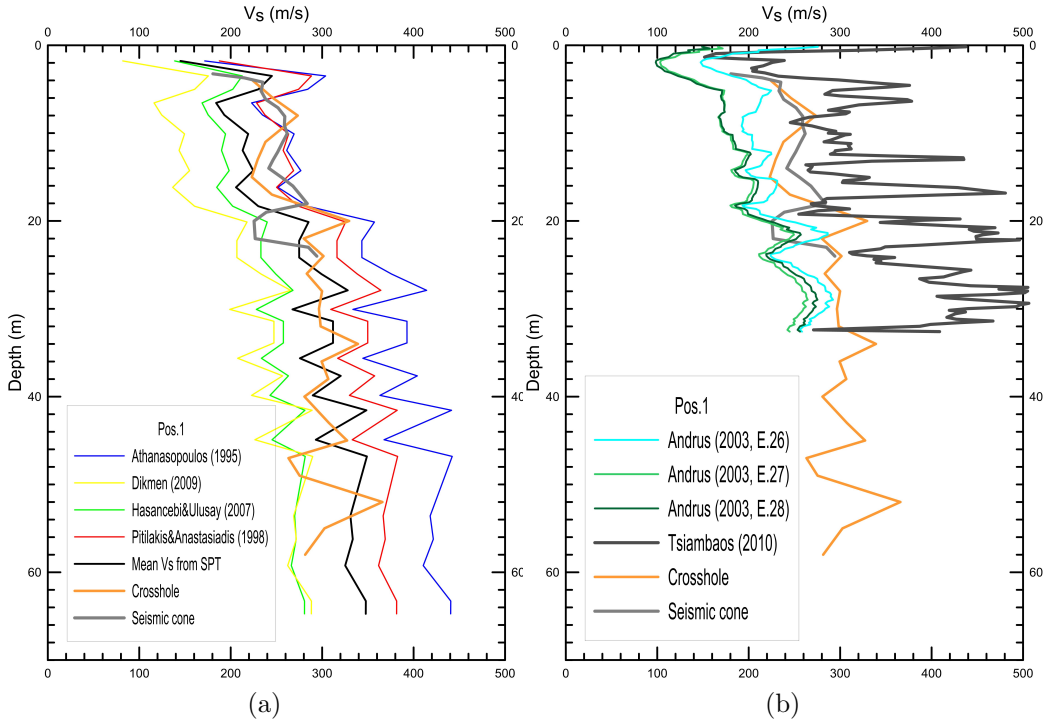

Figure 2.5: Comparison of directly measured V_s values against those estimated from existing calibrating equations, for Pos.1 (see Figure 2.1). (a) V_s values estimated from SPT relations. (b) V_s values estimated from CPT relations.

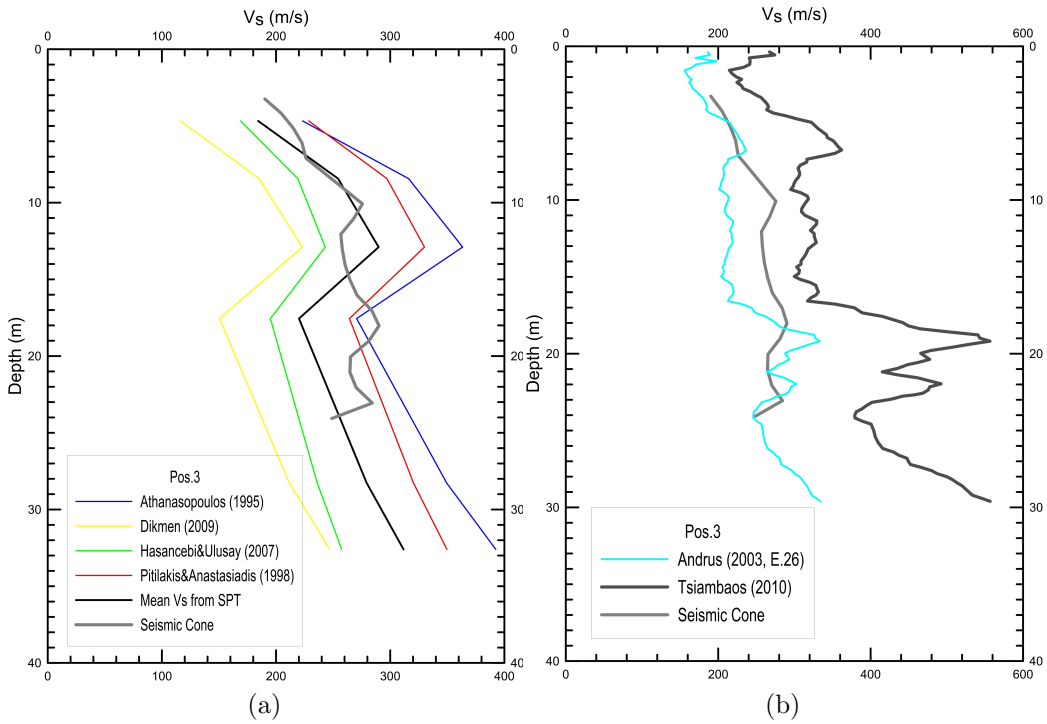

Figure 2.6: Same as Figure 2.5, for Pos.3.

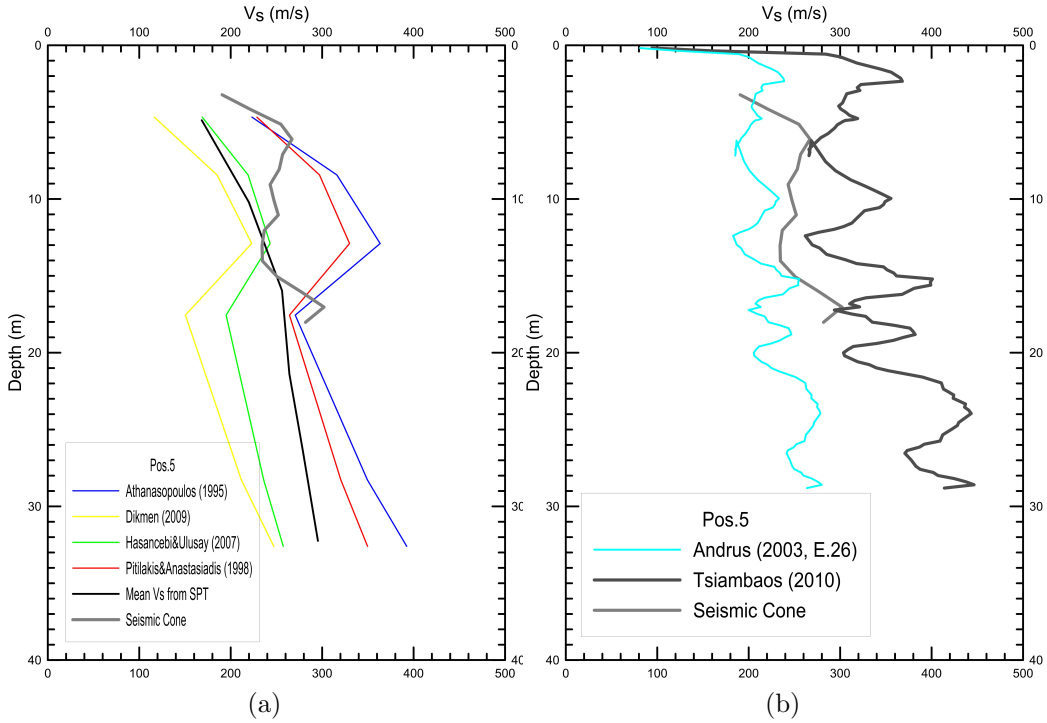

Figure 2.7: Same as Figure 2.5, for Pos.5.

Using the reference positions 1, 3 and 5, the first step for calculating the new equations was to linearly interpolate (using a developed MATLAB script) the N_{SPT}, q_c and f_s values, for the depths of available V_s measures from Seismic Cone (positions 1, 3 and 5) and then for the depths of V_s measurements from Crosshole (Pos.1 only). It should be noted that higher-order interpolation methods were tested (cubic, etc.) but resulted in very similar results with the linear interpolation. Considering the geological uniformity of all three examined positions, the interpolation results were unified into one dataset, containing values for the geotechnical parameters N_{SPT}, q_c and f_s along with measured V_s values, for all available depths. This allowed to plot each parameter against the measured V_s value for all depths, in order to derive the new correlation equations from the corresponding plots (Eq.2.1, Eq.2.2 and Eq.2.3). The $N_{SPT} - V_s$, $q_c - V_s$ and $f_s - V_s$ plots, along with the corresponding equations are presented in Figures 2.8, 2.9 and 2.10, respectively. Moreover, the correlation of the estimated V_s values using the

new equations with the measured ones from the 1998 microzonation study (for positions 1, 3 and 5) is presented in Figure 2.11.

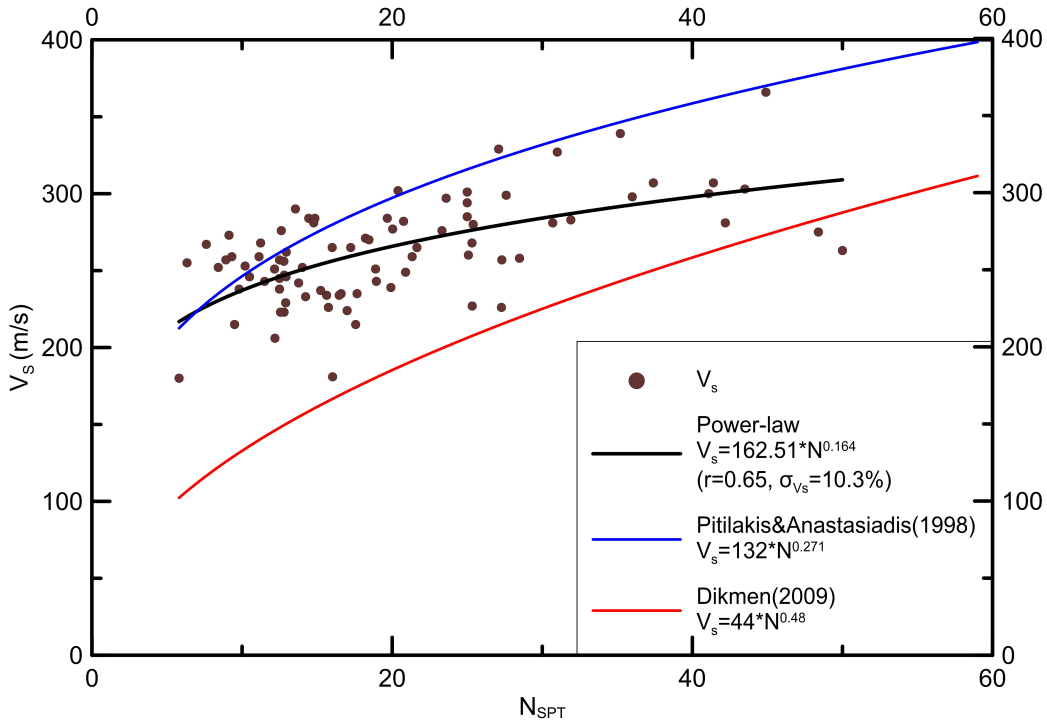

Figure 2.8: Correlation of interpolated N_{SPT} values to the measured V_s values (for the reference positions 1, 3 and 5). The corresponding determined equation is also presented, in comparison to other previously proposed ones.

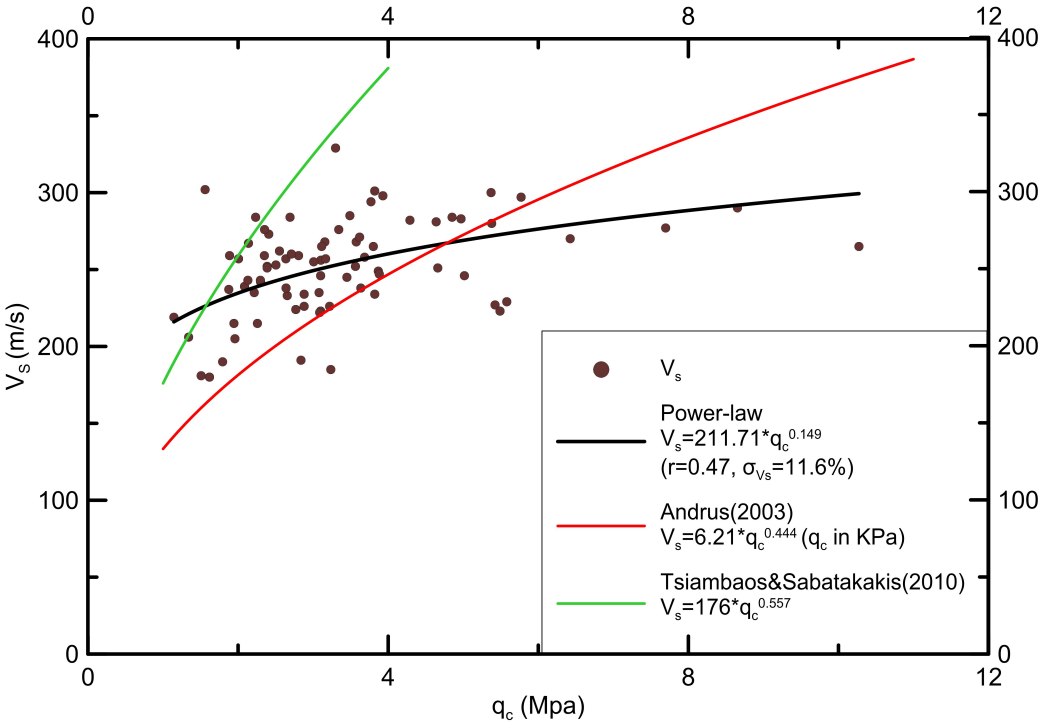

Figure 2.9: Same as Figure 2.8 for interpolated q_c values.

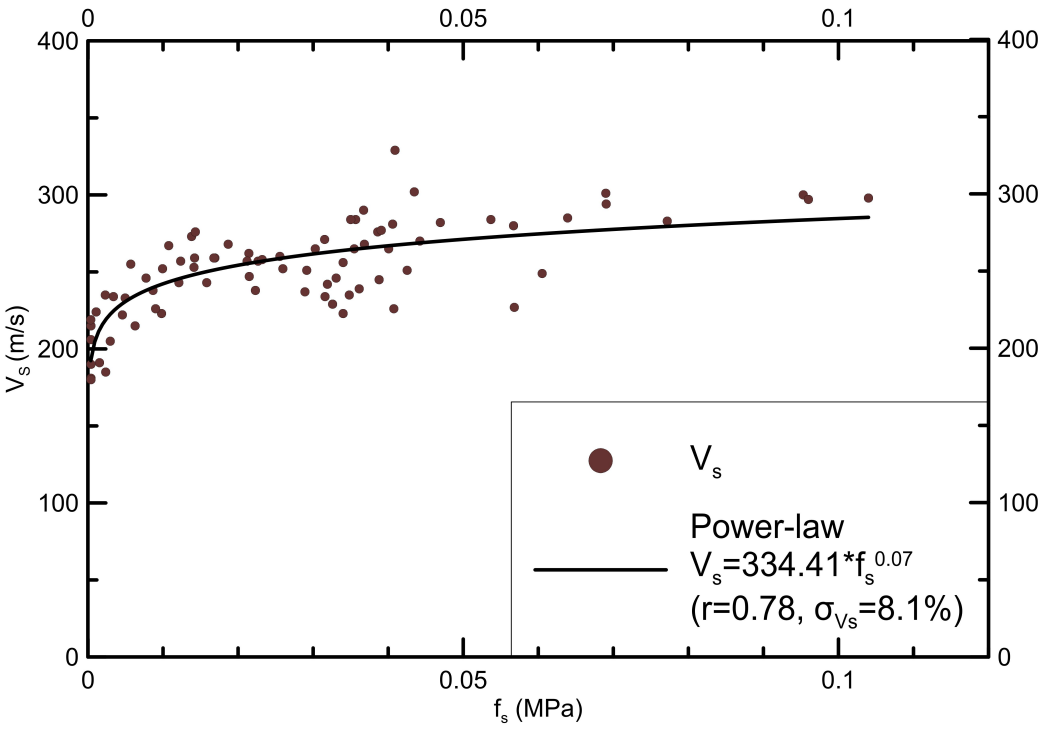

Figure 2.10: Same as Figure 2.8 for interpolated f_s values.

$$V_s = 162.51 * N^{0.164} \tag{2.1}$$

$$V_s = 211.71 * q_c^{0.149} \tag{2.2}$$

$$V_s = 334.41 * f_s^{0.07} \tag{2.3}$$

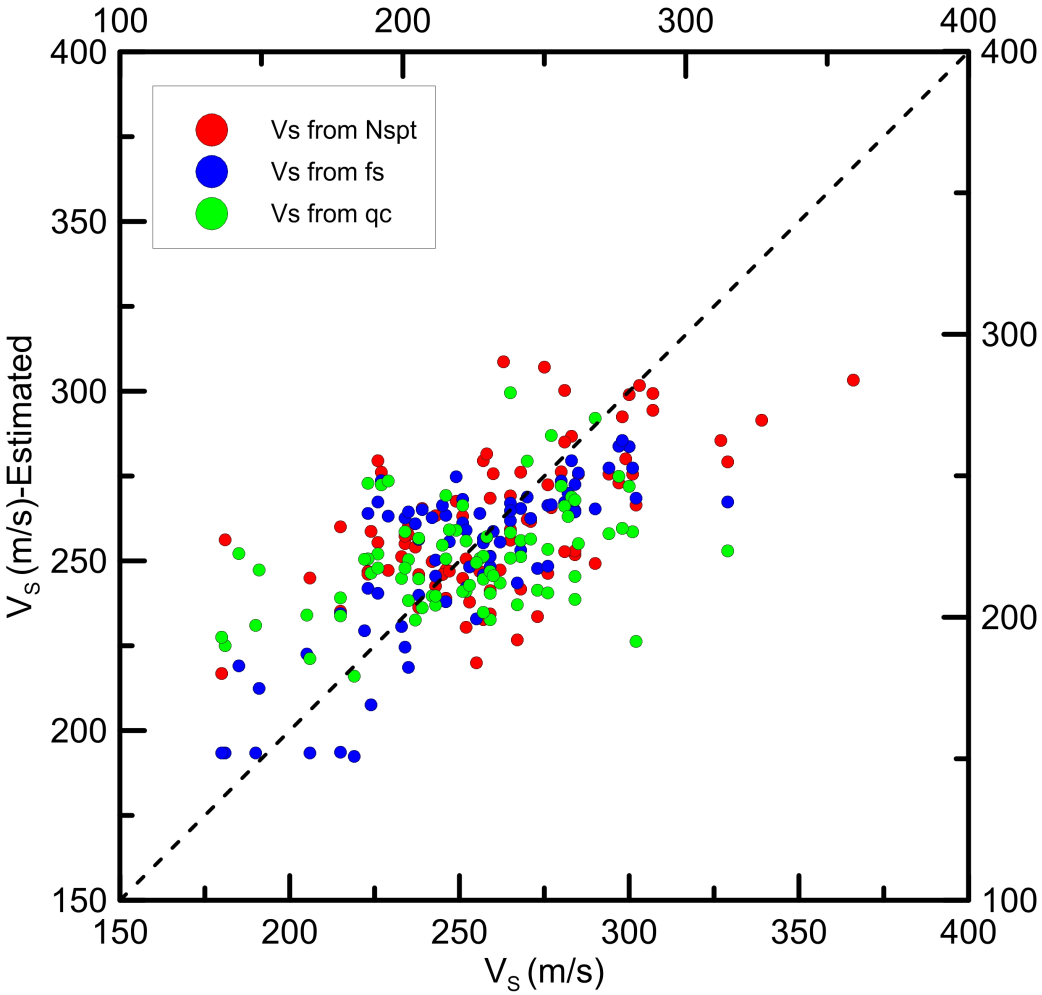

Figure 2.11: Comparison of the estimated V_s values from equations 2.1, 2.2 and 2.3 determined for the Karditsa area, with the measured V_s values of the 1998 microzonation study (for the reference positions 1, 3 and 5).

It is clear from Figure 2.11 that the estimated V_s values correlate better to measured V_s when using f_s values (Eq.2.3) compared to q_c (Eq.2.2). Thus, Eq.2.3 was used to estimate V_s for all remaining positions (4 and 6-26). For position 2, Eq.2.1 was used since only SPT data was available for this site. It should be noted that the final V_s for each position at each depth, is the average of all (measured or estimated) available V_s values. Table 2.5 gives an indication of the final V_s calculation, for position 3 and depths from ∼2m to 13m.

Table 2.5: Calculation of the final V_s values, for position 3 and for the depth range ∼2m to 13m. $V_s - SC$: Measured V_s from Seismic Cone test. N_{SPT}: Number of blow counts from Standard Penetration test. f_s: Local friction (MPa) from Cone Penetration test. $V_s - N_{SPT}$: V_s estimated using Eq.2.1. $V_s - f_s$: V_s estimated using Eq.2.3. final V_s: Average of $V_s - SC$, $V_s - N_{SPT}$ and $V_s - f_s$.

Depth(m)	$V_s - SC$	N_{SPT}	f_s	$V_s - N_{SPT}$	$V_s - f_s$	final V_s
2.3	219		0.0004		192	206
3.3	190		0.0004		193	192
4.2	205		0.0030		223	214
5.1	215	9.5	0.0063	235	234	228
6.1	223	12.6	0.0098	246	242	237
7.1	226	15.8	0.0090	255	240	241
8.1	243	18.9	0.0121	263	246	251
9.1	259	21.3	0.0168	268	251	260
10.1	276	23.3	0.0143	272	248	266
11.1	268	25.3	0.0187	276	253	266
12.1	257	27.3	0.0212	280	255	264
13.1	258	28.5	0.0232	281	257	265

The final V_s values for each position were then interpolated for the depth range 2m-30m (with a 2m step), resulting in V_s spatial grids for each of the interpolation depths. Figure 2.12 presents the V_s models for the depths of 2m, 10m and 28m, indicating that V_s ranges from ∼200-300m/s for all depths (the V_s spatial grids for the remaining depths can be found in Appendix Figures A.3 - A.6). The average V_S for depths 0-30m at all positions was calculated and was used to create a 3D V_s model for the

uppermost 30m of the urban Karditsa area. Moreover, using the relation:

$$V_s^{30} = \frac{30}{\sum_i^{30} V_s^i} \tag{2.4}$$

where V_s^i (i=1,...30) are the V_s values for each depth in the range 1-30m, the V_{s30} model for the urban area of Karditsa was defined and presented in Figure 2.13.

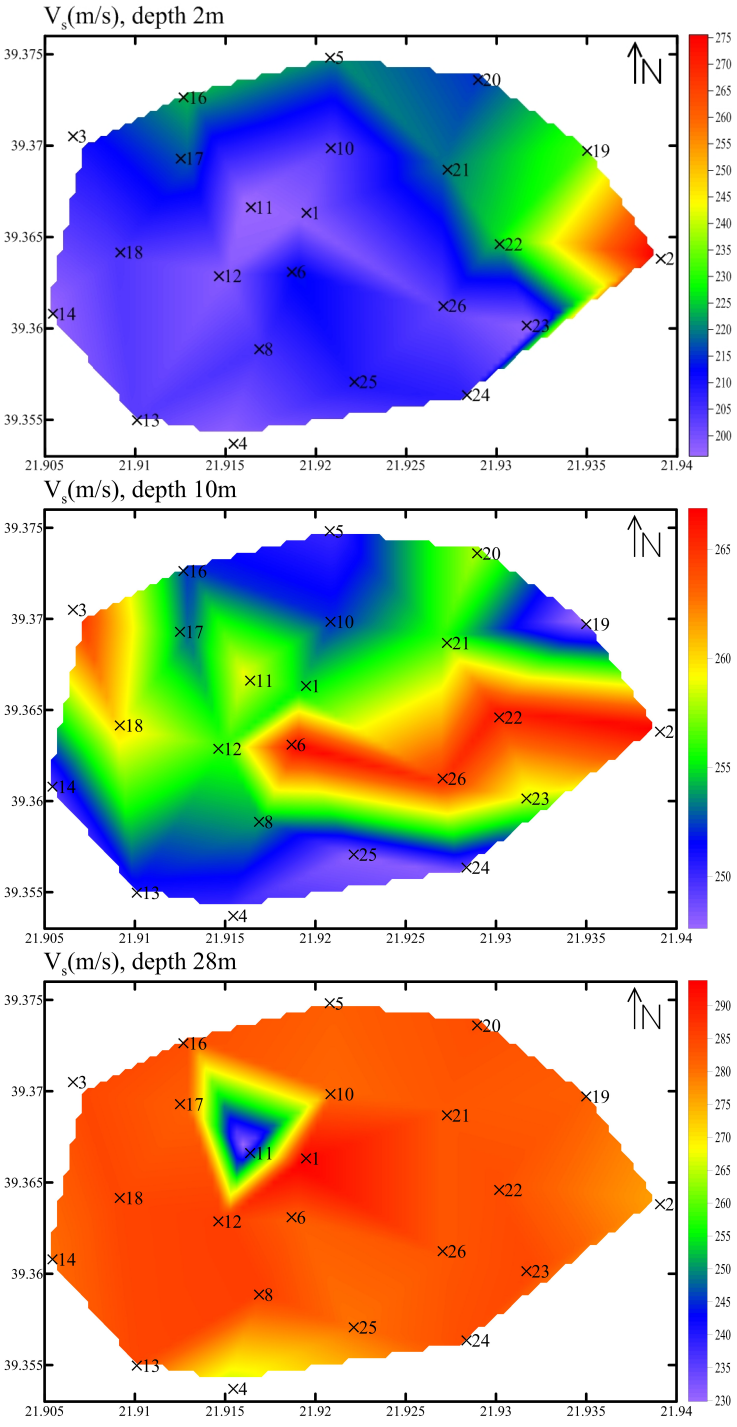

Figure 2.12: V_s models for the depths of 2m, 10m and 28m, for the urban area of Karditsa.

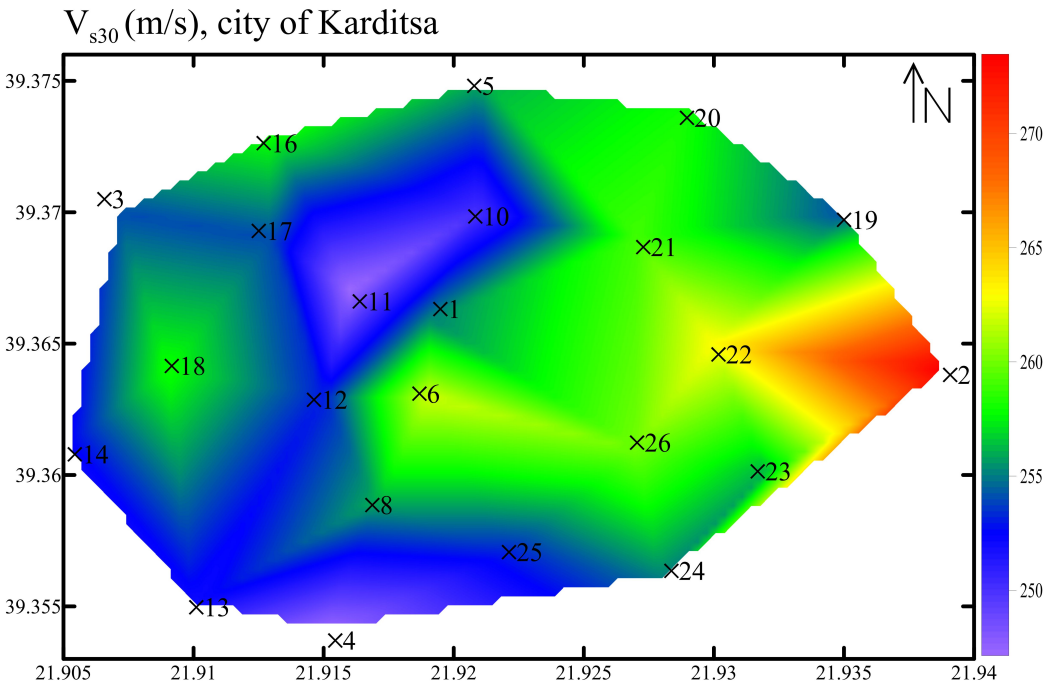

Figure 2.13: The calculated V_{s30} model for the urban area of Karditsa. 1998 microzonation study test positions are also depicted.

From Figure 2.13 it is obvious that there is limited spatial variation of the V_{s30} throughout the urban area of Karditsa, with values ranging from ∼250m/s to ∼275m/s. More significant variations are observed for the uppermost layers (2m, Figure 2.12), where higher values are found for the eastern part of Karditsa city. This was partly expected, considering the geological, geophysical and geotechnical uniformity within the study area.

2.4 HVSR measurements

In order to better understand the geophysical setting of the urban Karditsa area, fourteen (14) HVSR measurements were performed at selected positions within the city and its broader area (see Figure 2.15). The first six (6) measurements (grey triangles in Figure 2.15) were performed first, very close to positions 1, 2, 4, 5, 22 and 26 of the 1998 microzonation study tests (see Figure 2.1). The recovered resonant frequencies from these initial measurements exhibited values in the range of ∼0.35-0.4Hz, showing a

slight increase towards the East and a more significant gradual increase towards the South. Figure 2.14 presents the HVSR variation with frequency for two (2) positions within the urban Karditsa area (both show resonant frequencies at ∼0.35-0.4Hz). The increase of f_0 towards the south indicated the reduction of Quaternary sediments thickness towards the same direction, which can be also expected from the general geological setting of Thessaly (Figure 1.4), due to the appearance of bedrock formations towards the East of Karditsa (at a relatively small distance of ∼10km) and to the South (∼6km). To verify this assumption, eight (8) additional HVSR measurements were performed along these directions (white triangles in Figure 2.15), exhibiting higher resonant frequencies (up to 1.25Hz) towards the bedrock formations.

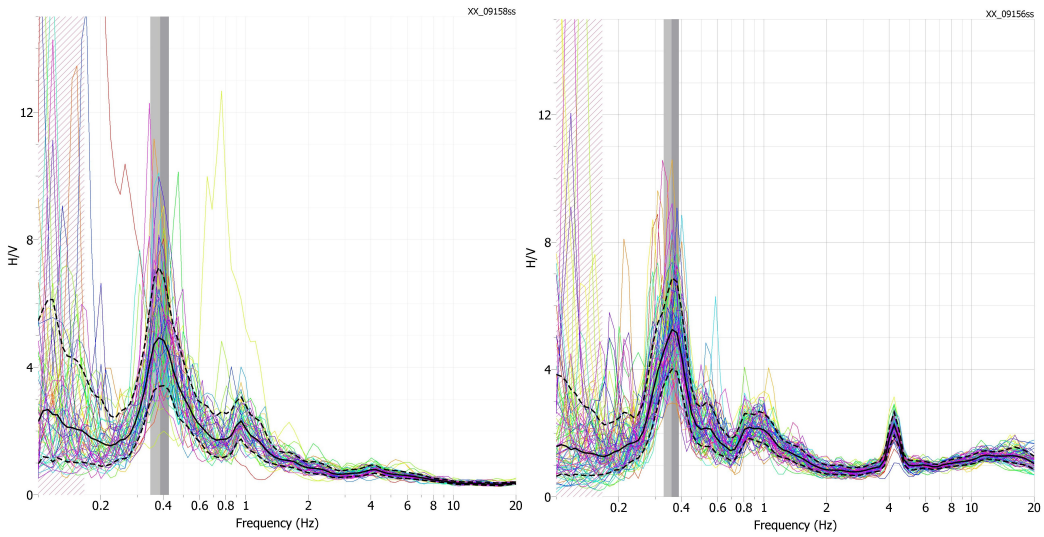

Figure 2.14: HVSR spectral plots (data processing with the Geopsy software), showing a low resonant frequency (∼0.35-0.4Hz) for two different positions within the urban Karditsa area (Quaternary formation sites).

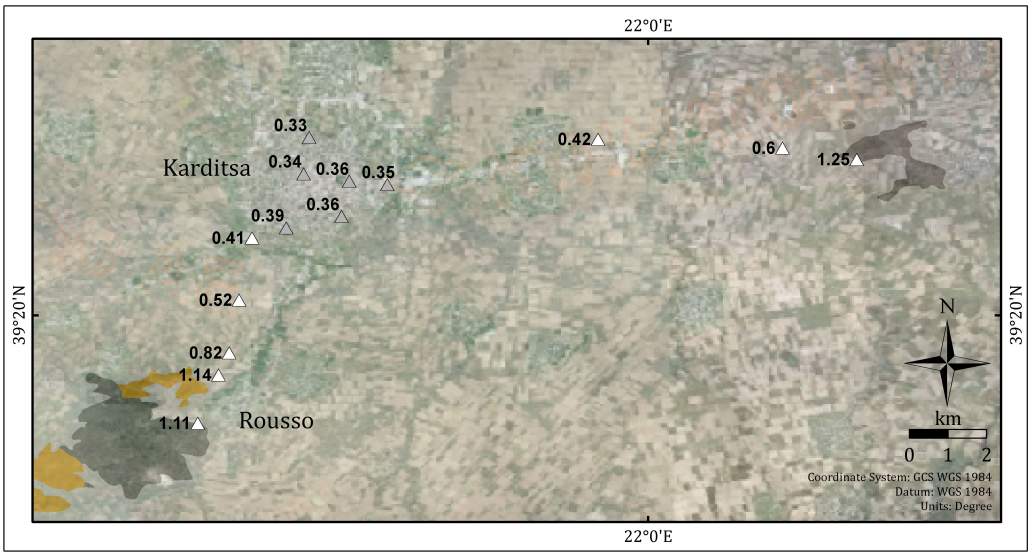

Figure 2.15: Positions of HVSR measurements performed within the urban Karditsa and the broader Karditsa area. The bedrock formations (grey color) and Molassic formations (orange color) are superimposed on the map, while the resonant frequency (f_0) for each position, as determined from HVSR data, is also presented.

Considering the significant thickness of the Quaternary deposits within the urban Karditsa area and the uniformity of the V_{s30} model, it becomes evident that the ground response to seismic motion is not expected to significantly vary within the city. Thus, a more generic approach was adopted, in which the seismic motions of strong historical earthquakes would be employed, aiming at the estimation of macroseismic intensities, I_{MM} (Modified Mercalli scale), for positions throughout the broader Thessaly plain area.

(This page is left intentionally blank)

3.Stochastic simulation

3.1 Stochastic simulation methodology

The seismic motions of two damaging earthquakes along the southern Thessaly zone were stochastically simulated, namely, the M=7.0, 1954 Sofades earthquake and the M=6.8, 1957 Velestino earthquake. Macroseismic data for both events were collected from the published database of macroseismic information for the Aegean area (Papazachos et al., 1997), in order to reconstruct the observed intensities distribution among the settlements of the broader Thessaly area. It is clear that due to the scale of the study area, geophysical and geotechnical information could not be employed for detailed assessment of site-effect. For this reason and to allow the efficient incorporation of site-effects in the stochastic simulations, only the available geological data were used, providing an initial database for site characterization. Thus, the settlements for which observed macroseismic intensities were available, have been characterized according to their underlying geological formation class (see Figure 1.4) and used as target sites for the simulations. A number of scenarios-models were tested for each event, always proceeding with a trial-and-error method.

Initially, the position of each fault (Sofades and Farsala faults) was constrained following the focal parameters (hypocenter and fault position, fault strike and dip, faulting type, etc.) provided by Papazachos et al. (2001). The dimensions of the faults (length, L, and width, w) were estimated using Eq.3.1 and Eq.3.2, which have been proposed for the estimation of fault dimensions from moment magnitude for continental dip-slip faults (Papazachos et al., 2004, 2006). The dimensions (length, dL and width,

dw) of each subfault were constrained from Eq.3.3, proposed by Beresnev and Atkinson (1999) and were slightly modified in order to scale with the calculated fault dimensions. It should be noted that according to Beresnev and Atkinson (1999), a linear relation has been proposed between the earthquake magnitude and the dimensions of the subfaults.

$$logL = 0.5M - 1.86 \tag{3.1}$$

$$logw = 0.28M - 0.70 \tag{3.2}$$

$$log\Delta l = -2 + 0.4M \tag{3.3}$$

For all simulations, the stress drop parameter was set to 70 bars (Boore and Joyner, 1997). The value 56 bars which has been proposed for normal and strike-slip faults in Greece by Margaris and Boore (1998) and is based in a relatively small number of events for the Aegean area was also tested, but returned very similar results, hence its effect could not be resolved, at least using the available macroseismic information. The crust's average shear wave velocity (beta) and density (rho) were derived from Papazachos et al. (1966). For the rupture propagation velocity, V_{rup}, a typical value of 0.8 was adopted. Larger values (V_{rup}=0.9 and 0.95) were also tested in several cases but, again, returned similar results, with slightly lower synthetic macroseismic values for the southern Thessaly observation sites for the higher V_{rup} value. Different values were used for the high-frequency attenuation parameter kappa, k, according to the geology/soil class of each simulation site, as shown in Table 3.1. For the bedrock sites, a smaller value than previously suggested for rock formations in Greece (Margaris and Boore, 1998) was used, after a trial-and-error approach and taking into account the recent experience for k estimates from bedrock sites in the broader Aegean area.

Table 3.1: High-frequency attenuation parameter kappa, adopted for each geological soil class in the simulations.

Geological group	Type	EC8 class	kappa	Reference
1	Bedrock	A/B	0.015	Adopted after tests
2	Molassic	C	0.044	Klimis et al. (1999)
3	Neogene	C	0.044	Klimis et al. (1999)
4	Quaternary, Plio-Pleistocene	D	0.066	Klimis et al. (1999)

The expected synthetic seismograms were initially simulated without considering the local site-effects (all formations were considered as basement rocks, class 1, without site amplifications). Figure 3.1 presents a typical example of a synthetic seismogram (accelerogram) obtained from the initial simulation of the 1954 Sofades earthquake, for a random site. Following this step, the calculated PGA and PGV values were corrected for site-effects using the constant amplification factors proposed in the GMPE estimated by Skarlatoudis et al. (2003). For this estimation it was assumed that bedrock, Molassic/Neogene, as well as Quaternary/Plio-Pleistocene sediments corresponded to UBC and EC8 soil categories A/B, C and D, respectively, as these are also considered by Skarlatoudis et al. (2003). Moreover, additional simulations were performed, assuming the generic spectral amplification factors shown in Tables 3.2 and 3.3 proposed by Klimis et al. (1999) for Greece for the site classes C and D.

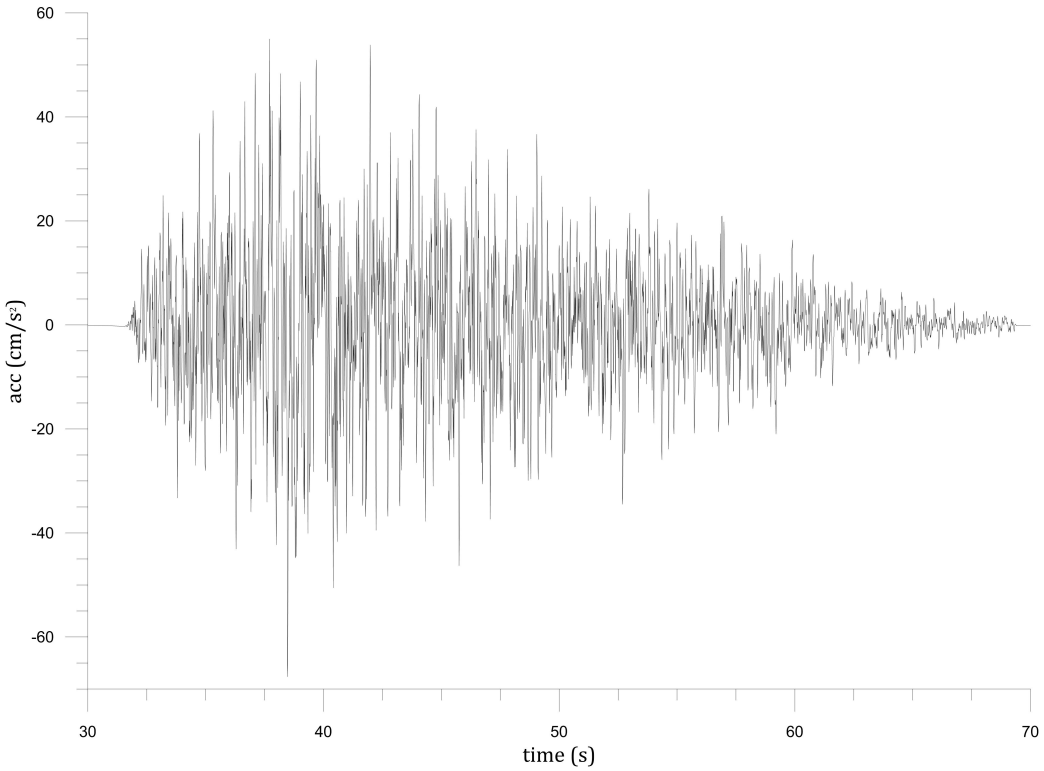

Figure 3.1: Typical synthetic accelerogram from the stochastic simulation of the M=7.0, 1954 Sofades earthquake.

Table 3.2: Spectral amplifications for EC8 soil category C according to Klimis et al. (1999), adopted for Molassic/Neogene sediments sites.

Frequency (Hz)	Amplification factor	Frequency (Hz)	Amplification factor
0.11	1.076	2.67	2.898
0.15	1.107	3.51	3.029
0.31	1.253	5.40	3.243
0.50	1.504	8.01	3.446
0.66	1.763	12.24	3.659
1.78	2.633	24.16	3.990
1.10	2.219	34.04	4.121
2.11	2.751	62.50	4.306

Table 3.3: Spectral amplifications for EC8 soil category D according to Klimis et al. (1999), adopted for Quaternary-Plio/Pleistocene sediments sites.

Frequency (Hz)	Amplification factor	Frequency (Hz)	Amplification factor
0.09	1.125	1.52	3.909
0.10	1.142	1.98	4.113
0.19	1.307	3.09	4.376
0.35	1.742	5.34	4.722
0.46	1.993	7.07	4.918
0.50	2.094	9.39	5.051
1.03	3.347	14.87	5.195
1.15	3.536	40.50	5.461

The final step for the simulation modelling corresponded to the estimation of the expected macroseismic intensities from the synthetic stochastic seismograms. Though this approach is not straightforward, a standard approach was adopted, where the PGA and PGV values from the synthetic waveforms were converted to macroseismic intensities (Modified Mercalli scale, I_{MM}). For this purpose, the proposed relations for the Greek area between PGA/PGV and I_{MM} by Theodulidis and Papazachos (1992), Koliopoulos et al. (1998) and Tselentis and Danciu (2008) were considered. A comparison of the corresponding scaling relations is presented in Figure 3.2. From both plots it is evident that the relations proposed by Tselentis and Danciu (2008) are close to the average of all examined relations, especially for PGA. For this reason, as well as since it was the most recently developed relation, the average I_{MM} values defined using the corresponding conversion relations (Eq.3.4 and Eq.3.5) proposed by Tselentis and Danciu (2008) were adopted for the final I_{MM} assessment from PGA and PGV values of the synthesized time series.

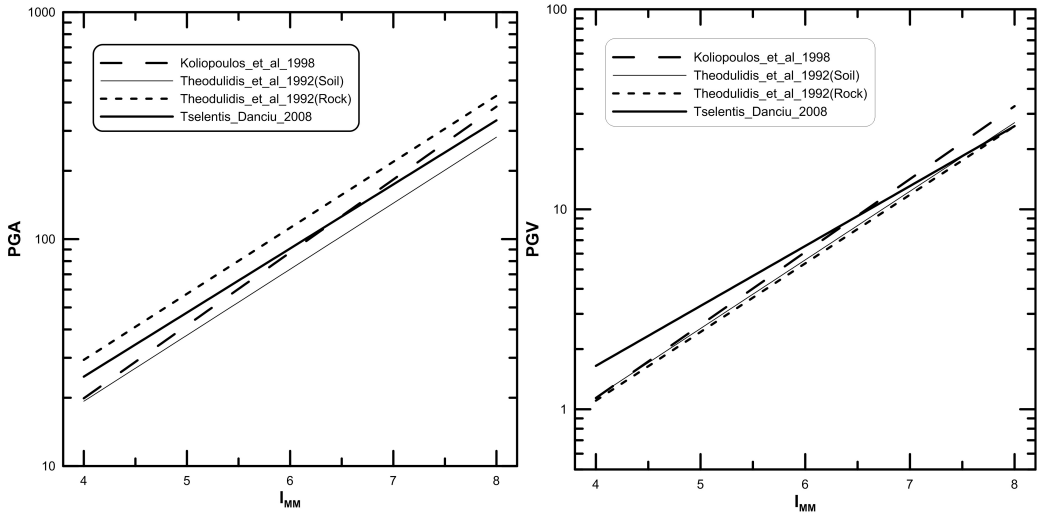

Figure 3.2: Comparison of published scaling relations (Theodulidis and Papazachos, 1992; Koliopoulos et al., 1998; Tselentis and Danciu, 2008) between I_{MM} and PGA (left) and PGV (right) proposed for the Greek area.

$$I_{MM} = -0.946 + 3.563 * logPGA \tag{3.4}$$

$$I_{MM} = 3.3 + 3.358 * logPGV \tag{3.5}$$

3.2 The M=7.0 1954 Sofades earthquake

The collected macroseismic data included observed intensities (I_{MM}), ranging from 5 to 9+, for 75 settlements / simulation target sites (19 on Bedrock, 4 on Molassic type sediments and 52 on Quaternary sediments) throughout the Thessaly area. The observed damages distribution of the 1954 event is also presented in Figure 3.3.

Table 3.4 summarizes all the parameters adopted for the simulations of the 1954 Sofades event seismic motions. The available field observations (Papastamatiou and Mouyaris, 1986; Mountrakis et al., 1993) showed a large number of surface fissures and small fault segments, without revealing a clear surface manifestation of the seismic fault along its length. For this

reason, the depth of the upper edge of the fault was set to 1km, close to the surface. It should be noted that slightly larger depths of 2km and 3km were also tested but no significant differences were observed, though the larger depth (3km) resulted in systematic macroseismic intensity underestimation, suggesting that the adopted choice of 1km was the most appropriate.

Table 3.4: Parameters of the model adopted for all stochastic simulations for the M=7.0, 1954 Sofades earthquake.

Strike	271^o	Subfaults	7x3
Dip	47^o	d_L	6.286km
L	44km	d_w	6km
w	18km	Stress drop	70bars
M_w	7.0	beta	3.4 km/sec
V_{rup}	0.8	kappa	As in Table 3.1

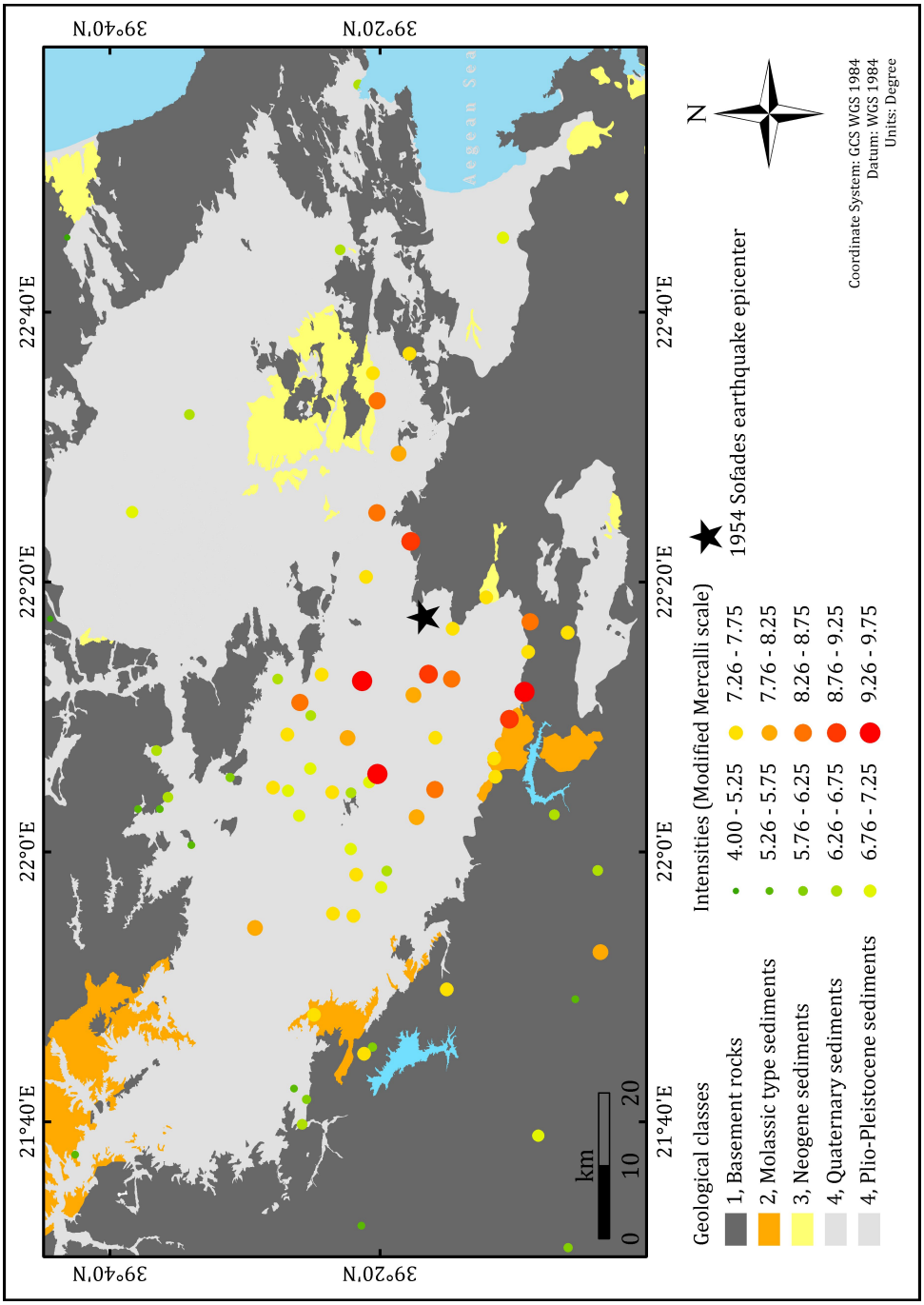

Figure 3.3: Observed macroseismic intensities (Modified Mercalli scale) of the M=7.0, 1954 Sofades earthquake.

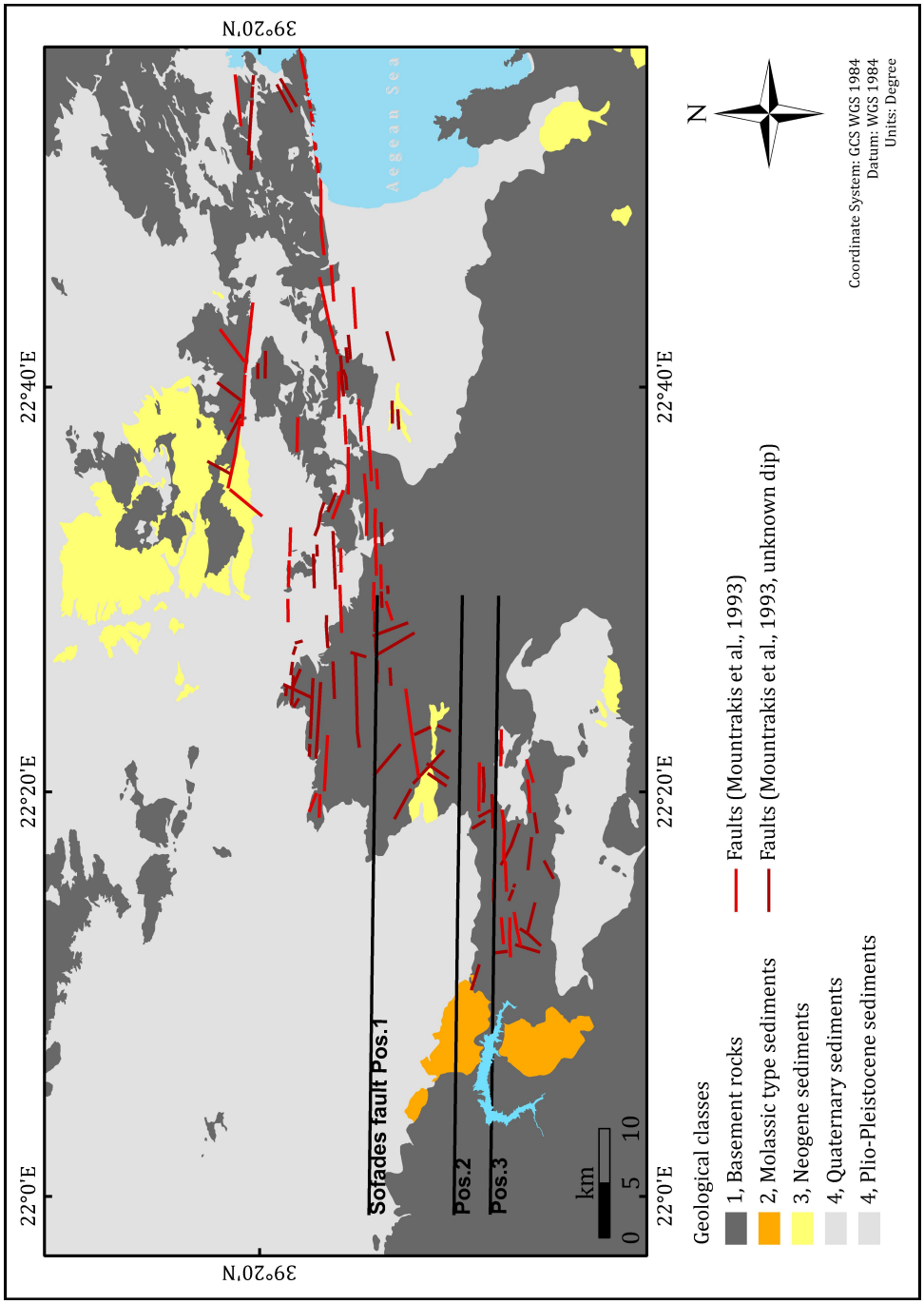

Figure 3.4: The three candidate positions for the upper Sofades fault edge considered in the present study for the 1954 event. The main active fault surface traces in southern Thessaly, as proposed by Mountrakis et al. (1993), are also depicted.

For the initial simulation, the Sofades fault position proposed by Papazachos et al. (2001) was adopted (depicted as Pos.1 in Figure 3.4). The results from this initial simulation, presented in Figure 3.5, showed significant deviations between observed and synthetic intensities. These differences are observed both without site amplifications, as well as when using the constant site amplification factors proposed by Skarlatoudis et al. (2003) and the generic spectral amplifications suggested by Klimis et al. (1999). In general, the results show that the modeled intensities for bedrock sites (blue diamonds in Figure 3.5) are lower than the observed intensities. The opposite is observed for soil sites, with synthetic macroseismic intensities (no site-effect amplification considered, Figure 3.5a) showing much larger values than the observed values, contrary to what would be expected for these sites, which are expected to exhibit significant site amplifications. Due to this discrepancy, the bias between synthetic and observed macroseismic intensities becomes worse when using site-effect amplifications (Figure 3.5b and Figure 3.5c).

In order to explain this discrepancy, it is clear that any simulation scenario would require a reduction of the synthetic macroseismic intensities for the soft soil (essentially Quaternary/Plio-Pleistocene) sites, and an opposite increase for bedrock sites. This pattern can be partly fulfilled if the fault's upper edge would be located southern than the initial position examined, being in better agreement with the mapped active faults of the southern Thessaly fault zone (Mountrakis et al., 1993), as these are presented in Figure 3.4. For this reason, two additional possible fault positions were considered, depicted as Pos.2 and Pos.3 in Figure 3.4. As Figure 3.6 indicates, simulations using the second fault position (Pos.2) also resulted in significant deviations between observed and synthetic macroseismic intensities.

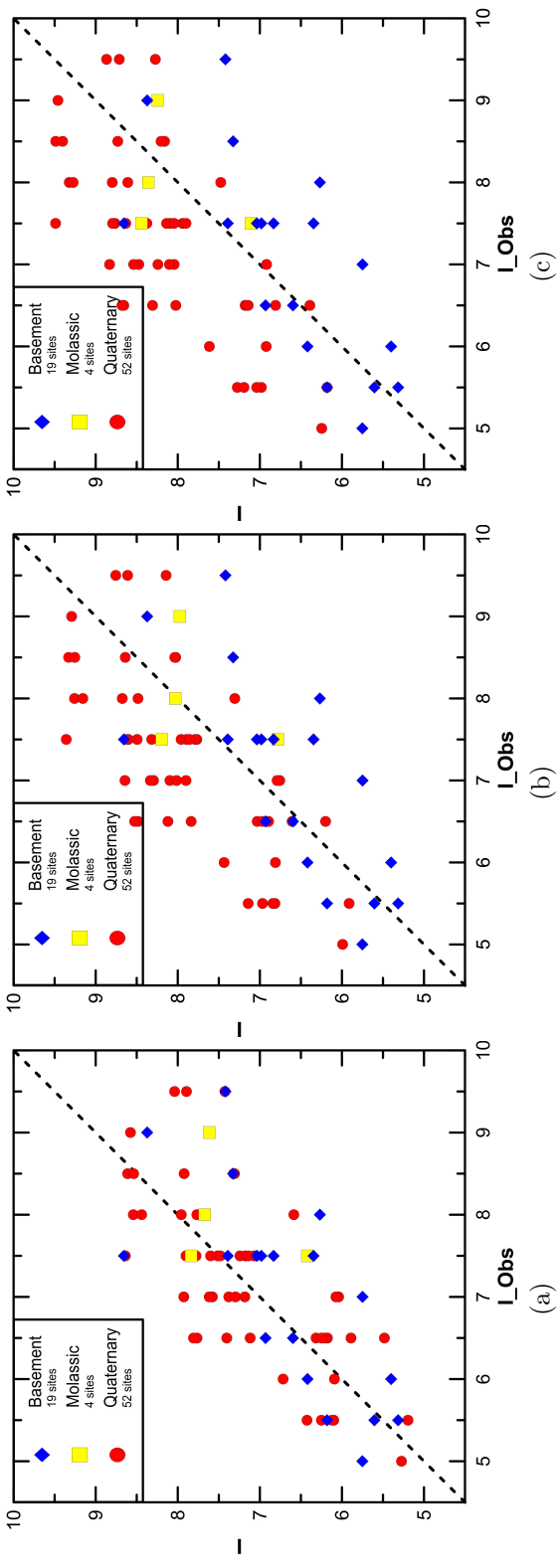

Figure 3.5: Comparison of modeled, I, against observed, I_Obs, macroseismic intensities for Sofades fault position 1 scenario (see Figure 3.4). (a) No site-effects. (b) Using the constant amplification factors of Skarlatoudis et al. (2003). (c) Using the generic spectral amplifications proposed by Klimis et al. (1999).

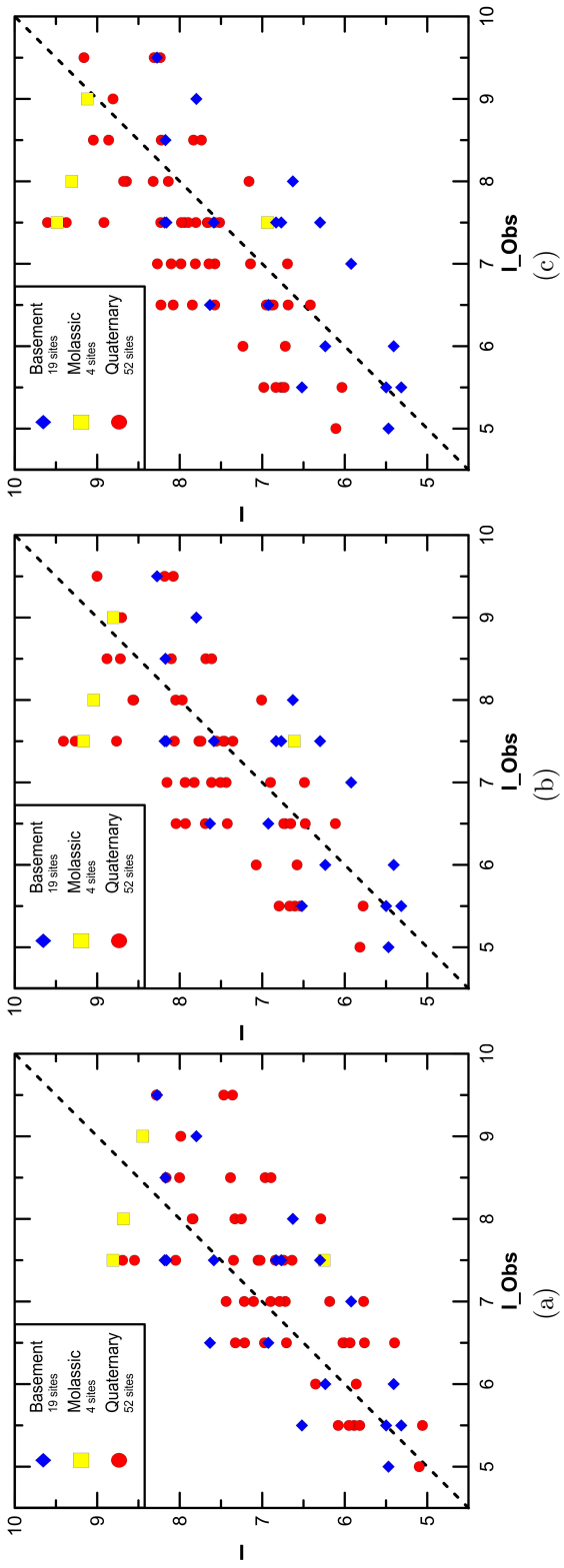

Figure 3.6: Same as Figure 3.5, for the second fault position simulation (Pos.2 in Figure 3.4).

The third fault position examined (Pos.3 in Figure 3.4), which was constrained by the observed surface ruptures and neotectonic faulting of the southern Thessaly basin (Papastamatiou and Mouyaris, 1986; Caputo and Pavlides, 1993; Mountrakis et al., 1993, also shown in Figure 3.4) led to the best results, as is presented in Figure 3.7. As can be seen from Figure 3.7a, the synthetic and macroseismic intensities show an improved correlation when no site amplifications are considered. The observed agreement for bedrock sites suggests that the fault position is optimally placed, in agreement with the available neotectonic information. However, the soil sites (mostly Quaternary/Plio-Pleistocene sites, class D) show significantly higher observed intensities, when no site amplifications are considered for the stochastic simulation results. This observation confirms the presence of significant site amplification effects for class D formations, as expected.

It should be noticed that performing simulations using the amplification factors proposed by Klimis et al. (1999), in an attempt to account for this pattern, has led to a systematic overestimation of macroseismic intensities for these mainly Quaternary formation sites (Figure 3.7c), especially for the central Thessaly basin part. The HVSR measurements performed in the southern Thessaly basin showed that the recovered resonance frequencies for the central section of the basin (Karditsa area) exhibit a very low resonant frequency ($\sim$0.35-0.4Hz, as shown in Figure 2.14 and discussed in Chapter 2), most probably due to the significant thickness of the Quaternary deposits. This low frequency amplification is very different than the corresponding typical (generic) amplification factors proposed by Klimis et al. (1999) for EC8 class D formations (see Figure 4.1 and later discussion in Chapter 4), which can be considered as the main reason for the observed discrepancy and macroseismic intensity overestimation. The optimal results have been obtained for fault position 3 (Pos.3 in Figure 3.4), using the constant amplification factors for PGA and PGV proposed by Skarlatoudis et al. (2003) for the broader Aegean area. Macroseismic intensities for both bedrock and Quaternary formation sites show a very good correlation between predicted and observed intensities (Figure 3.7b).

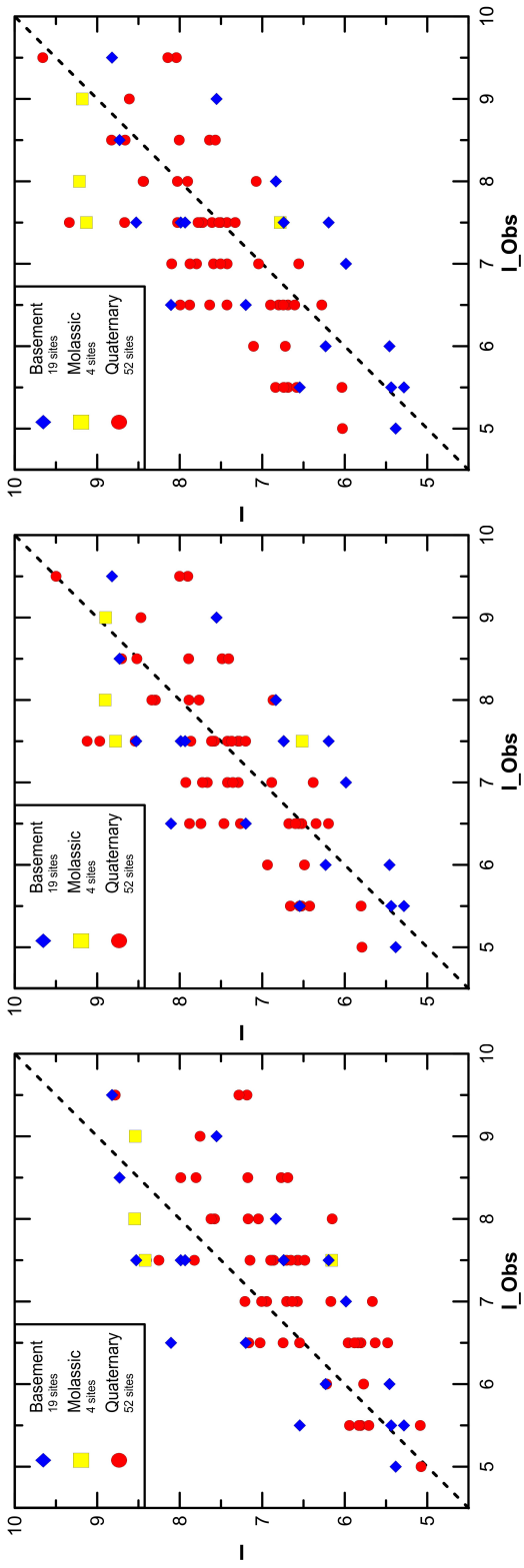

Figure 3.7: Same as Figure 3.5, for the third fault position simulation (Pos.3 in Figure 3.4).

In order to assess the effect of the performed modeling for the broader Thessaly area, the final modeling parameters (Table 3.4, Pos.3, constant amplification factors for soil formations, etc.) were adopted in order to perform computations for a grid of target points with a 4km spacing. This procedure was used to estimate the expected damage distribution of the 1954 event, in terms of macroseismic intensities, throughout the whole broader Thessaly area. The final damage distribution maps for bedrock (no site amplification) and using the appropriate site amplification factors by Skarlatoudis et al. (2003), are presented in Figure 3.8. The results confirm the effect of the fault geometry, as well as local geology on the expected (and observed) seismic motions, with significant modifications of the observed damage pattern due to the presence of local site-effects. More specifically, the hanging wall fault area is exhibiting higher seismic motion levels, which are further enhanced for the largest part of the south-western Quaternary Thessaly basin due to the site-effect contribution.

The synthetic macroseismic intensities maps for all three (3) considered Sofades fault positions and with the use of Skarlatoudis et al. (2003) constant amplification factors can be found in Appendix Figures A.7, A.8 and A.9.

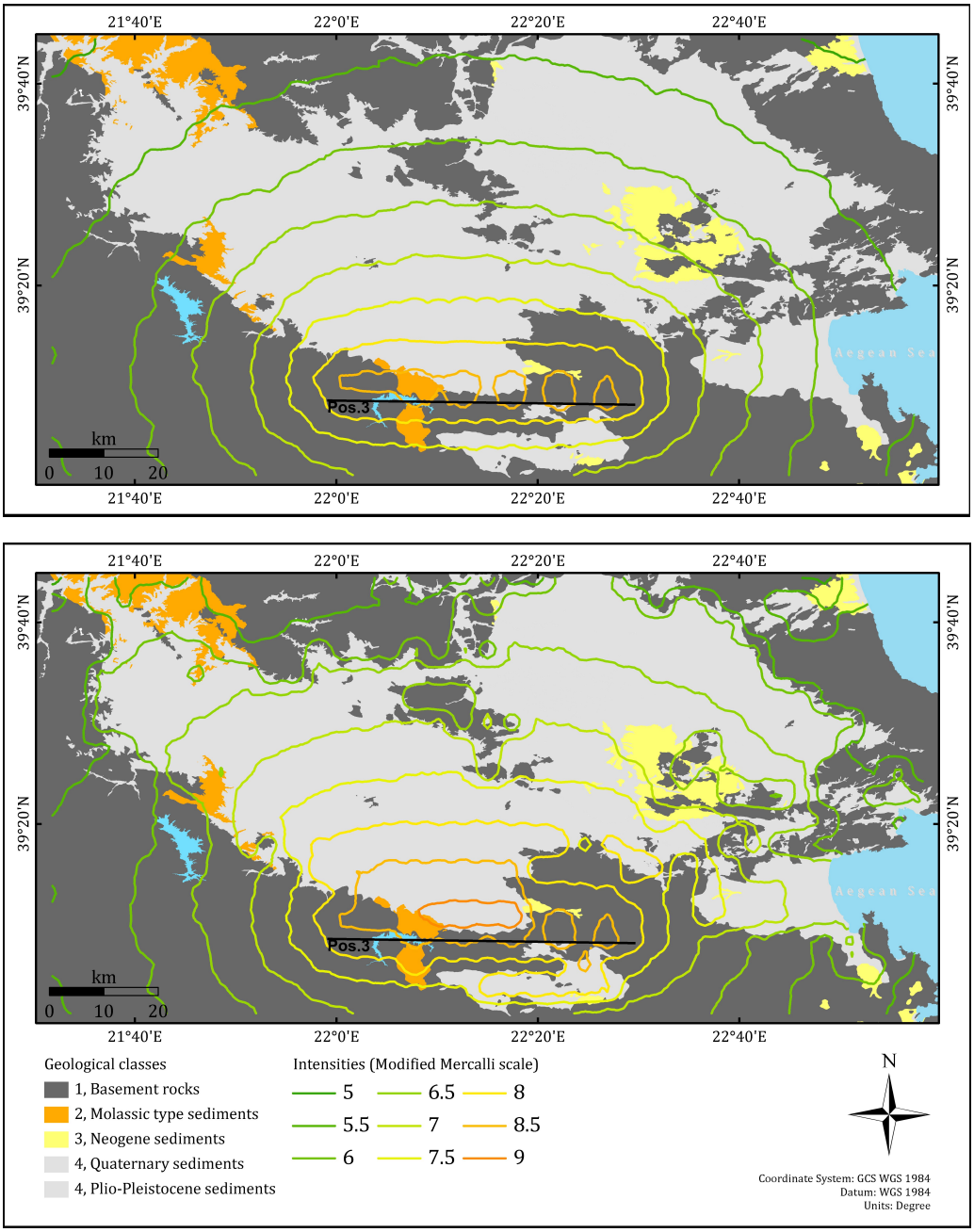

Figure 3.8: Estimated macroseismic intensities contours (synthetic isoseismals) for the M=7.0, 1954 Sofades event, considering the optimal fault position 3 (see Figure 3.4), without the use of site amplifications (upper figure) and with the use of the constant PGA / PGV site amplification factors of Skarlatoudis et al. (2003) (lower figure).

3.3 The M=6.8 1957 Velestino earthquake

The collected macroseismic data included observed intensities (I_{MM}), ranging from 5+ to 9+, for 79 settlements (simulation target sites) throughout the Thessaly area (32 Bedrock sites, 3 Neogene sediments sites and 44 Quaternary sediments sites). The observed damages distribution of the 1957 event is also presented in Figure 3.9. Table 3.5 summarizes all the parameters adopted for the simulations of the 1957 Velestino event seismic motions. In this case, the depth of the upper edge of the fault was also set to 1km, relatively close to the surface. Again, slightly larger depths of 2km and 3km were also tested for the upper fault edge but no significant differences were observed.

Table 3.5: Parameters of the model adopted for all stochastic simulations for the strong motion of the M=6.8, 1957 Velestino earthquake.

Strike	269^o	Subfaults	7x3
Dip	47^o	d_L	5km
L	35km	d_w	5.33km
w	16km	Stress drop	70bars
M_w	6.8	beta	3.4 km/sec
V_{rup}	0.8	kappa	As in Table 3.1

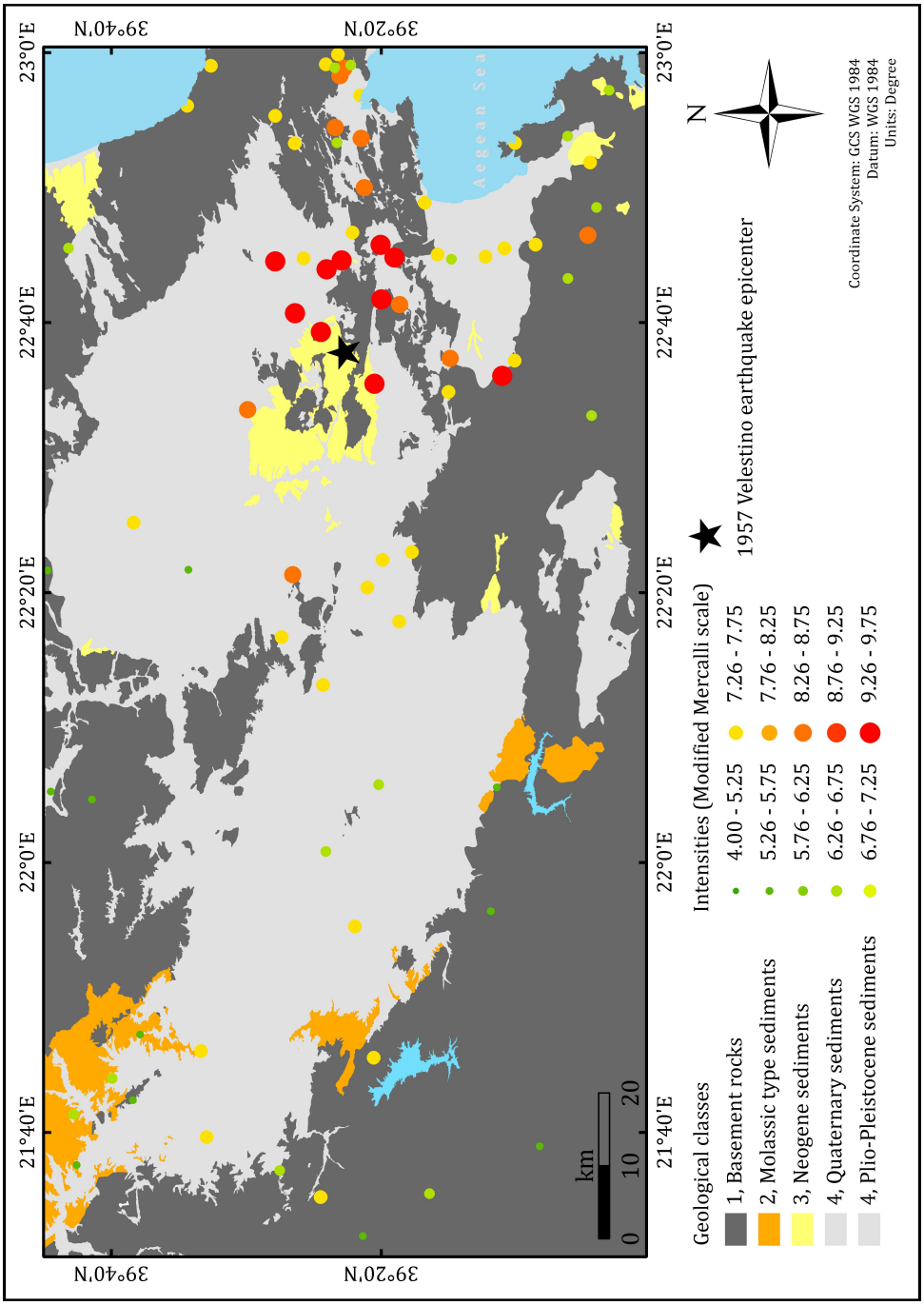

Figure 3.9: Observed macroseismic intensities (Modified Mercalli scale) of the M=6.8, 1957 Velestino earthquake.

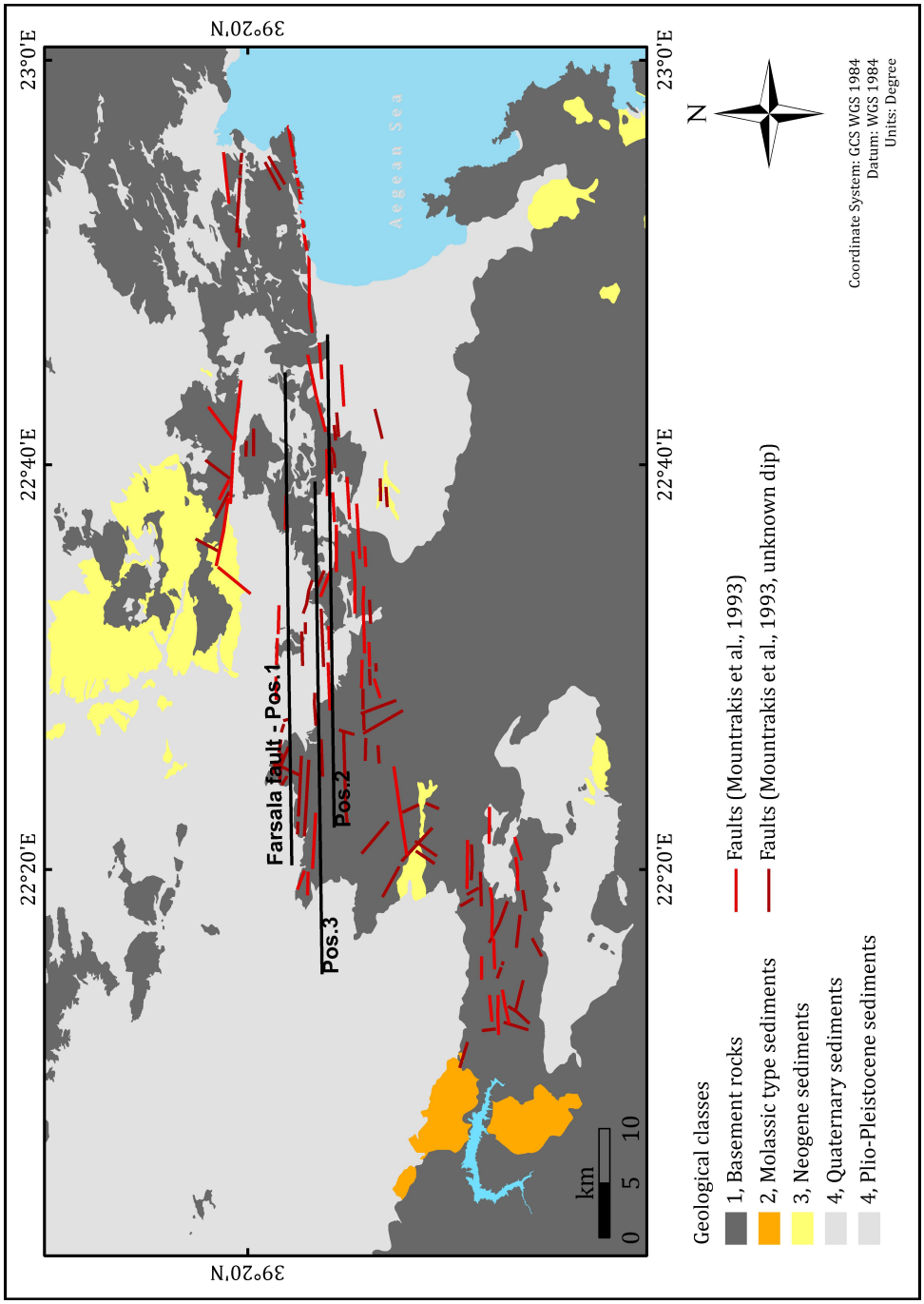

Figure 3.10: The three candidate positions for the upper Farsala fault edge considered in the present study for the 1957 event. The main active fault surface traces in southern Thessaly, as proposed by Mountrakis et al. (1993), are also depicted.

As in the Sofades case, the position adopted initially for the Farsala fault was the one proposed by Papazachos et al. (2001) (depicted as Pos.1 in Figure 3.10). Again, the results showed significant deviations between observed and synthetic intensities (Figure 3.11). Regarding bedrock sites (blue diamonds in Figure 3.11), the modeled intensities are generally lower than the observed ones, while a number of extreme discrepancies are observed (differences larger than 3 in the Modified Mercalli scale). Lower synthetic macroseismic intensities are also observed for soil sites (without employing site-amplifications, Figure 3.11a), with the bias between synthetic and observed macroseismic intensities slightly improving when using the Skarlatoudis et al. (2003) constant amplification factors (Figure 3.11b). The employment of Klimis et al. (1999) generic spectral amplifications (Figure 3.11c), probably overestimates the synthetic macroseismic intensities due to the same reasons analyzed in the previous section, resulting in larger values larger than the observed ones.

In order to increase the synthetic macroseismic intensities for both bedrock and soil sites, two additional possible positions were tested for the upper edge of the Farsala fault (Pos.2 and Pos.3 of Figure 3.10). The results are shown in Figures 3.12 and 3.13. As can be seen from both figures, the discrepancies could not be resolved by a simple repositioning of the upper edge of the fault. The biggest discrepancies are observed for several bedrock sites, showing that the simulation can not realistically reproduce the seismic wavefield and corresponding damages, when considering sites where site amplification is not normally expected.

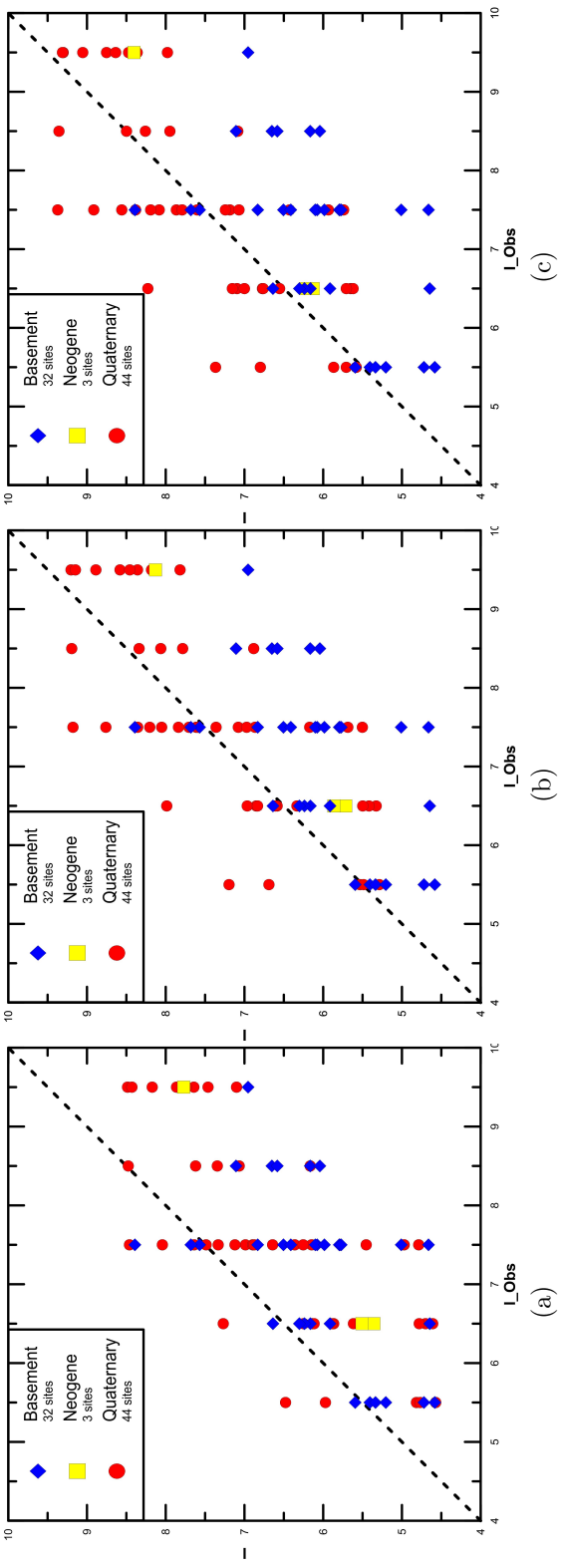

Figure 3.11: Comparison of modeled, I, against observed, I_Obs, macroseismic intensities for Farsala fault position 1 scenario (see Figure 3.10). (a) No site-effects. (b) Using the constant amplification factors of Skarlatoudis et al. (2003). (c) Using the generic spectral amplifications proposed by Klimis et al. (1999).

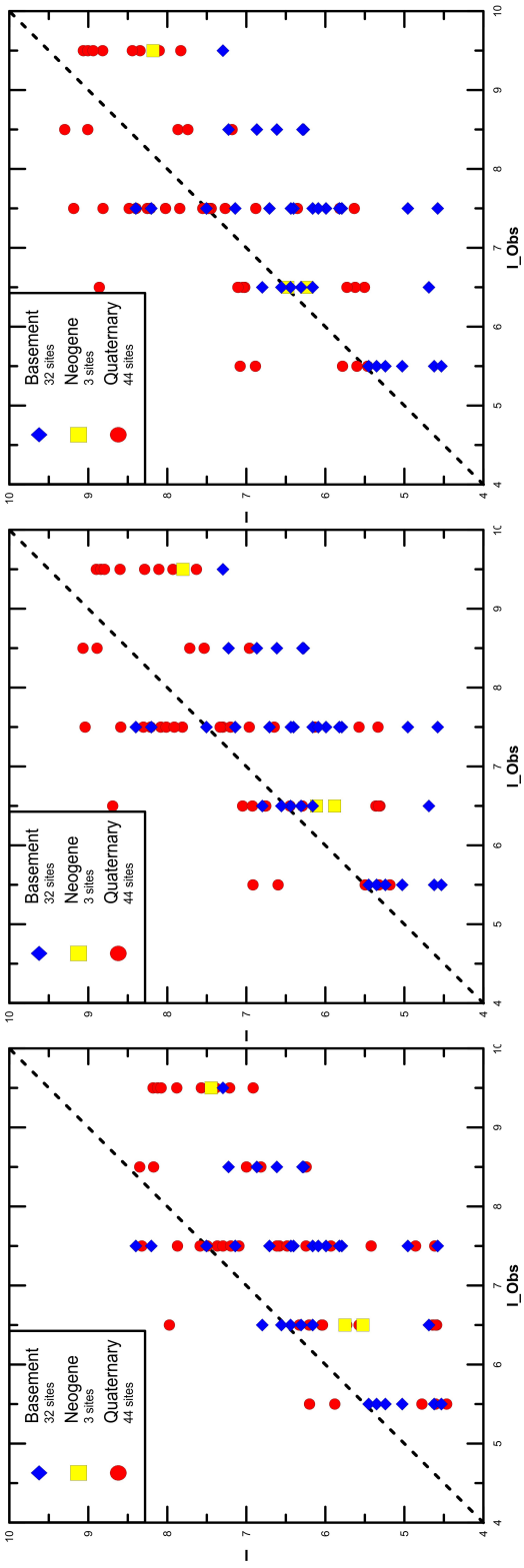

Figure 3.12: Same as Figure 3.11, for the second fault position simulation (Pos.2 in Figure 3.10).

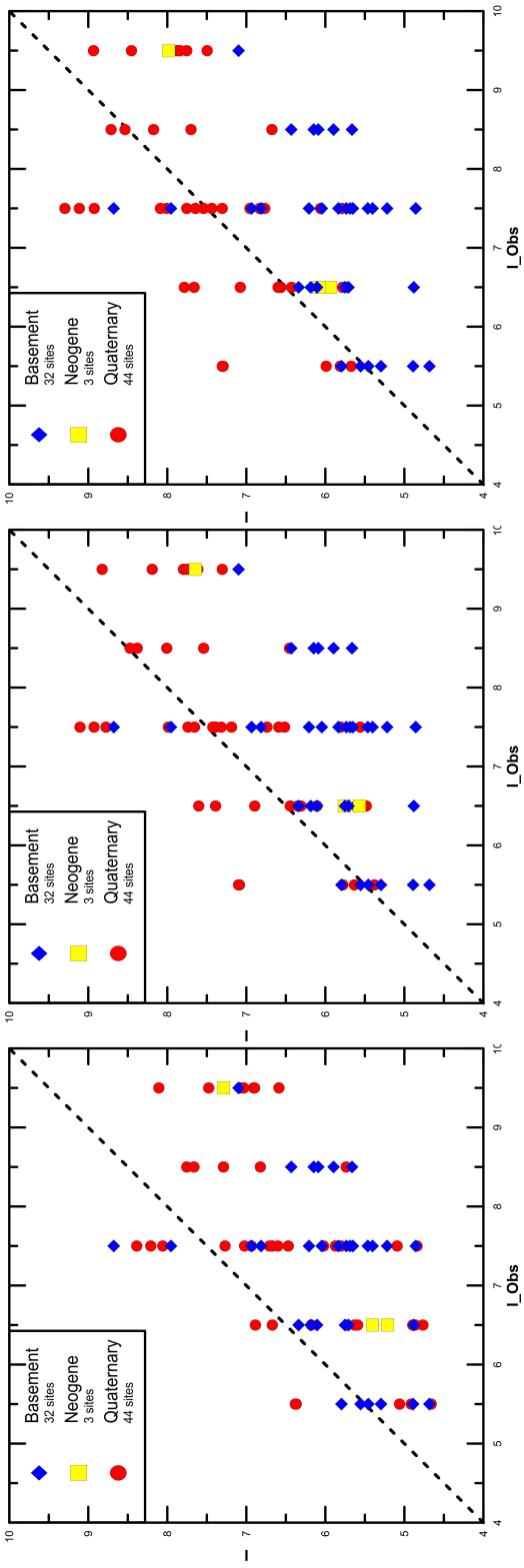

Figure 3.13: Same as Figure 3.11, for the third fault position simulation (Pos.3 in Figure 3.10).

Although all three examined candidate Farsala fault positions are in general agreement with the mapped active fault traces of the area (as is indicated by Figure 3.10), all simulations using these positions resulted in overestimation of macroseismic intensities for the broader Farsala region (central Thessaly), while underestimating the macroseismic intensities for the eastern Thessaly basin (Velestino-Volos region). As this pattern suggested, in order to improve the agreement of observed and synthetic macroseismic intensities specifically for these areas, directional rupture scenarios were tested, were the rupture was assumed to start closer to the western edge of the fault (near Farsala), propagating in a W-E direction and with a larger rupture propagation velocity (rupture values of 0.9 and 0.95 were tested, instead of the typical value of 0.8). Figure 3.14 shows the results of a directional rupture scenario for Pos.1 (see Figure 3.10) with a rupture propagation speed of 0.95, where it is clear that there is no significant improvement regarding estimated macroseismic intensities for bedrock sites, while the increase of the rupture propagation speed does not have a significant effect on the synthetic values. Also, with these modifications, a slight but not important improvement was observed for the Farsala and Velestino-Volos areas.

The comparison of the directional scenarios results among all three positions shows that soil sites synthetic intensities, amplified by Skarlatoudis et al. (2003) amplification factors (Figure 3.14b), correlate better with the observed intensities when using Pos.1 (Figure 3.15). This fact, along with the need to increase the synthetic intensities for bedrock sites, led to considering a scenario using Pos.1, with a slightly larger length for the Farsala fault, thus, a slightly larger moment magnitude.

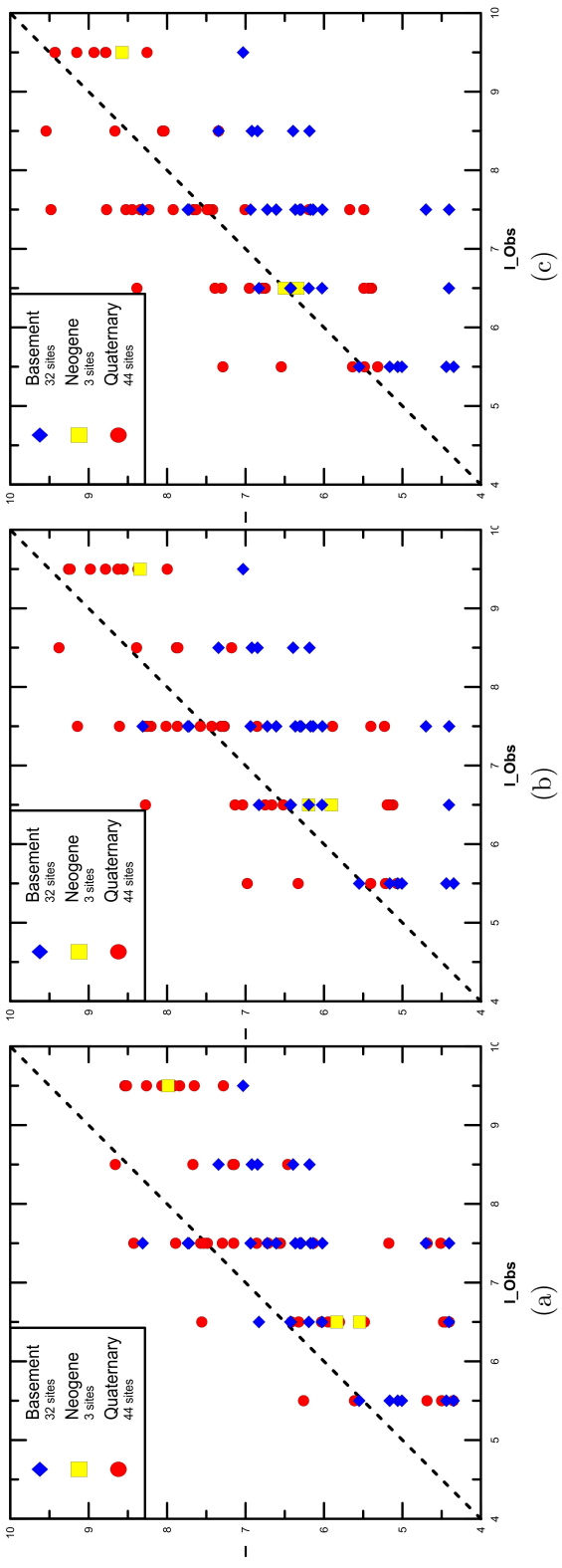

Figure 3.14: Same as Figure 3.11, for the first fault position simulation (Pos.1 in Figure 3.10), with a directional rupture and a rupture propagation velocity of 0.95.

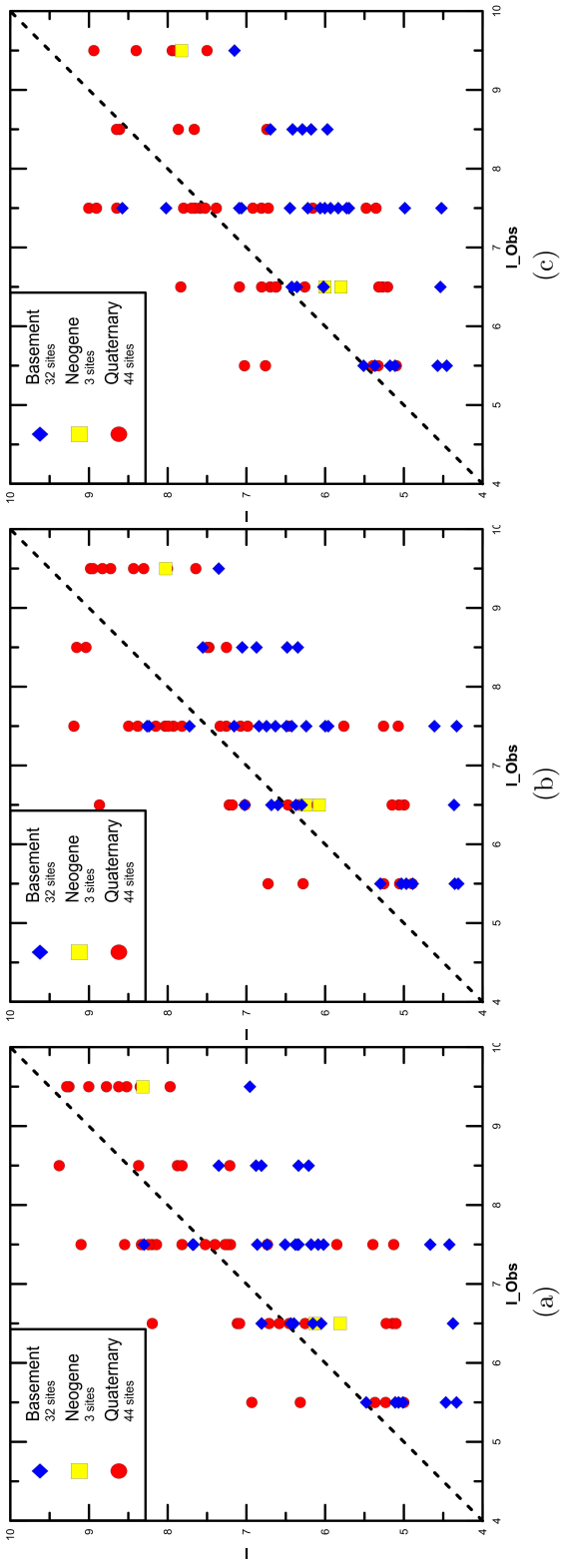

Figure 3.15: Comparison of modeled macroseismic intensities with Skarlatoudis et al. (2003) amplification factors, I, against observed macroseismic intensities, I_Obs, for: (a) Pos.1, (b) Pos.2 and (c) Pos.3 (see Figure 3.10).

The fault length for the new scenario (considering Pos.1) was set to L=40km (5km larger than the initial length of 35km), which corresponds to a moment magnitude of roughly M=6.9. All the other model parameters are the same as in Table 3.5. It is clear from the results of this simulation (shown in Figure 3.16) that synthetic macroseismic intensities of bedrock sites and soil sites (with Skarlatoudis et al., 2003 amplification factors) are generally improved, showing a better agreement with the observed ones.

Even with this scenario, the aforementioned localized large discrepancies for seven (7) specific sites could not be resolved. All the simulations returned synthetic macroseismic intensities much lower than the observed ones for these sites. The spatial distribution for these sites is presented separately in Figure 3.17, where the symbol size represents the difference between the observed intensity for the site and the synthetic intensity as defined from the final simulation scenario. Though the chance of exaggerated reports for the original observations must be taken into account, it can be observed from the original IGME maps (see Figure A.1) that four (4) of these sites-settlements (Mesenikolas, Argireika, Kokkotoi, and Vatsounia) are located upon flysch formations (classified as bedrock, class 1). Flysch formations can be differentiated regarding their expected dynamic amplification behavior, as well as their geotechnical properties and the stratigraphy of the involved formations. More specifically, if the flysch formation is weathered or has a high soft formation content (e.g. mixtures of loose sands-clays, etc.), its geotechnical properties are relatively poor, especially with the presence of water. This fact, along with the possible rugged topography (large slopes, etc.) can lead to large local site amplifications, therefore larger macroseismic intensities. In other words, it is possible that for these cases, the flysch formations locally behave as more loose formations, susceptible to amplification, formations. The behavior of these specific formations could not be studied in detail since it would require the availability of in-situ tests.

Regarding Anthotopos (see Figure 3.17) which is classified as a bedrock site (class 1), it is observed from the IGME maps, as well as from satellite data (Google Earth) that this village is build on the contact between both

Quaternary sediments (eastern part of the village) and Basement rocks (western part). This essentially explains the difference between the high observed and the low modeled macroseismic intensities, since the more appropriate site amplifications (Skarlatoudis et al., 2003 for EC8 soil class D) were not considered for this site.

Finally, it is observed that all simulations resulted in an underestimation of synthetic macroseismic intensities for a number of sites located at the northern part of the western Thessaly basin. Trikala and Valtino exhibit the most significant underestimation. This amplification along the westernmost Thessaly basin occurs for sites which are approximately at a distance of 40-65km from the fault. This suggests that the observed increased intensities may be due to specific phenomena, such as Moho critical reflections or directive rupture energy reflected from the Moho or other inter-crustal discontinuities, toward this section of the Thessaly basin. Such specific source-rupture or reflected energy phenomena can not be simulated using the available information or the adopted simulation modeling, suggesting that the proposed methodology can not fully replace detailed wave-propagation models.

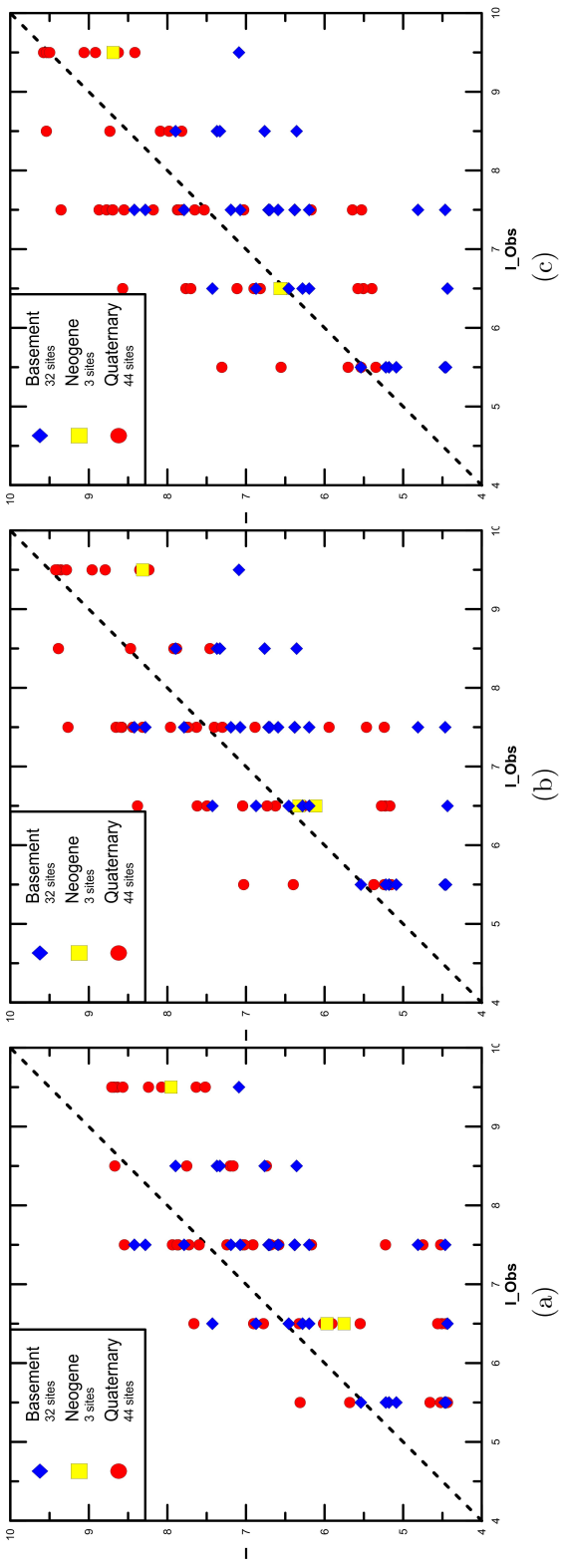

Figure 3.16: Same as Figure 3.11, for the first fault position simulation (Pos.1 in Figure 3.10), with a directional rupture and a larger fault length.

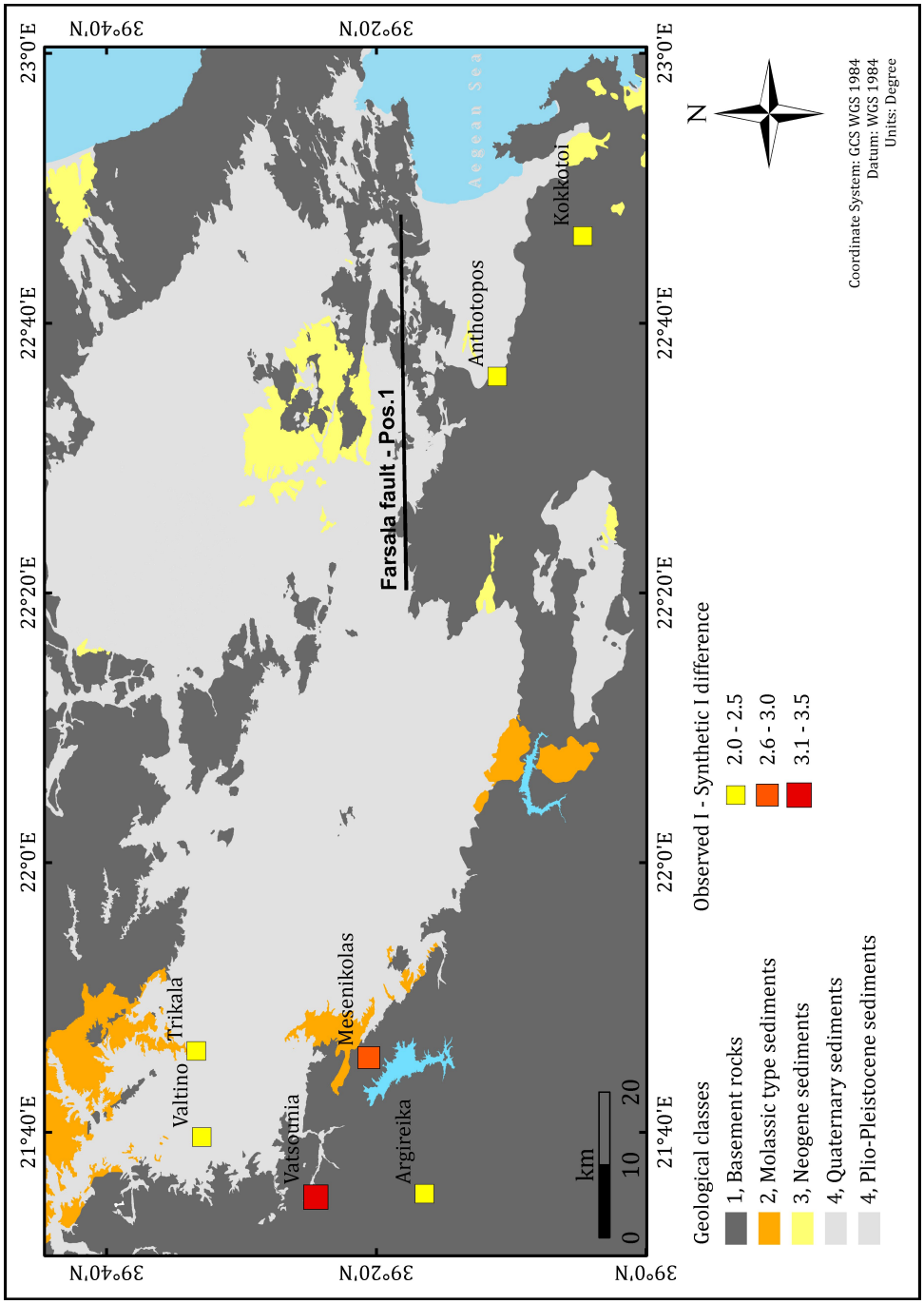

Figure 3.17: Sites with large differences between observed and synthetic macroseismic intensities, as emerged from the final simulation scenario (Pos.1, larger fault length, see Figure 3.16).

The final modeling parameters (Table 3.5, Pos.1 - larger length, constant amplification factors by Skarlatoudis et al., 2003, etc.) were used to perform computations for the same 4km spacing grid as in the 1954 Sofades case. The final synthetic isoseismals for bedrock (no site amplification) and using the appropriate site amplification factors by Skarlatoudis et al. (2003), are presented in Figure 3.18. Again in this case, the effect of fault geometry and the significant contribution of site-effects to seismic damage distribution, are both confirmed. The hanging wall fault area is exhibiting higher seismic motion levels and especially its eastern section, due to the directional rupture propagation defined in the simulation model.

The synthetic macroseismic intensities maps for the three (3) considered Farsala fault positions and for position 1 with a larger fault length, with directional rupture and considering Skarlatoudis et al. (2003) constant amplification factors can be found in Appendix Figures A.10, A.11, A.12 and A.13.

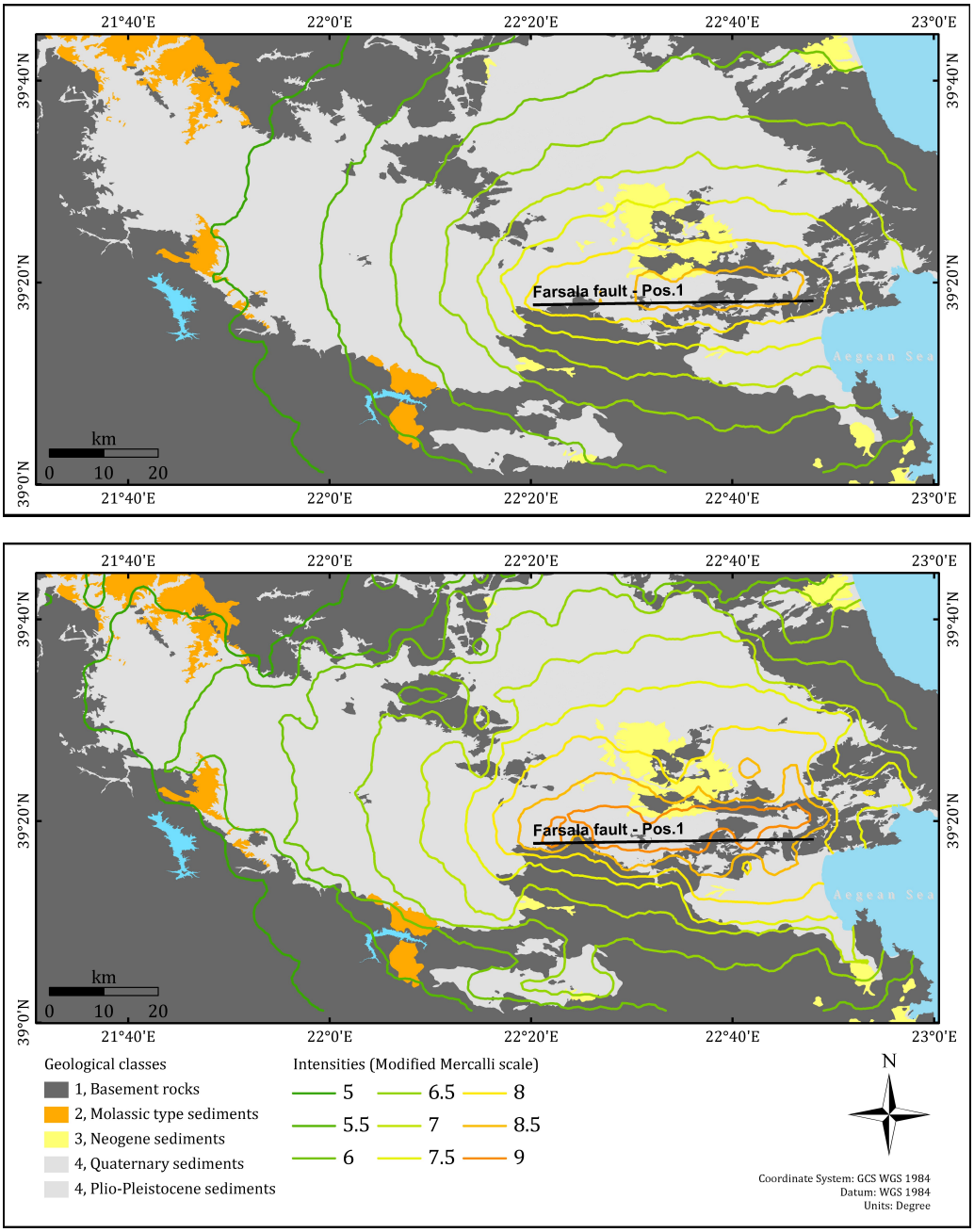

Figure 3.18: Estimated macroseismic intensities contours (synthetic isoseismals) for the M=6.8, 1957 Velestino event, considering the optimal fault position 1 (see Figure 3.10) with an increased length of 40km, without the use of site amplifications (upper figure) and with the use of the constant PGA / PGV site amplification factors of Skarlatoudis et al. (2003) (lower figure).

4.Conclusions

The main conclusion that can be extracted from the results of the present work, is that the adopted stochastic methodology provides reliable results, since the stochastic simulation predictions and the observed macroseismic intensities are generally in very good agreement for the examined Southern Thessaly events. This suggests that all the considered assumptions (e.g. scaling relations), as well as the stochastic simulation methodology itself, can lead to reliable scenarios of past and future earthquakes.

The macroseismic data of historical earthquakes provide important information on the seismic rupture and the seismic waves propagation. Thus, regarding the 1954, Sofades event, the available macroseismic data indicated the absence of directionality for the rupture propagation, while the fault was probably positioned to the south with respect to its originally proposed position. On the contrary, regarding the 1957, Farsala event, the macroseismic data indicated the presence of intense directional rupture phenomena (West-to-East rupture propagation), while the moment magnitude of the earthquake is suggested to be slightly larger (M$\sim$6.9) than the originally proposed one (M=6.8).

The site-effect assessment for the study area returned less realistic results when using the generic transfer functions of Klimis et al. (1999), in comparison to the employment of constant amplification factors for PGA and PGV values (Skarlatoudis et al., 2003). The main reason for this overestimation can be observed in the low-frequency territory of Figure 4.1 ($\sim$0.35-0.4Hz), where it is obvious that the amplifications proposed by Klimis et al. (1999) for EC8 class D formations are significantly lower than the actual ones, as obtained from the HVSR measurements for most south-

ern Thessaly sites that exhibit large sedimentary cover thicknesses. On the contrary, the use of the Skarlatoudis et al. (2003) constant amplification factors leads to a more reliable estimation of the amplifications due to local site effects. The presence of significant site amplification effects for class D formations can be observed when comparing Figures 4.2 and 4.4 to Figures 4.3 and 4.5, respectively, where it is clear that the employment of Skarlatoudis et al. (2003) constant amplification factors, differentiates significantly the synthetic macroseismic intensities for the 1954 M=7.0 and 1957 M=6.8 events.

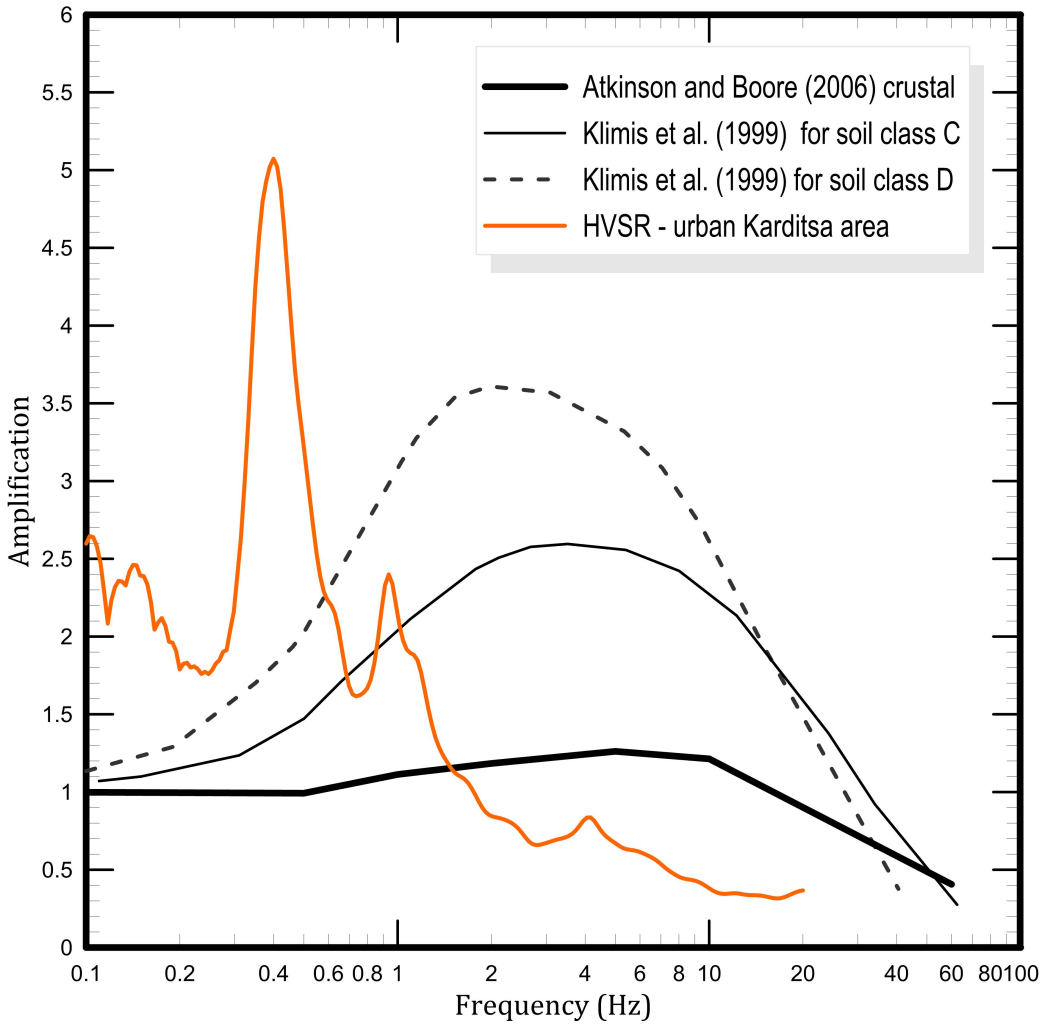

Figure 4.1: Comparison of the Atkinson and Boore (2006) crustal amplifications adopted for bedrock formations, the Klimis et al. (1999) amplifications for soil classes C and D (see Tables 3.3 and 3.2) and the HVSR variation with frequency for position 4 (urban Karditsa area, see Figures 2.1 and 2.14).

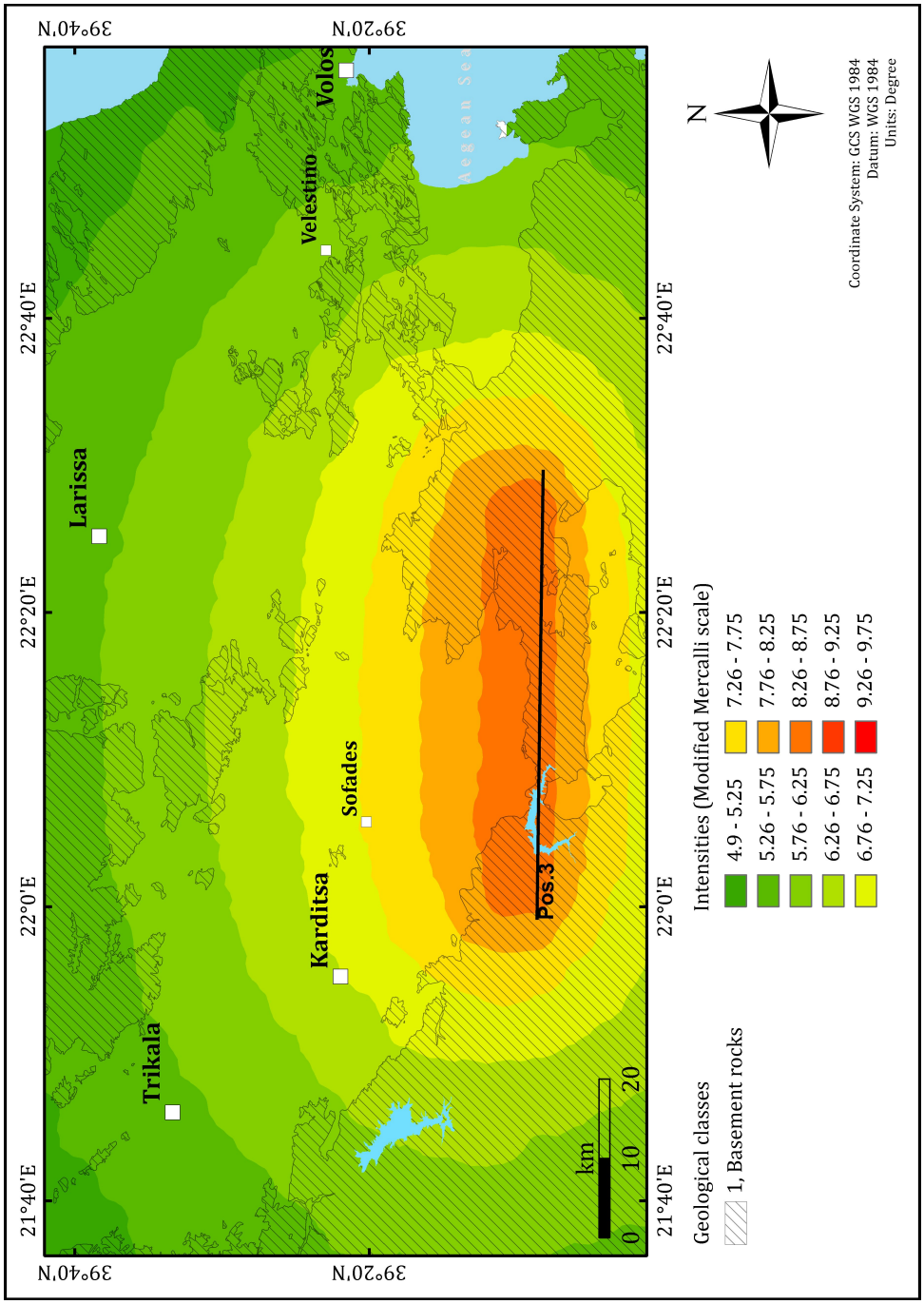

Figure 4.2: Estimated macroseismic intensities distribution for the M=7.0, 1954 Sofades event, considering the optimal fault position 3 (see Figure 3.4), without site amplifications.

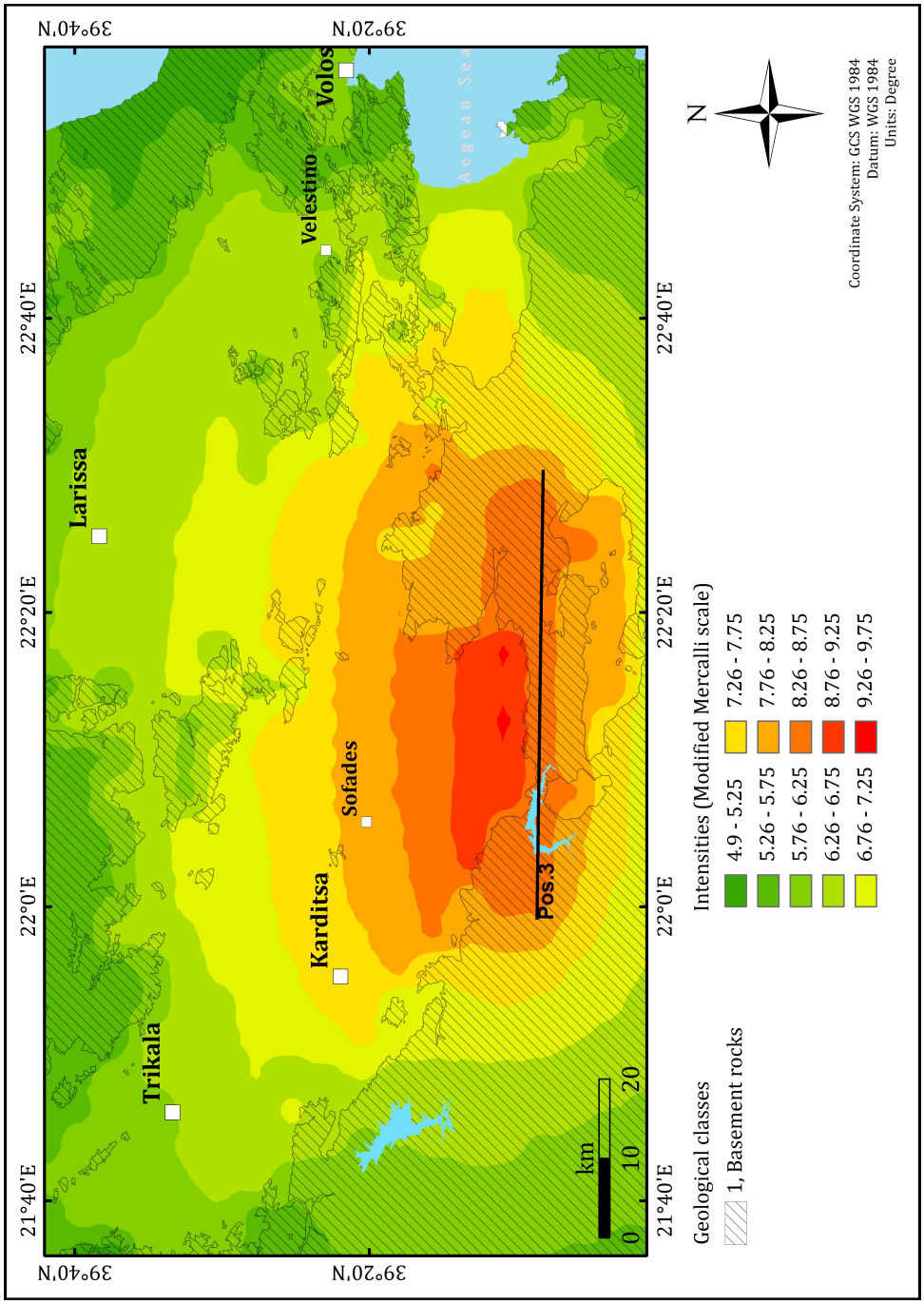

Figure 4.3: Same as Figure 4.2 considering the constant PGA / PGV site amplification factors of Skarlatoudis et al. (2003).

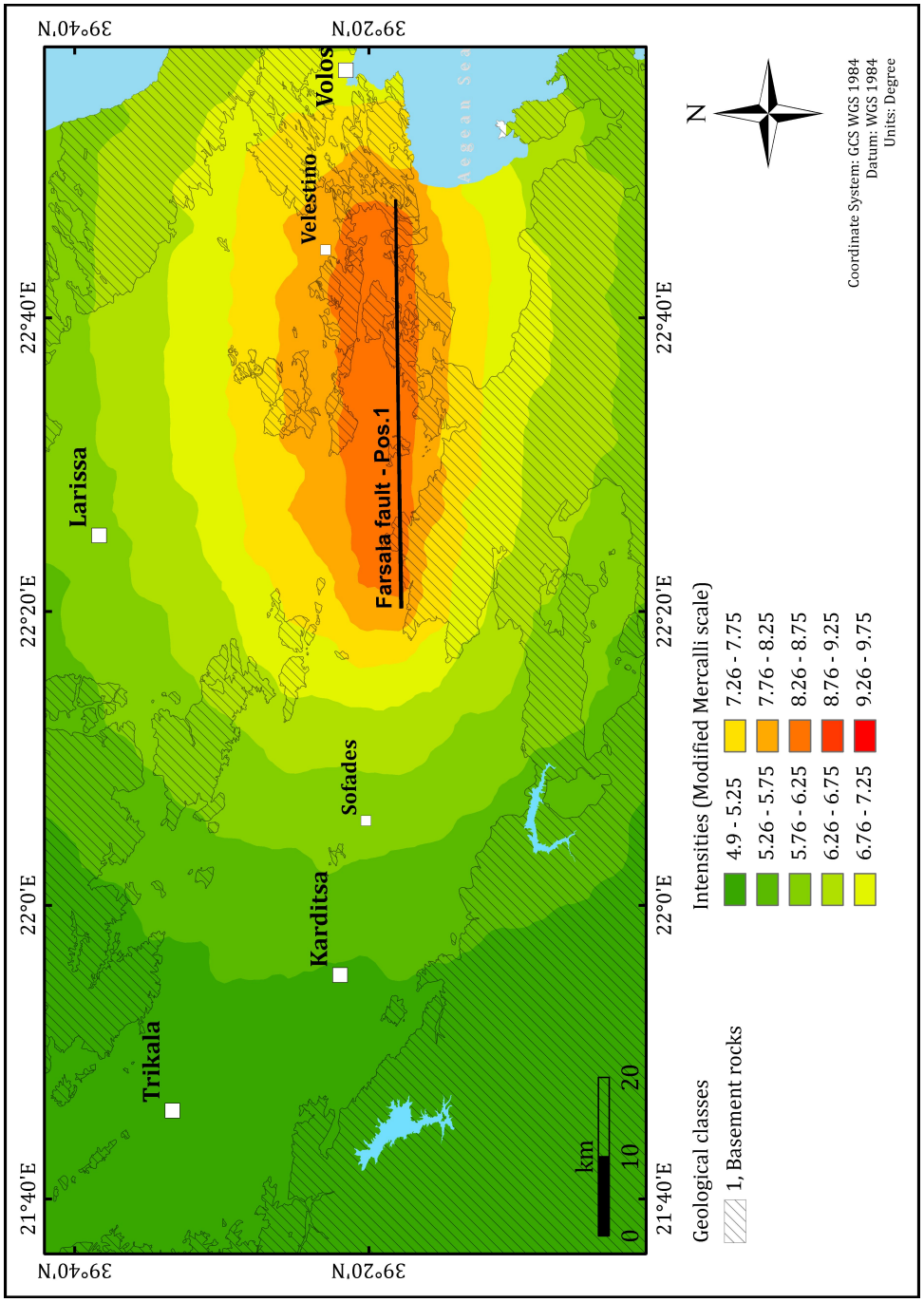

Figure 4.4: Estimated macroseismic intensities distribution for the M=6.8, 1957 Velestino event, considering the optimal fault position 1 (see Figure 3.4) with a larger fault length of 40km, without site amplifications.

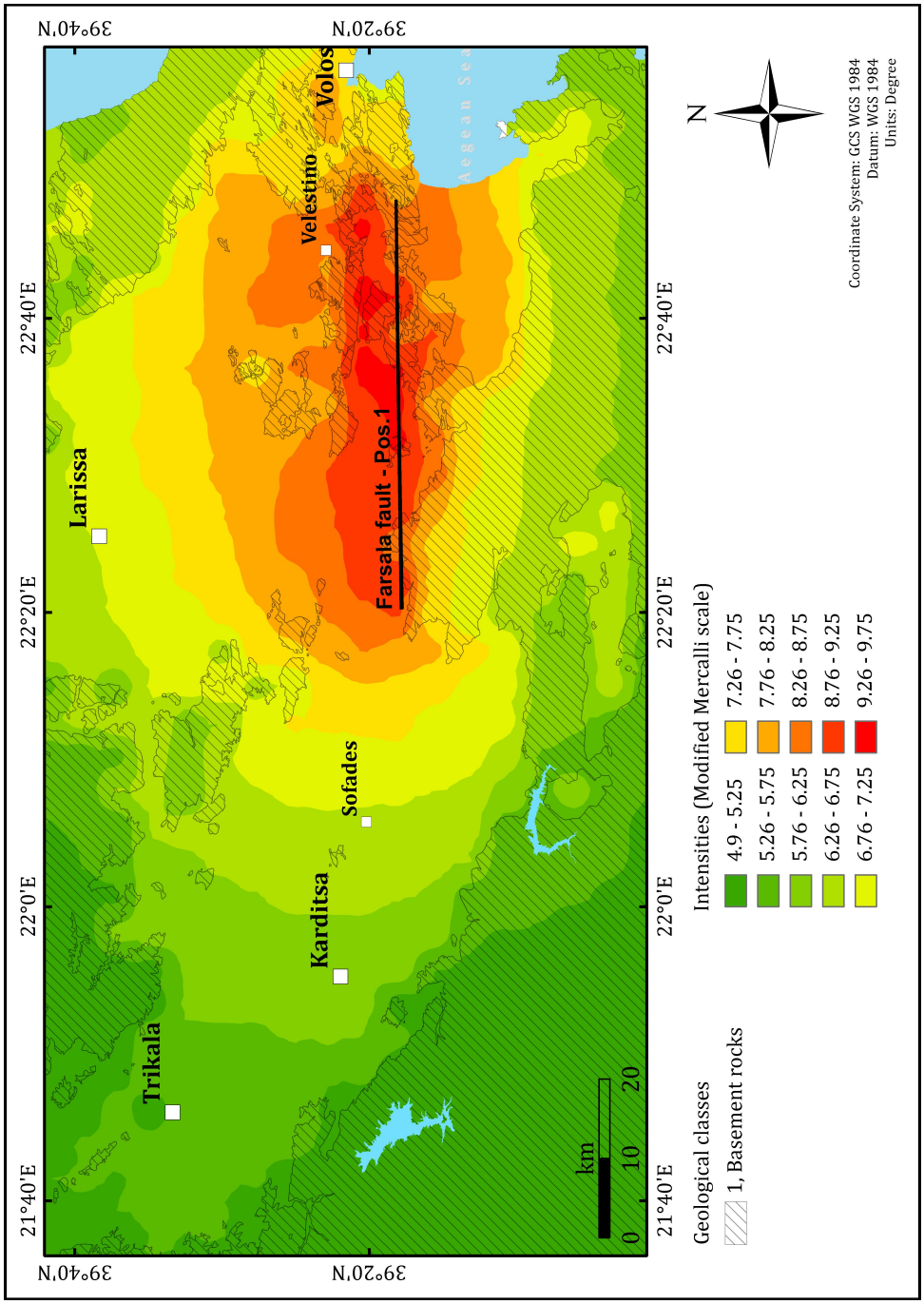

Figure 4.5: Same as Figure 4.4 considering the constant PGA / PGV site amplification factors of Skarlatoudis et al. (2003).

Finally, the utilization of the 1998 microzonation study data allowed the creation of the V_{s30} model for the city of Karditsa, which revealed a relative spatial uniformity of V_s values throughout the whole urban Karditsa area. The study of the local geophysical setting by performing HVSR measurements, showed significant low-frequency amplifications within the city (of the order of ∼5-7), while measurements along selected routes (see Figure 2.15) indicated that these large amplifications are related to the significant Quaternary sediments thickness over bedrock formations, as presented in Figure 4.6.

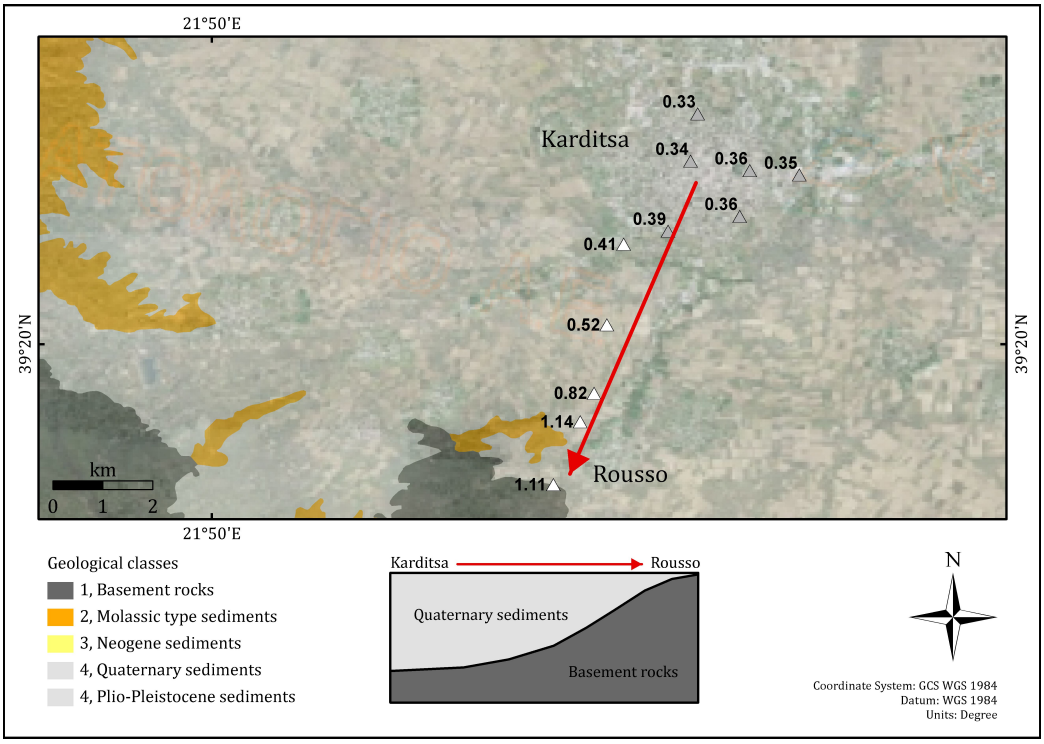

Figure 4.6: Quaternary sediments thickness schematic profile and resonant frequencies from HVSR measurements, on a selected profile from the city of Karditsa to the bedrock formations near the village Rousso. Notice the gradual increase of the resonant frequency as we move closer to bedrock formations.

References

Andrus, R.D.; Zhang, J.; Ellis, B.S., and Juang, C.H. Guide for estimating the dynamic properties of south carolina soils for ground response analysis. South Carolina Department of Transportation, 2003.

Athanasopoulos, G.A. Empirical correlations vso-nspt for soils of greece: A comparative study of reliability. Proc. of Seventh International Conference on Soil Dynamics and Earthquake Engineering, pages 19–26, 1995.

Atkinson, G.M. and Boore, D.M. Ground-motion relations for eastern north america. Bull. Seism. Soc. Am., 85:17–30, 1995.

Atkinson, G.M. and Boore, D.M. Earthquake ground-motion prediction equations for eastern north america. Bull. Seism. Soc. Am., 96(6): 2181–2205, 2006.

Beresnev, I.A. and Atkinson, G.M. Finsim; a fortran program for simulating stochastic acceleration time histories from finite faults. Seismological Research Letters, 69(1):27–32, 1998.

Beresnev, I.A. and Atkinson, G.M. Generic finite-fault model for ground-motion prediction in eastern north america. Bull. Seism. Soc. Am., 89: 608–625, 1999.

Boore, D.M. Stochastic simulation of high-frequency ground motions based on seismological models of the radiated spectra. Bull. Seism. Soc. Am., 73:1865–1894, 1983.

Boore, D.M. and Atkinson, G.M. Stochastic prediction of ground motion and spectral response parameters at hard-rock sites in eastern north america. Bull. Seism. Soc. Am., 77:440–467, 1987.

Boore, D.M. and Joyner, W.B. Site amplifications for generic rock sites. Bull. Seism. Soc. Am., 87:327–341, 1997.

Borcherdt, R.D. Estimates of site dependent response spectra for design (methodology and justification). Earthquake Spectra, 10(4):617–653, 1994.

Caputo, R. and Pavlides, S. Late cainozoic geodynamic evolution of thessaly and surroundings (central-northern greece). Tectonophysics, 223(3): 339–362, 1993.

Dikmen, U. Statistical correlations of shear wave velocity and penetration resistance for soils. J. Geophys. Eng., 6:61–72, 2009.

Dobry, R.; Borcherdt, R.D.; Crouse, C.B.; Idriss, I.M.; Joyner, W.B.; Martin, G.R.; Power, M.S.; Rinne, E.E., and Seed, R.B. New site coefficients and site classification system used in recent building seismic code provisions. Earthquake Spectra, 16(1):41–67, 2000.

Haghshenas, E.; Bard, P.Y.; Theodulidis, N., and Team, SESAME WP04. Empirical evaluation of microtremors h/v spectral ratio. Bull. Earthq. Eng., 6:75–108, 2008.

Hasancebi, N. and Ulusay, R. Empirical correlations between shear wave velocity and penetration resistance for ground shaking assessments. Bull. Eng. Geol. Environ., 66:203–213, 2007.

Klimis, N.S.; Margaris, B.N., and Koliopoulos, P.K. Site-dependent amplification functions and response spectra in greece. Journal of Earthquake Engineering, 3(02):237–270, 1999.

Koliopoulos, P.K.; Margaris, B.N., and Klimis, N.S. Duration and energy characteristics of greek strong motion records. Journal of Earthquake Engineering, 2(3):391–417, 1998.

Lekkas, E. Geological structure and geodynamic evolution of the Koziakas range (western Thessaly) (in Greek). PhD thesis, Department of Geology, National and Kapodestrian university of Athens, 1987.

Lekkas, E. The presence of the western thessaly unit in the area of dafnospilia - ktimeni (southern thessaly) (in greek). Bull. Geol. Soc. Gr., 25(1):231–244, 1991.

Lekkas, E. Seismic design and organiztion of karditsa - sofades (in greek). Technical report, Sector of Dynamics, Tectonics and applied Geology, National and Kapodestrian university of Athens, 1998.

Margaris, B.N. and Boore, D.M. Determination of $\Delta\sigma$ and $\varkappa 0$ from response spectra of large earthquakes in greece. Bull. Seism. Soc. Am., 88:170–182, 1998.

Mavroeidis, G.P. and Papageorgiou, A.S. A mathematical representation of near-fault ground motions. Bull. Seism. Soc. Am., 93(3):1099–1131, 2003.

McKenzie, D. Active tectonics of the mediterranean region. Geophys. J. R. astr. Soc., 30(2):109–185, 1972.

Motazedian, D. and Atkinson, G.M. Stochastic finite-fault modeling based on a dynamic corner frequency. Bull. Seism. Soc. Am., 95:995–1010, 2005.

Mountrakis, D.; Kilias, A.; Pavlides, S.; Zouros, N.; Spyropoulos, N.; Tranos, M., and Soulakelis, N. Field study of the southern thessaly highly active fault zone. Proceedings of the 2nd Congress of the Hellenic Geophysical Union, 2:603–614, 1993.

Ou, G.B. and Hermann, R.B. Estimation theory for peak ground motion. Seismological Research Letters, 61(2):99–107, 1998.

Panagiotopoulos, D.G. and Papazachos, C.B. Application of modern methods for assessing the seismicity of karditsa. Proc. of the 1st development conf. of Karditsa, 2008.

Papanikolaou, D. and Sideris, C. Geology, the science of Earth (in Greek). Editions Pataki, 2007.

Papastamatiou, D. and Mouyaris, N. The earthquake of april 30, 1954, in sophades (central greece). Geophys. J. R. astr. Soc., 87:885–895, 1986.

Papazachos, B.C. and Papazachou, C. The earthquakes of Greece. Editions Ziti, 2002.

Papazachos, B.C.; Comninakis, P.E., and Drakopoulos, J.C. Preliminary results of an investigation of crustal structure in southeastern europe. Bull. Seism. Soc. Am., 56(6):1241–1268, 1966.

Papazachos, B.C.; Papaioannou, Ch.; Papazachos, C.B., and Savvaidis, A.S. Atlas of isoseismal maps for strong shallow earthquakes in greece and surrounding area (426bc-1995). Ziti Publ., Thessaloniki, 1997.

Papazachos, B.C.; Papadimitriou, E.E.; Kiratzi, A.A.; Papazachos, C.B., and Louvari, E.K. Fault plane solutions in the aegean sea and the surrounding area and their tectonic implications. Boll. Geof. Teor. Appl., 39(3):199–218, 1998.

Papazachos, B.C.; Papaioannou, C.A.; Papazachos, C.B., and Savvaidis, A.S. Rupture zones in the aegean region. Tectonophysics, 308:205–221, 1999.

Papazachos, B.C.; Mountrakis, D.M.; Papazachos, C.B.; Tranos, M.D.; Karakaisis, G.F., and Savvaidis, A.S. The faults which have caused the known major earthquakes in greece and surrounding region between the 5th century bc and today. Proceedings of 2nd National Conference Anti-Seismic Engineering and Technical Seismology, page 17–26, 2001.

Papazachos, B.C.; Scordilis, E.M.; Panagiotopoulos, D.G.; Papazachos, C.B., and Karakaisis, G.F. Global relations between seismic fault parameters and earthquake moment. Bull. Seism. Soc. Am., 36:1482–1489, 2004.

Papazachos, B.C.; Karakaisis, G.F.; Papazachos, C.B., and Scordilis, E.M. Perspectives for earthquake prediction in the mediterranean and contribution of geological observations. Tectonic Development of the Eastern Mediterranean Region. (From: Robertson, A.H.F. Mountrakis, D., eds), Publ. Geol. Soc., London, 260:689–707, 2006.

Pitilakis, K.D. and Anastasiadis, A.J. Soil and site characterization for seismic response analysis. 11th European Conference on Earthquake Engineering,Balkema, Rotterdam, 1998.

Skarlatoudis, A.A.; Papazachos, C.B.; Margaris, B.N.; Theodulidis, N.; Papaioannou, Ch.; Kalogeras, I.; Scordilis, E.M., and Karakostas, V. Empirical peak ground motion predictive relations for shallow earthquakes in greece. Bull. Seism. Soc. Am., 93:2591–2603, 2003.

Theodulidis, N.P. and Papazachos, B.C. Dependence of strong ground motion on magnitude-distance, site geology and macroseismic intensity for shallow earthquakes in greece: I, peak horizontal acceleration, velocity and displacement. Soil Dynamics and Earthquake Engineering, 11(7): 387–402, 1992.

Toro, G.R. and McGuire, R.K. An investigation into earthquake ground motion characteristics in eastern north america. Bull. Seism. Soc. Am., 77(2):468–489, 1987.

Tselentis, G.A. and Danciu, L. Empirical relationships between modified mercalli intensity and engineering ground-motion parameters in greece. Bull. Seism. Soc. Am., 98(4):1863–1875, 2008.

Tsiambaos, G. and Sabatikakis, N. Empirical estimation of shear wave velocity from in situ tests on soil formations in greece. Bull. Eng. Geol. Environ., 70:291–297, 2010.

(This page is left intentionally blank)

Appendix

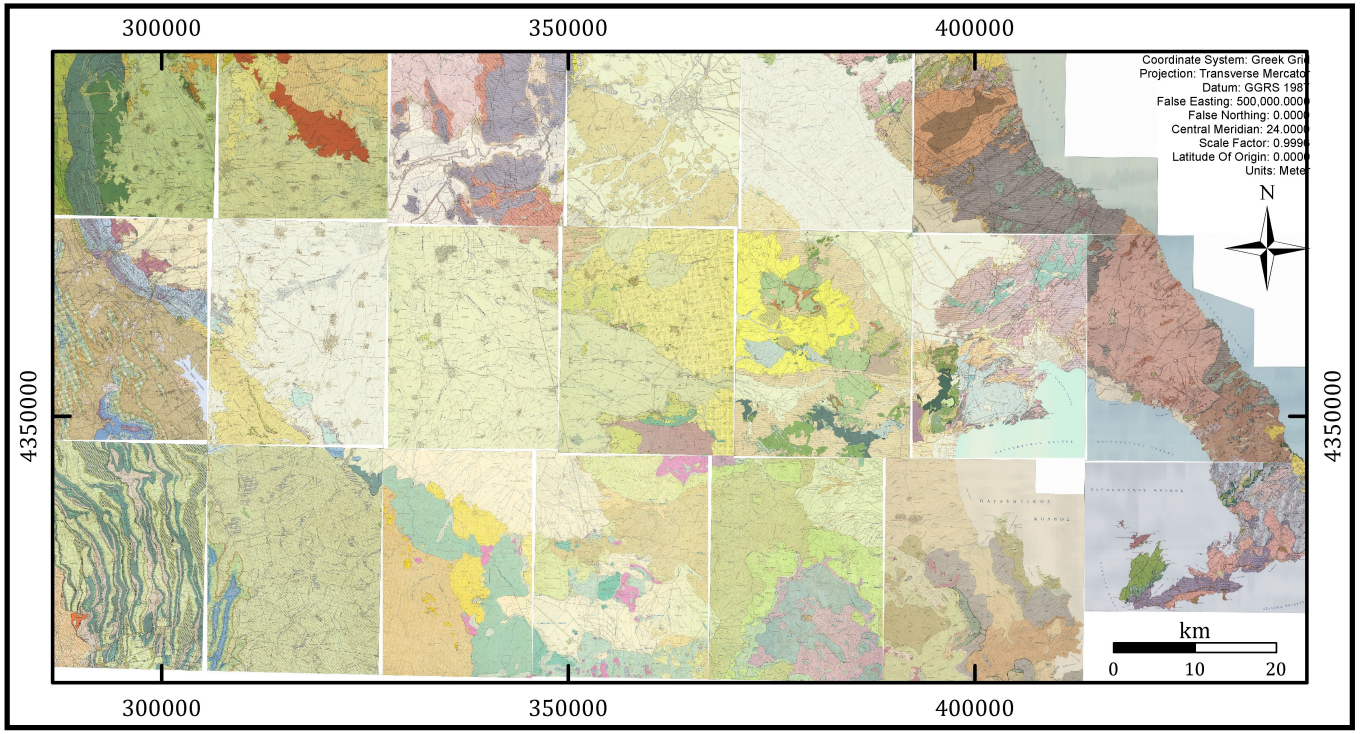

Figure A.1: The twenty (20) IGME geological maps (1:50000) used for the digitization of the geological formations of Thessaly.

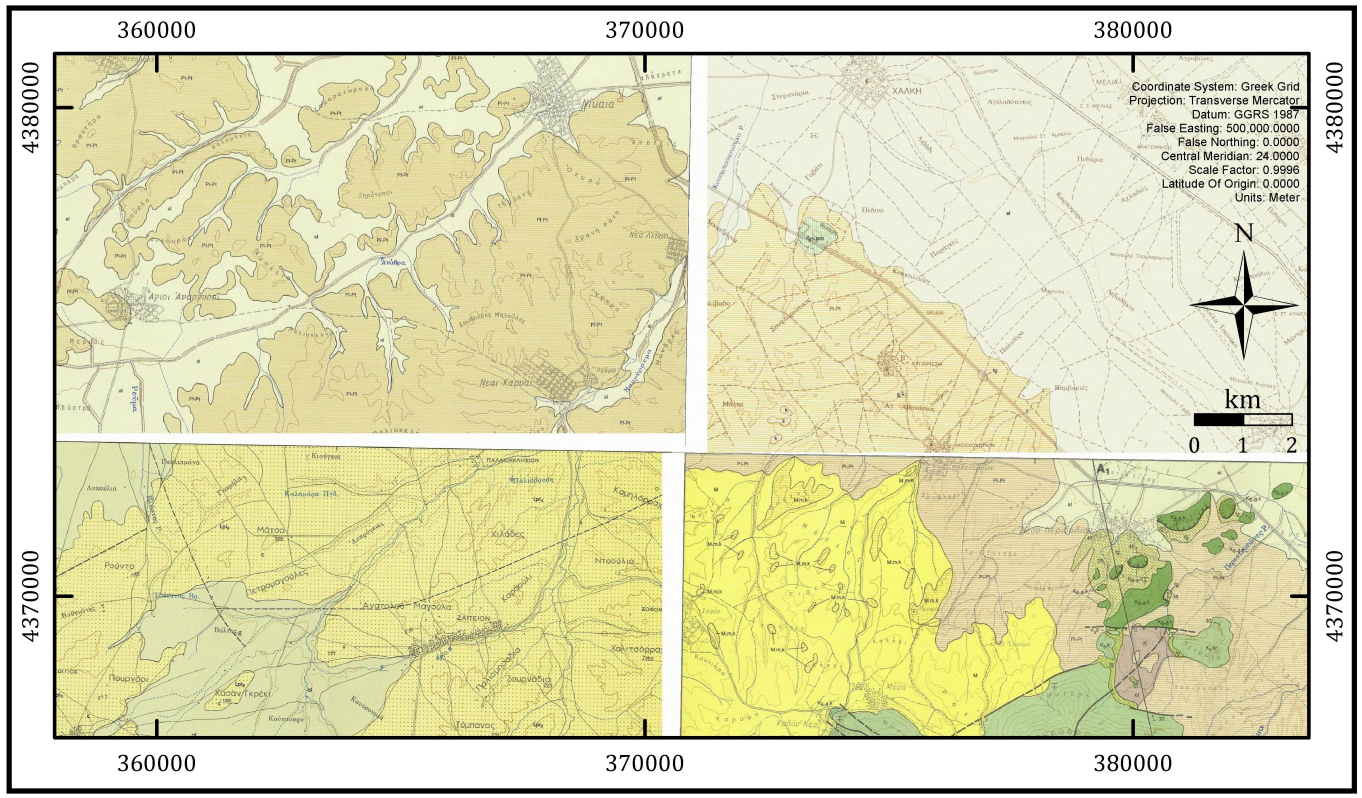

Figure A.2: Typical problematic junction of four adjacent IGME maps (1:50000) where incompatible or different level of detail geological formations are observed. The Velestino sheet (bottom right) separates the Neogene formations from the surrounding Plio-Pleistocene formations, contrary to the Farsala sheet (bottom left) which only characterizes the formations as Plio-Pleistocene.

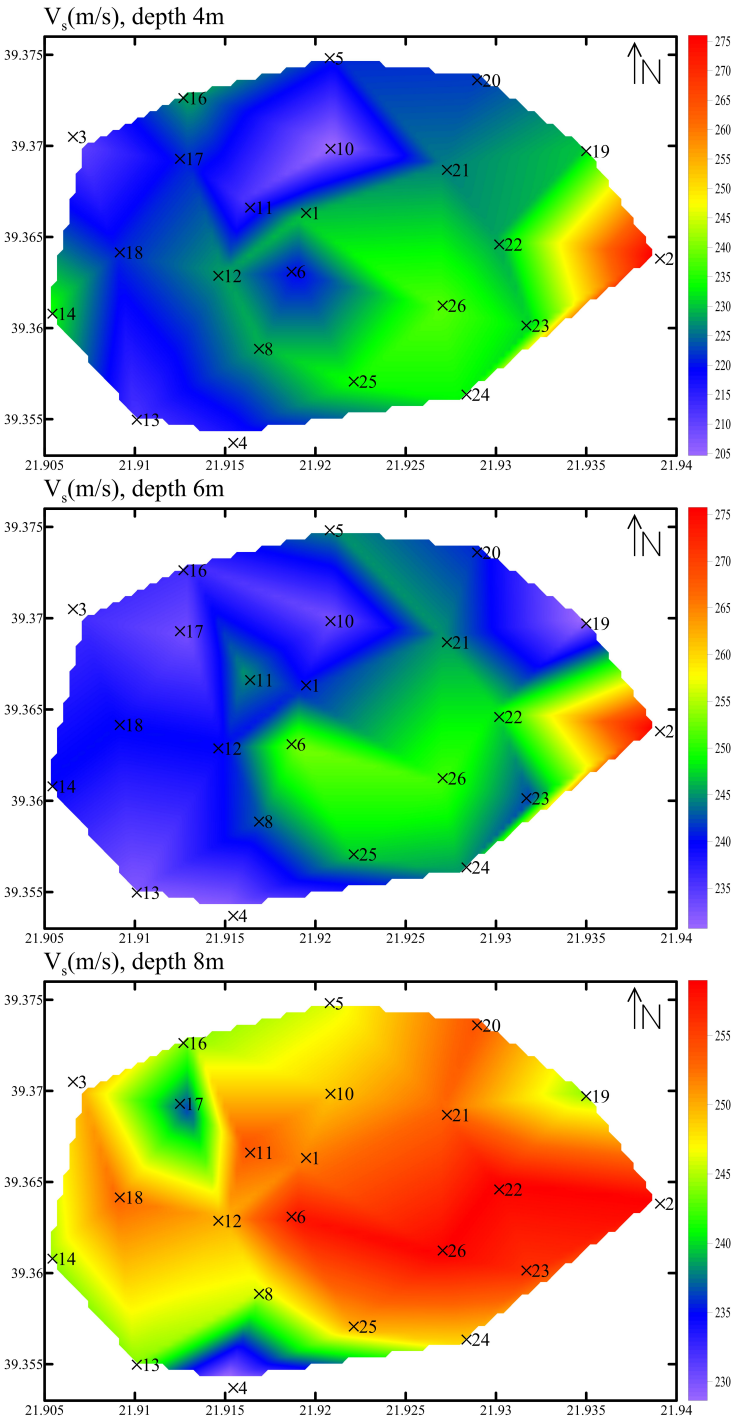

Figure A.3: Final V_s models determined for the depths of 4m, 6m and 8m, for the urban area of Karditsa.

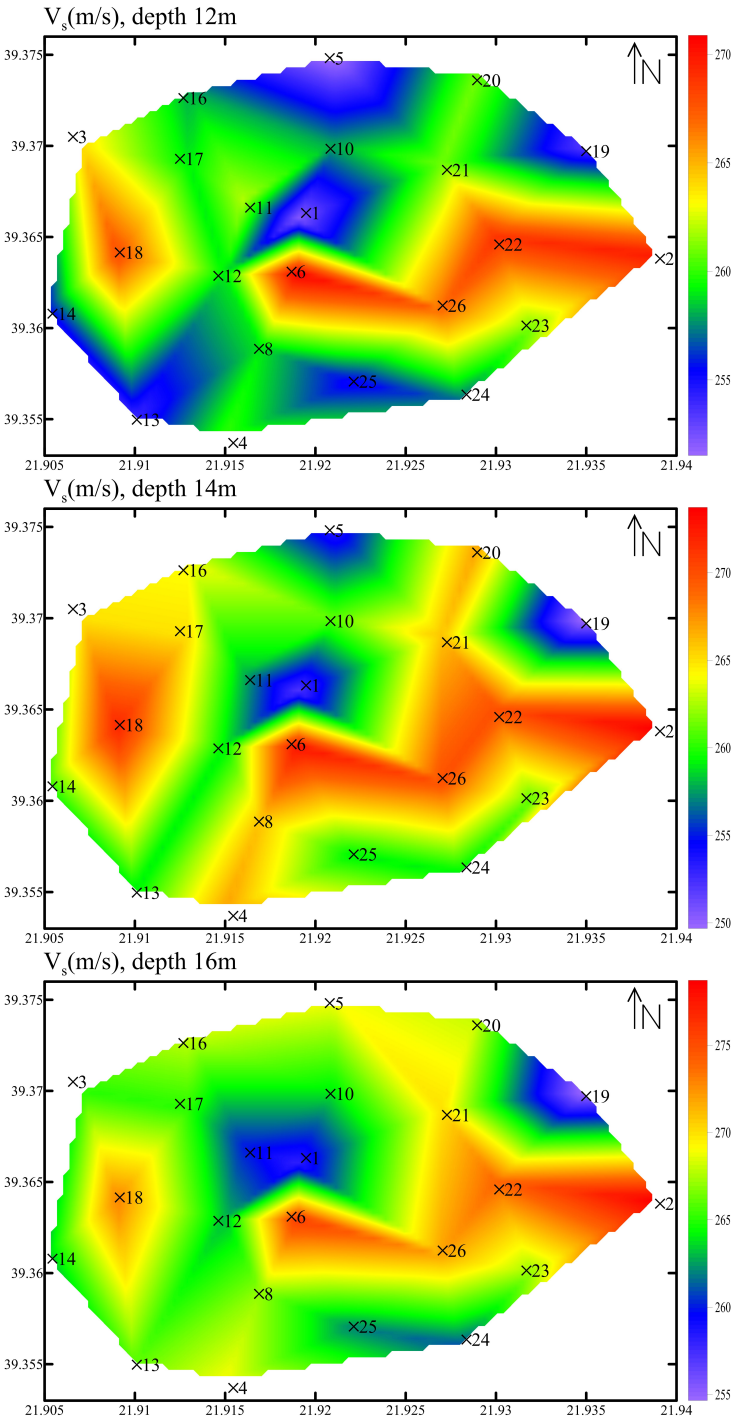

Figure A.4: Final V_s models determined for the depths of 12m, 14m and 16m, for the urban area of Karditsa.

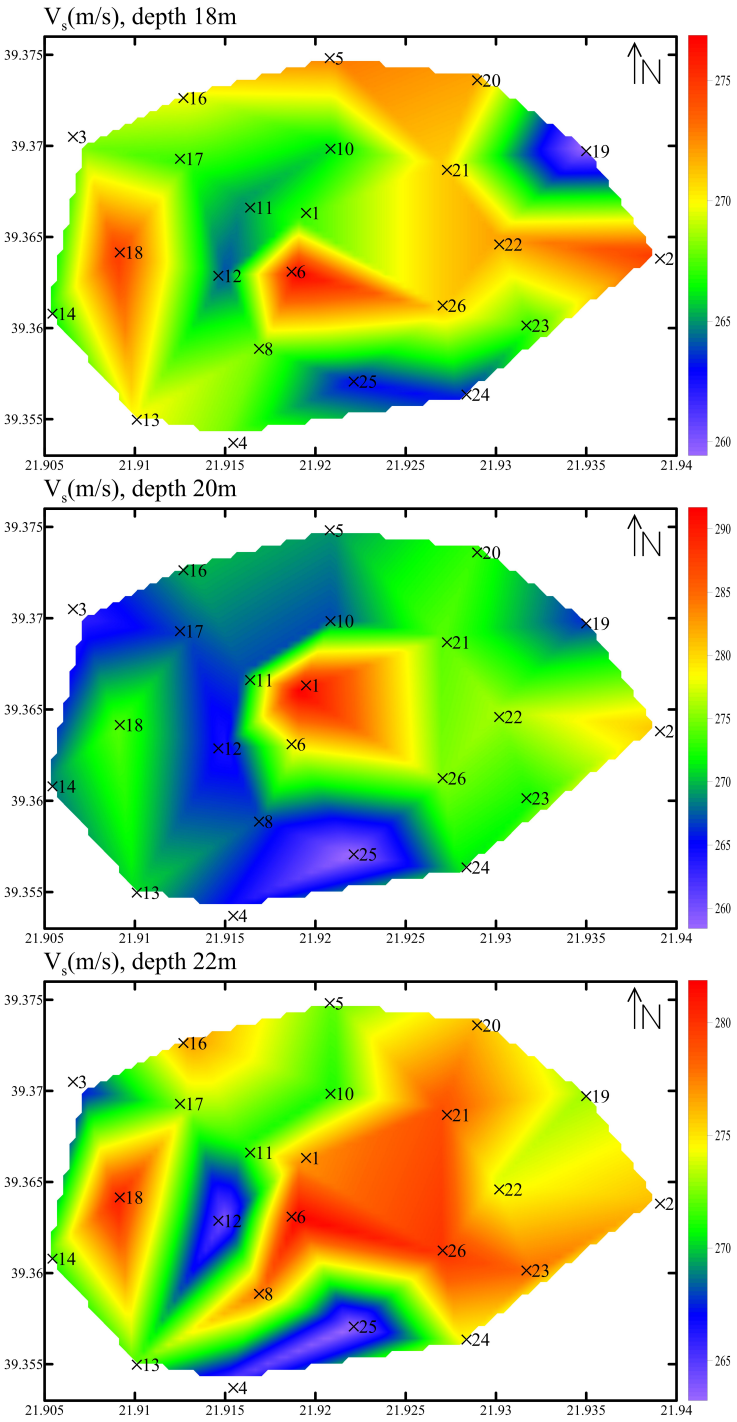

Figure A.5: Final V_s models determined for the depths of 18m, 20m and 22m, for the urban area of Karditsa.

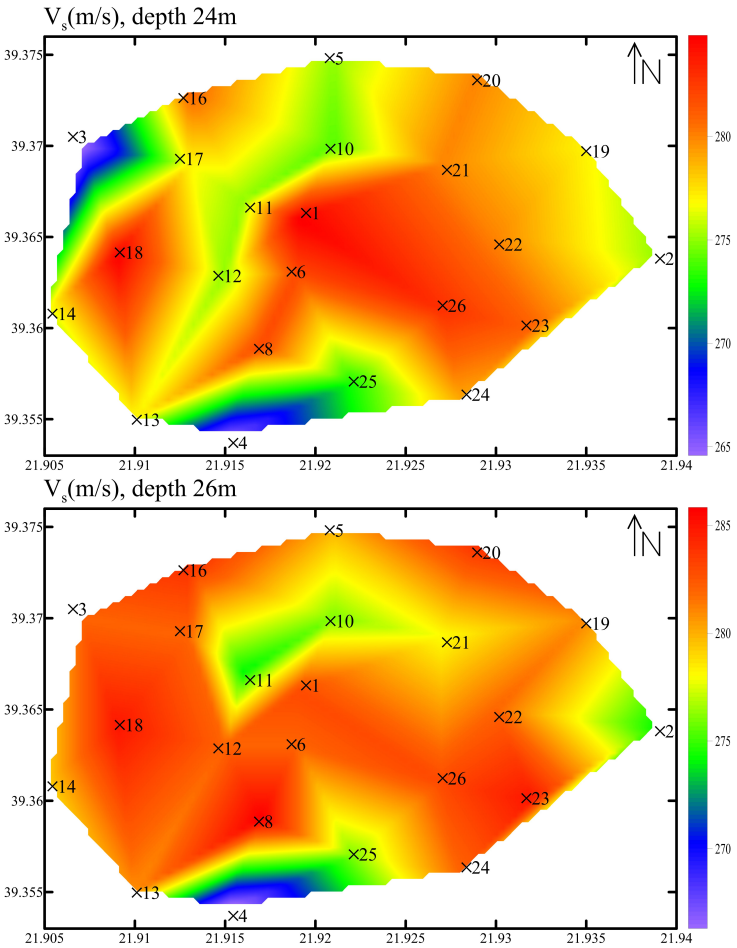

Figure A.6: Final V_s models determined for the depths of 24m and, 26m, for the urban area of Karditsa.

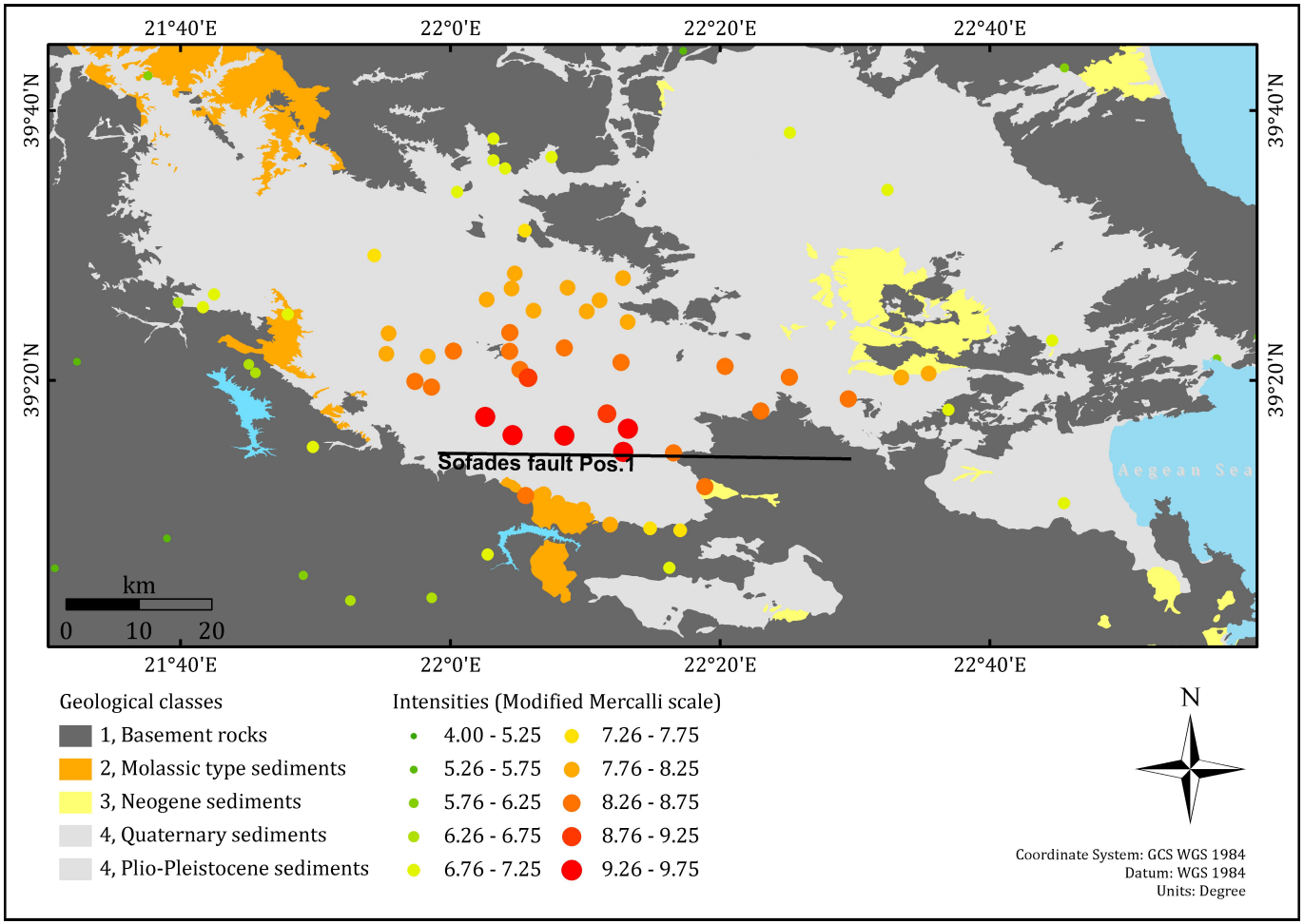

Figure A.7: Synthetic macroseismic intensities for the M=7.0, 1954 Sofades earthquake, considering fault position 1 (see Figure 3.4), with the use of the constant PGA / PGV site amplification factors of Skarlatoudis et al. (2003).

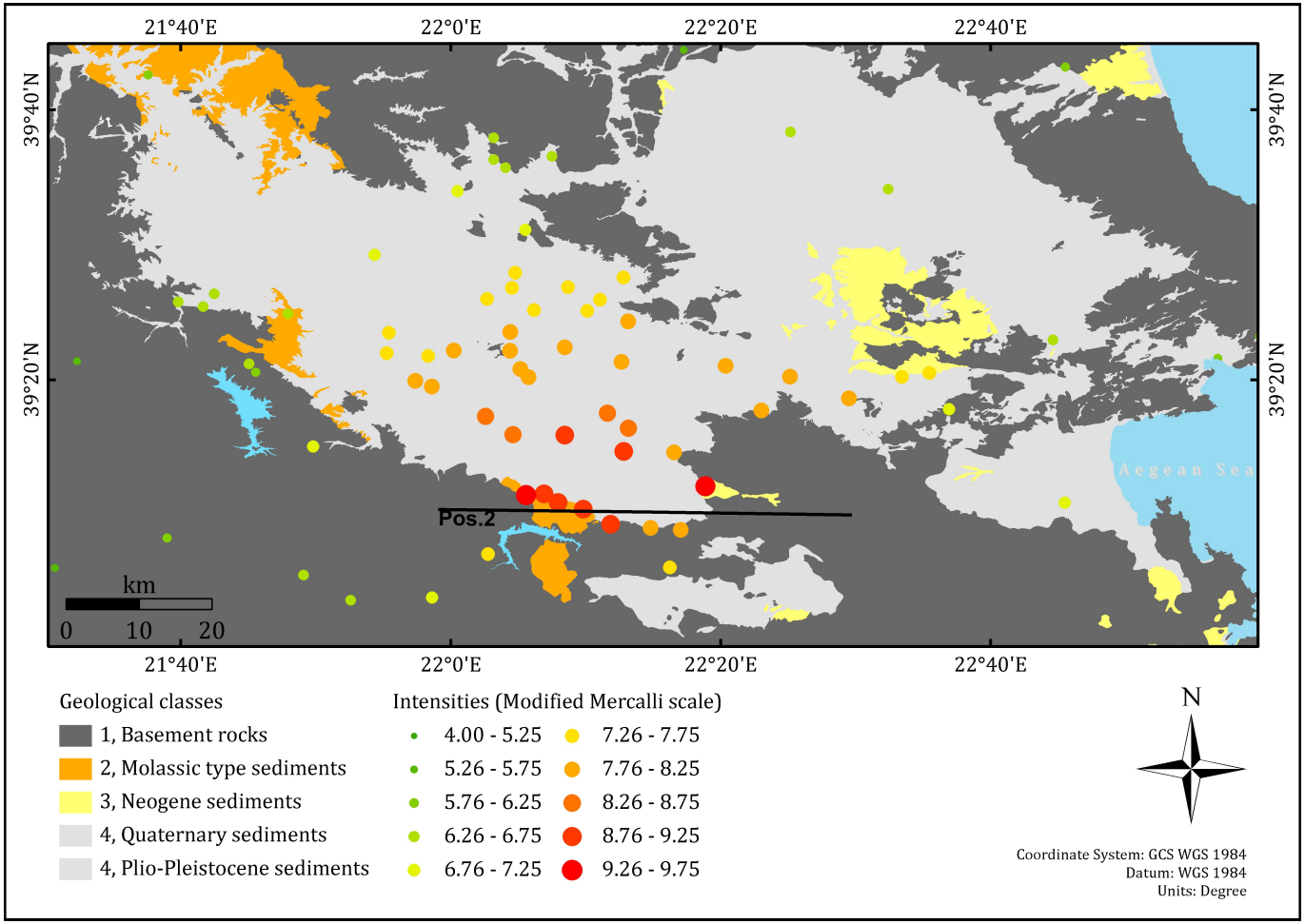

Figure A.8: Same as Appendix Figure A.7, considering fault position 2 (see Figure 3.4).

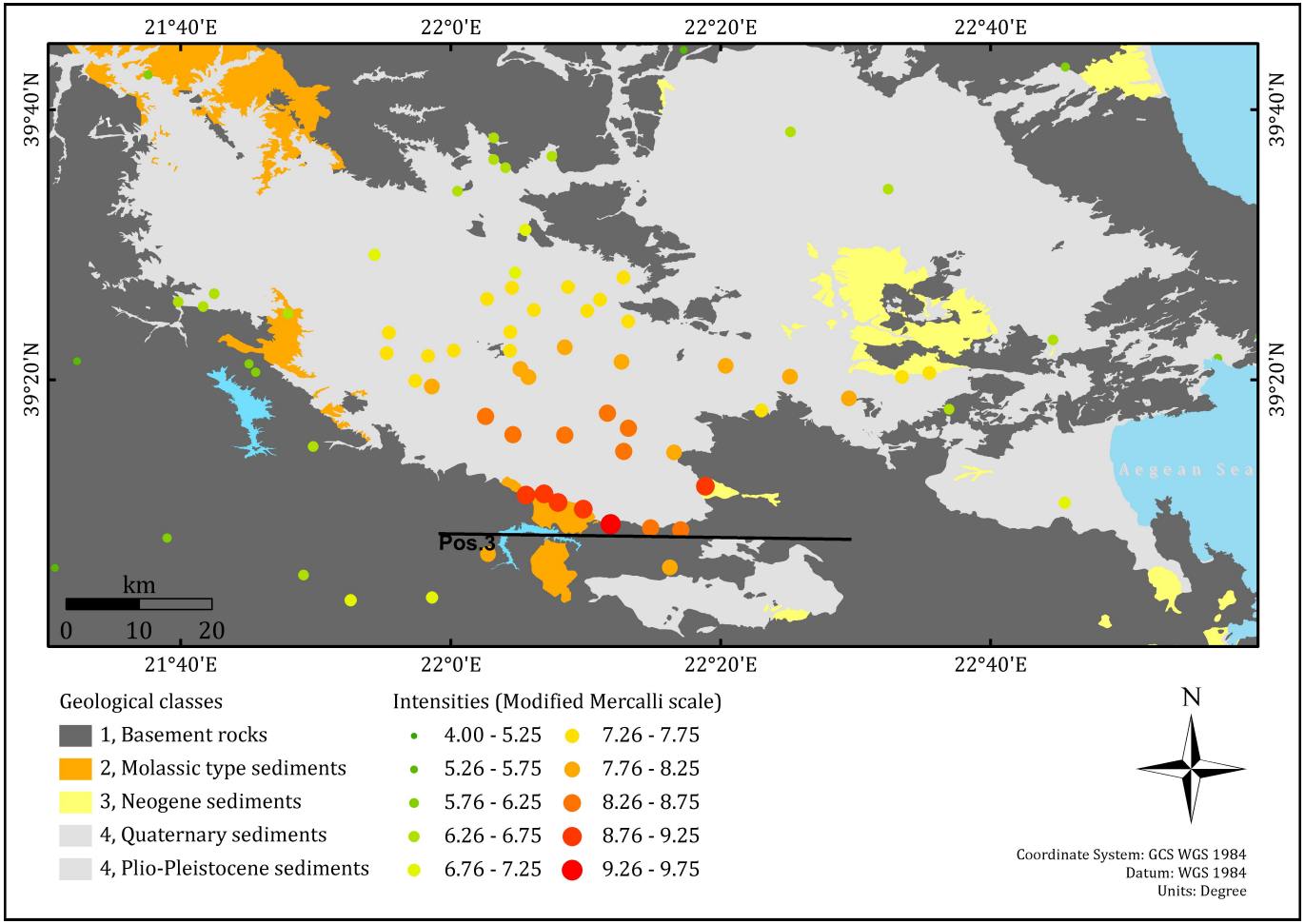

Figure A.9: Same as Appendix Figure A.7, considering fault position 3 (see Figure 3.4).

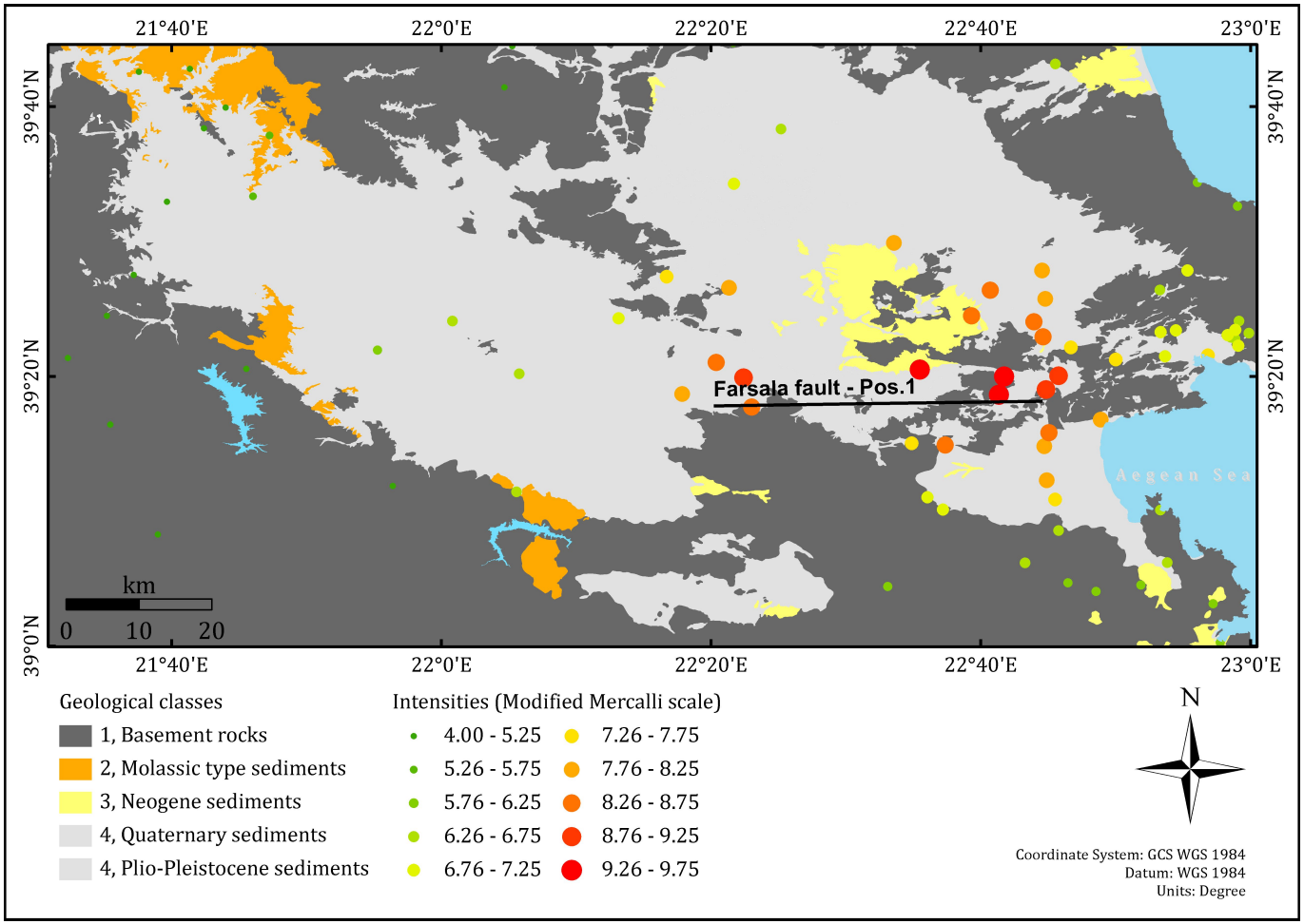

Figure A.10: Synthetic macroseismic intensities for the M=6.8, 1957 Velestino earthquake, considering fault position 1 (see Figure 3.10) with directional rupture and considering the constant PGA / PGV site amplification factors of Skarlatoudis et al. (2003).

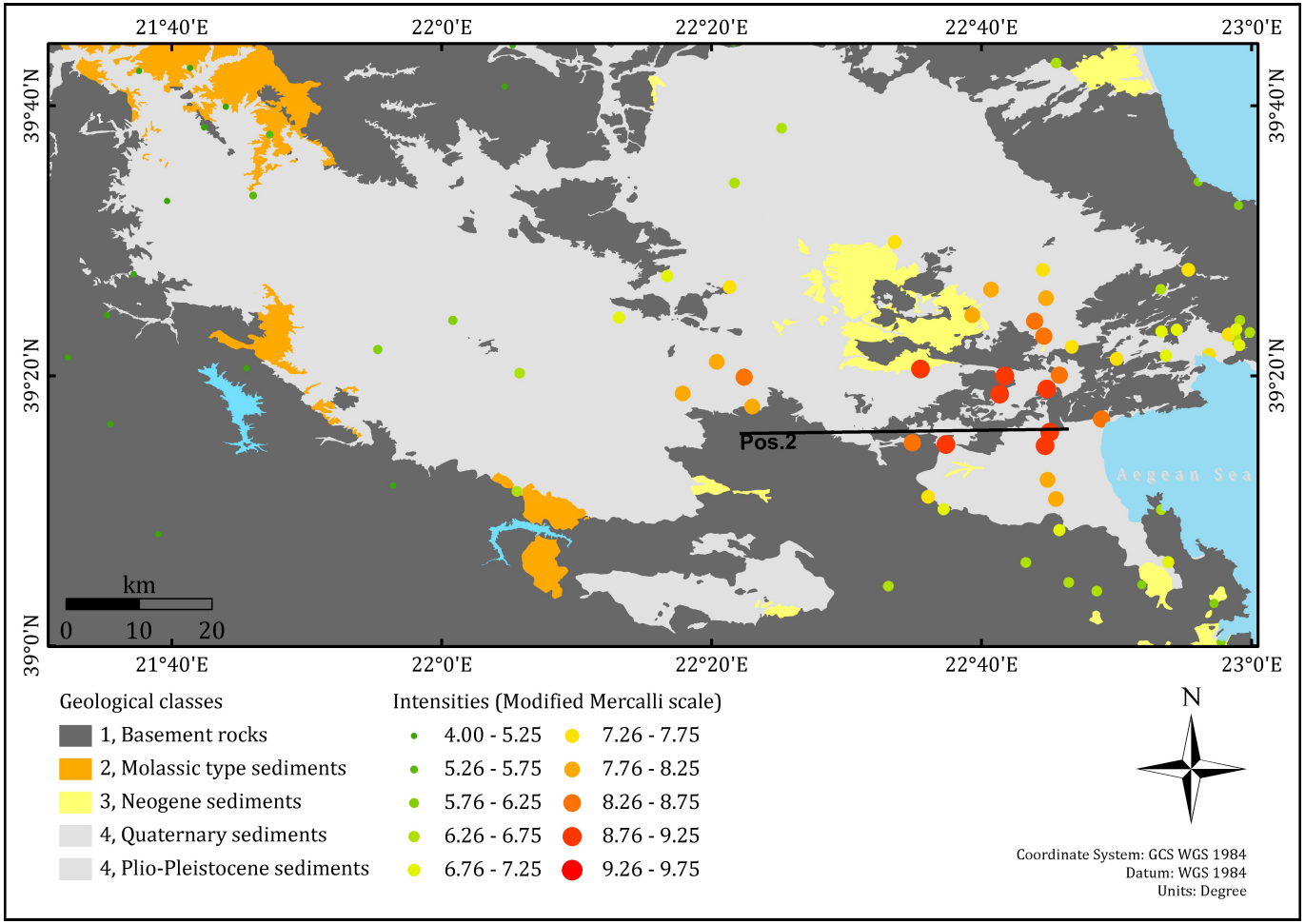

Figure A.11: Same as Appendix Figure A.10, considering fault position 2 (see Figure 3.10).

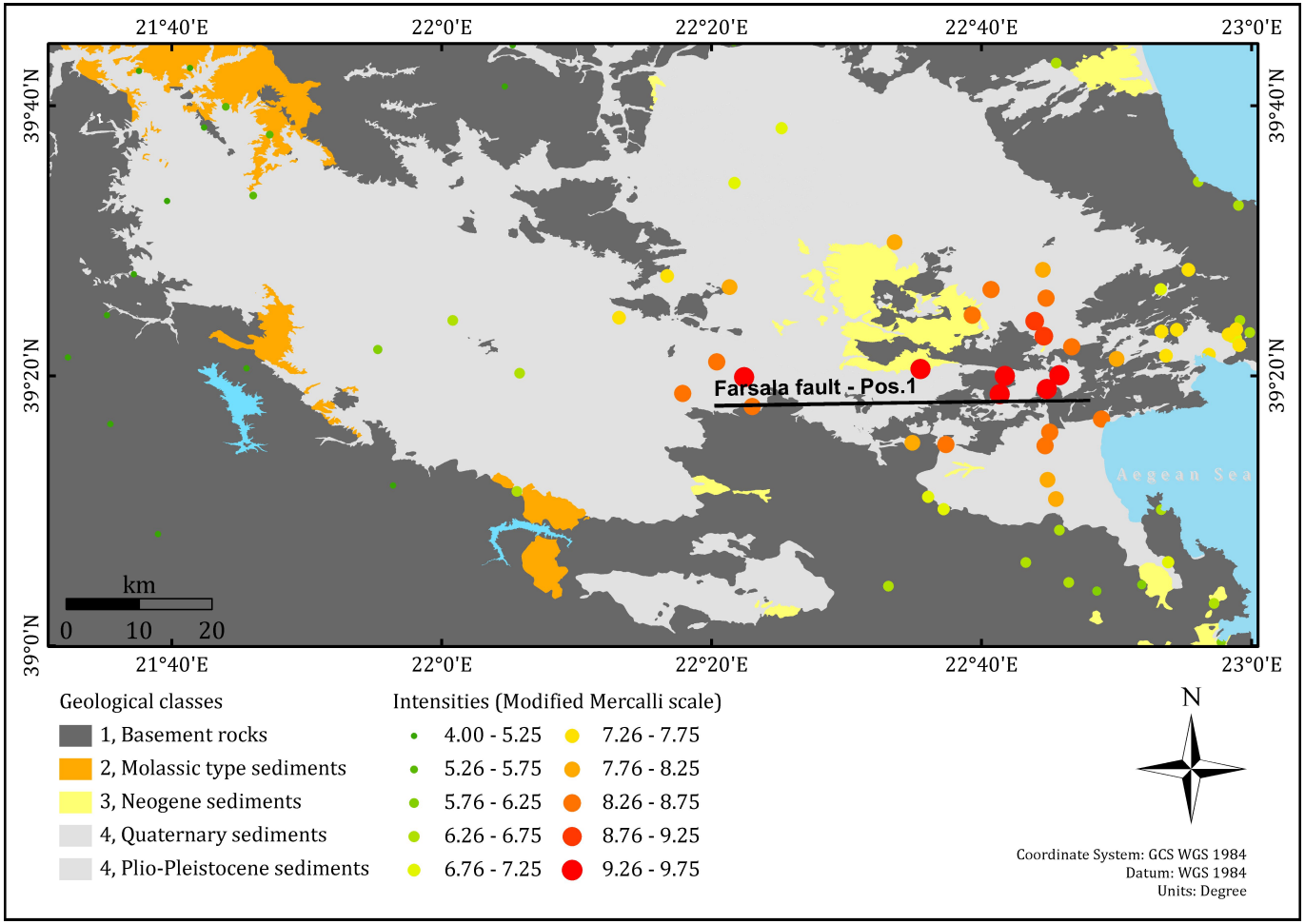

Figure A.12: Same as Appendix Figure A.10, considering fault position 3 (see Figure 3.10).

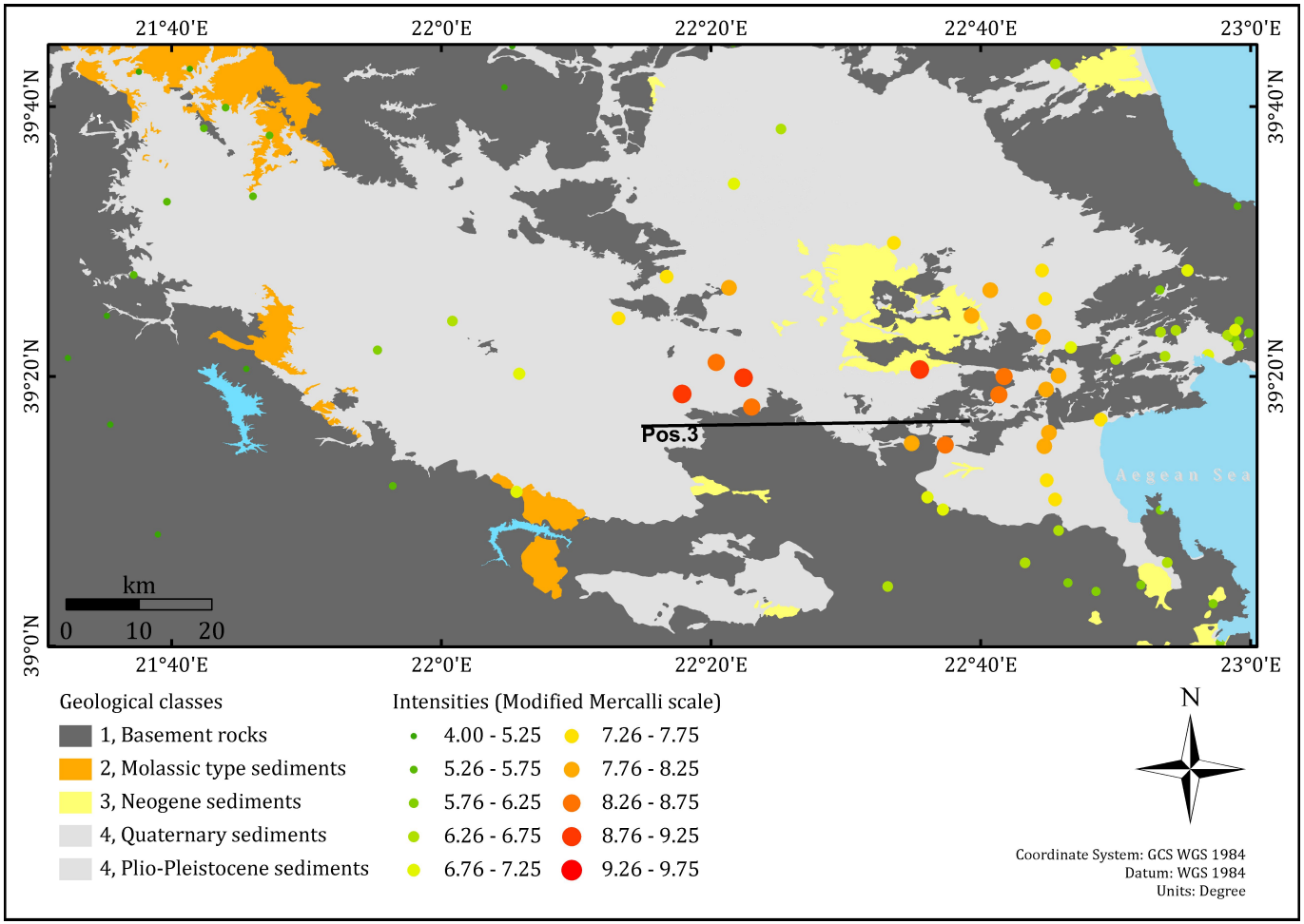

Figure A.13: Same as Appendix Figure A.10, considering fault position 1 (see Figure 3.10) with a larger fault length of 40km.